

國立交通大學

電子工程學系 電子研究所

博士論文

單一砷化銦量子點之磁光特性及其與光子晶體共振
腔之耦合

Magneto-Optical Properties of Single InAs Quantum Dot and
Their Coupling to Photonic Crystal Cavity

研究生：傅英哲

指導教授：林聖迪 教授

中華民國一〇三年七月

單一砷化銾量子點之磁光特性及其與光子晶體共振腔之耦合

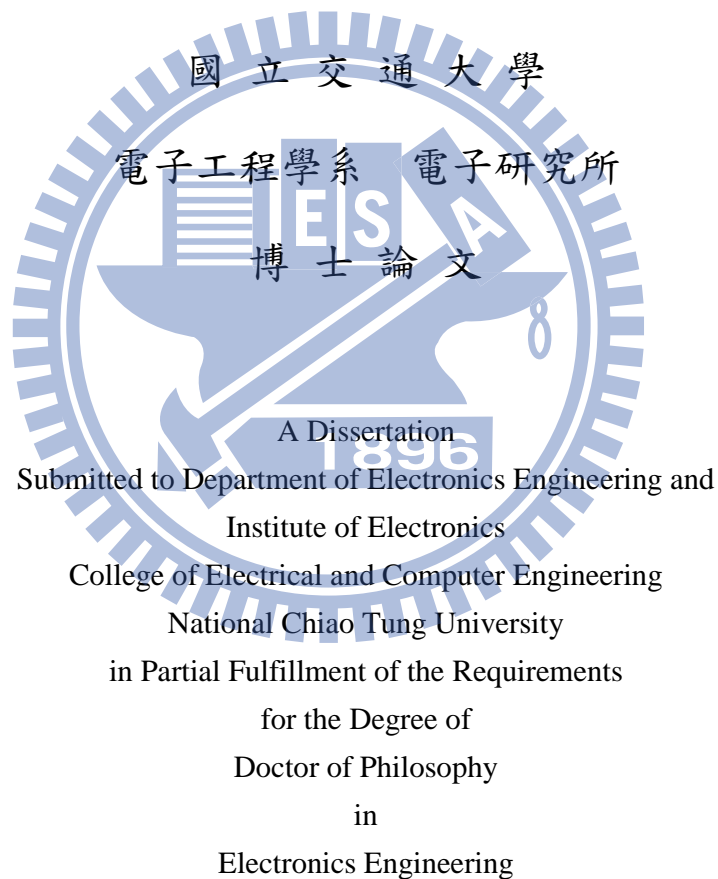
Magneto-Optical Properties of Single InAs Quantum Dot and Their
Coupling to Photonic Crystal Cavity

研究生：傅英哲

Student : Ying-Jhe Fu

指導教授：林聖迪

Advisor : Dr. Sheng-Di Lin



July 2014

Hsinchu, Taiwan, Republic of China

中華民國一〇三年七月

單一砷化銦量子點之磁光特性及其與光子晶體共振腔之耦合

研究生：傅英哲

指導教授：林聖迪 博士

國立交通大學

電子工程學系 電子研究所 博士班

摘要

此篇論文主要在研究單一量子點的螢光特性。我們報告單一自組式砷化銦/砷化鎵量子點內中性激子(X)、雙激子(XX)和帶電激子(X^+/X^-)對磁場的響應。與中性激子傳統上二次方相關的反磁性位移不同，我們觀察到的負帶電激子其反磁性位移較小而且與磁場呈現非二次方相關。更特別地是，我們也觀察到一個負號的反磁性位移。經過理論的分析，說明了負帶電激子這樣的異常行為是由於其在複合發光後，剩餘電子失去了未複合前電洞的強庫倫吸引力，而導致波函數在空間的分布劇烈地改變。對於小尺寸的量子點而言，這樣的效應非常明顯，因為其侷限電子的能力較弱，電子波函數延伸到周圍較高能障的砷化鎵。當電子逐漸地失去侷限性，負帶電激子的磁響應也將從對磁場二次相關的反磁性位移，逐漸變為四次方相關，最後變成一個順磁性的行為，也就是說隨著磁場強度的增加，負帶電激子的發光能量會變低。另一方面，我們研究單一量子點與光子晶體共振腔的耦合行為，為了達到高品質因子的 H1 型光子晶體共振腔，我們提出一個設

計的方法，其在計算上可以達到最高的品質因子大約 120,000。空間中共振模態電場分布的傅立葉轉換形式說明了品質因子的提升是因為有效地抑制了漏光模態。在實驗上，也展示了品質因子的提升，量測到的最高品質因子大約為 11,700。我們的設計在提升品質因子的同時並不會造成模態體積太大的提高，因此可以應用在量子點與 H1 型共振腔耦合的研究。最後我們成功地展示砷化銦量子點與 H1 型共振腔的強耦合效應。此時，量子點與共振腔混合成兩個新的 polariton 量子態造成螢光特性的改變。量測溫度大約在 37.75 K 時，有最強的耦合效應。經分析，其 Rabi 分裂大約是 $156.7 \mu\text{eV}$ 。



Magneto-Optical Properties of Single InAs Quantum Dot and Their Coupling to Photonic Crystal Cavity

Student : Ying-Jhe Fu

Advisor : Dr. Sheng-Di Lin

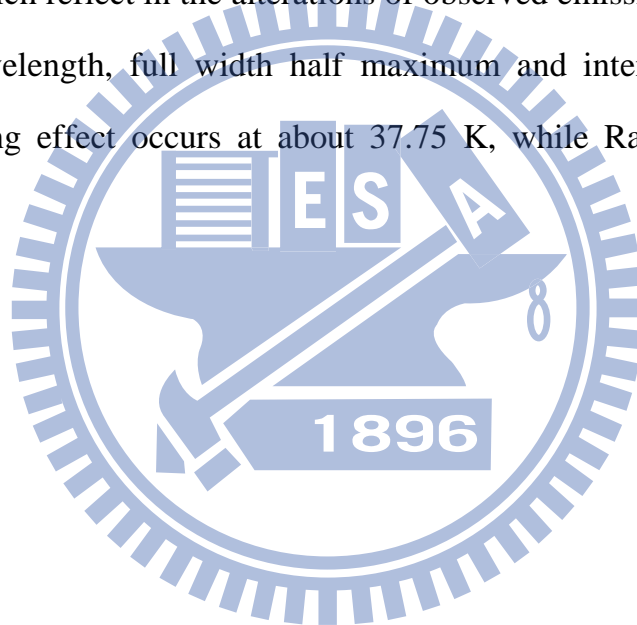
Department of Electronics & Institute of Electronics
National Chiao Tung University

Abstract

This dissertation mainly researches the photoluminescence characteristics of single quantum dot. We report on the magnetic responses of neutral exciton (X), biexcitons (XX) and positive/negative trions (X^+/X^-) in single self-assembled InAs/GaAs quantum dots. Unlike the conventional quadratic diamagnetic shift for neutral excitons, the observed X^- diamagnetic shifts are small and nonquadratic. In particular, we also observed a reversal in sign of the conventional diamagnetic shift. A theoretical analysis indicates that such anomalous behaviors for X^- arise from an apparent change in the electron wave function extent after photon emission due to the strong Coulomb attraction induced by the hole in its initial state. This effect can be very pronounced in small quantum dots, where the electron wave function becomes weakly confined and extended much into the barrier region. When the electrons gradually lose confinement, the magnetic response of X^- will transit gradually from the usual quadratic diamagnetic shift to a quartic dependence, and finally into a special *paramagnetic* regime with an overall negative energy shift.

On the other hand, we purpose to study the coupling effect between single quantum dot and photonic crystal cavity, a method for designing H1 photonic crystal cavity is

introduced to enhance its quality factor (Q factor). The highest theoretical Q factor of 120,000 is obtained. The Fourier transformation of field distribution shows that the enhancement arises from the component reduction of leaky mode. The Q-factor improvement has also been demonstrated experimentally with the highest value of 11700. Our design could be useful for studying light-matter interaction in H1 cavity as the mode volume only increases slightly. Finally, we successfully demonstrated the strong coupling effect in the H1 photonic crystal cavity embedded single InAs/GaAs quantum dot. Two polariton states arise from the hybridization of the cavity mode and quantum dot, which reflect in the alterations of observed emission characteristics, such as emission wavelength, full width half maximum and intensity. Via analysis, the strongest coupling effect occurs at about 37.75 K, while Rabi splitting is equal to $156.7 \mu\text{eV}$.



誌謝

終於迎來了畢業的這一刻。首先最感謝的就是林聖迪老師，在這幾年時間裡的辛苦指導，老師對於研究的熱忱以及剖析問題的看法，一直是我學習的對象。感謝您總是很有耐心地與我討論，並在我研究上遇到瓶頸時給予我正面的鼓勵，您總是很尊重我的想法，並適時地提供給我建議與協助。讓我能夠在這個氣氛融洽的實驗室裡有所成長，很慶幸能夠遇到如此好的老師。感謝李建平老師，為我們打造了一個資源豐富的研究環境，讓我們能夠盡情地發揮自己的想法，實踐理想，當老師在與我們分享研究經驗以及提出寶貴的意見時，總是讓我獲益良多。感謝張文豪老師，在量測方面以及我發表第一篇期刊時的建議及幫助。也感謝張老師實驗室的朋友們，林萱學姊、家賢、周湘諭學妹，之前受到你們的照顧了。羅明城學長、大鈞學長、旭傑學長、蔡明福學長、游宏凱學長，感謝你們傳承了珍貴的研究知識及經驗。感謝 Queena、巫俠、建宏、聖凱、KB、小金、尼克…等，在實驗上的幫忙及討論，尤其是 Queena 總是不厭其煩地提供我樣品，並對量測系統盡心地維護。平時大家還能一起打羽球，調劑身心。奈科二樓的夥伴們，師叔、小豪、林博、柏存、小羽、鴻霆、書文，大家一起熬夜做實驗，一起運動流汗的日子真的很充實、很快樂，很感謝有你們的陪伴和互相鼓勵，給予我支持和動力，這會是我人生中珍貴的回憶。

最後，最要感謝的是我親愛的家人，我的父母及妹妹。因為有你們的支持，我才可以無後顧之憂地投入研究。感謝你們總是在背後默默地關心著我、守護著我，陪我度過這段求學生涯。現在我順利完成學位了，在此將這份成就及榮耀獻給你們。

CONTENTS

Abstract (Chinese)	i
Abstract (English)	iii
Acknowledgement	v
CONTENTS	vi
Table Captions	ix
Figure Captions	x
Chapter 1 Introduction	1
1.1 Brief review of the semiconductor QDs.....	1
1.2 Brief review of photonic crystal.....	1
1.3 Research motivation.....	2
1.4 Organization of this dissertation	3
Chapter 2 Theoretical studies: the magnetic response of single quantum dot, photonic crystal cavity and light-matter interaction	5
2.1 Electronic configurations of quantum dot.....	5
2.2 Fine structure splitting	8
2.3 Magnetic response of quantum structures.....	12
2.3.1 Magnetic response of single particle	12
2.3.2 Magnetic response of Coulomb interaction.....	14
2.4 Concept of photonic crystal and cavity.....	16
2.5 Photonic Crystal fundamental theorem.....	18

2.6	Light-matter interaction : Jaynes-Cummings model.....	21
Chapter 3 Fabrication and Experiment/Simulation techniques		24
3.1	The growth of InAs/GaAs quantum dot.....	24
3.2	Fabrication of Aluminum apertures on QD sample	27
3.3	Fabrication of photonic crystal cavity.....	29
3.4	Conventional photoluminescence setup.....	31
3.5	Micro-photoluminescence setup	32
3.6	Finite-element method (fem) : Comsol Multiphysics	35
3.7	Finite-difference time domain (FDTD) method : Rsoft.....	35
Chapter 4 Magnetic response of single InAs QD.....		36
4.1	Micro- photoluminescence results	36
4.1.1	Power-dependent measurement.....	38
4.1.2	Polarization resolution measurement.....	40
4.2	Magneto-photoluminescence results.....	42
4.3	The simulation method for emission energies of excitonic complexes	47
4.4	The simulation results of diamagnetic shifts and their size-dependence	52
4.5	Brief discussion of anomalous diamagnetic shift	58
Chapter 5 Design of high quality-factor H1-cavities in 2-D photonic crystal and demonstration of their strong coupling to single InAs quantum dot.....		61
5.1	The designed structure of modified H1 cavity.....	61
5.2	The simulation results of Q factor and mode volume.....	63
5.3	The spatial Fourier transform of electric field distribution in cavity.....	65
5.4	Experimental results.....	68
5.5	The strong coupling effect between InAs QD and cavity.....	72

Chapter 6 Conclusion and Future work	77
6.1 Conclusion.....	77
6.2 Future work.....	78
Appendix	80
A Fock-Darwin model.....	80
B Hartree approximation.....	83
Reference	85
Vita	92
Publication List	93

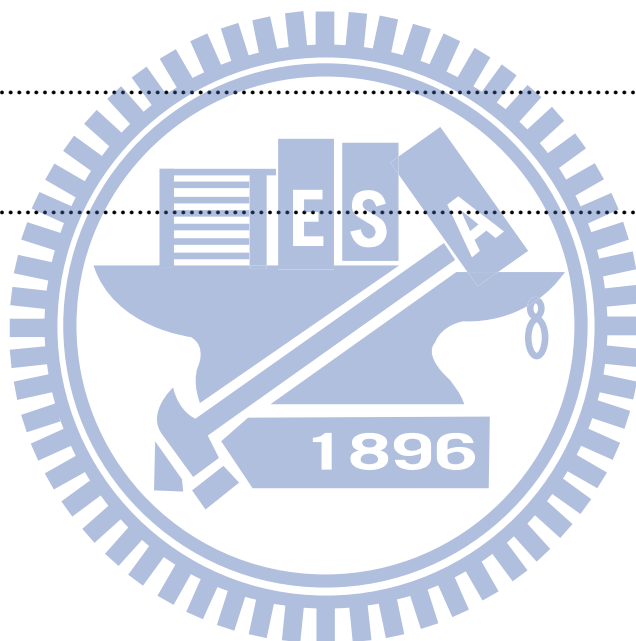


Table Captions

Table 4.1: The used material parameters in the simulation.53



Figure Captions

Figure 2.1: Band diagrams of Type I and Type II heterostructure	6
Figure 2.2: The excitonic complexes: neutral exciton (X), biexciton (XX), negative trion (X^-) and positive trion (X^+) in initial state (a) and final state (b).....	7
Figure 2.3: The X - XX cascade decay in QD with (a) and without (b) e-h exchange interaction.	10
Figure 2.4: Two cavity modes strongly couple to non-degenerated X states. Two groups of degenerate polariton states are formed.....	11
Figure 2.5: The illustrated scheme of one, two and three dimensional PhC.	16
Figure 2.6(a): The H1 cavity and its two fundamental modes: Horizontal and Vertical dipole mode.....	17
Figure 2.6(b): The H2 cavity and its fundamental modes: monopole mode.	17
Figure 2.6(c): The L3 cavity and its fundamental modes.....	17
Figure 2.7: A calculated TE mode band structure of an air-hole triangular lattice on a GaAs membrane with period=260 nm and air-hole radius=65 nm, this calculation uses FDTD method. The shadow region is so-called photonic band gap (PBG).....	20
Figure 2.8: The calculated TE mode band structure of a point defect PhC cavity formed by removing one hole in a perfect air-hole triangular lattice. A defect mode appears in the range of PBG.	20
Figure 2.9: A sketch of a two-level emitter coupling to a cavity resonator.	23
Figure 3.1: The structures of the samples embedded in InAs/GaAs QDs. (a) Lm4596 for single QD study (b) Lm5217 for PhC cavity study.....	25
Figure 3.2: The AFM images of the sample Lm4596.....	25
Figure 3.3: The PL spectra of the regions with different QD density in the sample Lm4596..	26

Figure 3.4: The process flow of A1 aperture on the sample Lm4596.....	28
Figure 3.5: The process flow of PhC cavity on the sample Lm5217.	30
Figure 3.6: The framework of the conventional PL setup.	32
Figure 3.7: (a) The framework of the μ -PL setup. (b) The laser beam is focused onto the A1 aperture.....	34
Figure 3.8: The top/side view of the calculated H1 cavity structure (left/right). The orange arrow is the excited Gaussian pulse.	35
Figure 4.1: The measured micro-PL spectra of seven different apertures in Lm4596.	37
Figure 4.2: (a) The PL spectra of QD3 excited by the power from 43nW to 10 μ W. (b) The dependence between PL intensity and the excitation power.....	39
Figure 4.3: (a) The PL spectra of QD5 excited by the power from 43nW to 10 μ W. (b) The dependence between PL intensity and the excitation power.....	39
Figure 4.4: The polarized PL spectrum of X , XX , X^- and X^+ in QD3 for polarized angle 80° (blue peaks) and 160° (red peaks), respectively.	41
Figure 4.5: The figure of peak intensity versus polarized angle for X (left) and XX (right). The blue and red curves represent the split peaks due to FSS.	41
Figure 4.6: (a) The magneto-PL spectra for QD1 under a magnetic field $B=0-6$ T. (b) The corresponding peak energies of different excitonic complexes as a function of B for QD2, where $\sigma+$ and $\sigma-$ in each form a Zeeman doublet. The dashed line is the average energy of $\sigma+$ and $\sigma-$	42
Figure 4.7: The Zeeman splitting versus B (a) and the diamagnetic shifts versus B^2 (b) for X^- , X , XX , and X^+ of four QDs (QD2, QD3, QD4, QD5). Points are the measured data, and the lines are guide for the eye.....	46
Figure 4.8: The diamagnetic coefficients γ_{X^-} , γ_X , γ_{XX} and γ_{X^+} are plotted as a function of X emission energy.	47
Figure 4.9: The steps of self-consistent calculation.	51

Figure 4.10: The cross-section of simulated cone-shaped InAs QD, of which the height and diameter are denote h and w.....	53
Figure 4.11: The band diagram of InAs/GaAs interface in QDs.	53
Figure 4.12: The diamagnetic shifts of the excitonic complexes for the three typical QDs (QD3, QD1 and QD4). Blue points and red lines are the experimental and simulated results, respectively. The simulated parameters are diameter of 11.6 nm and height of 1.1 nm for QD3; diameter of 11 nm and height of 1.4 nm for QD1; diameter of 8.4 nm and height of 1.4 nm for QD4.....	54
Figure 4.13: The experimental and simulated diamagnetic coefficients of the excitonic complexes for the three typical QDs (QD3, QD1 and QD4). The simulated parameters are diameter of 11.6 nm and height of 1.1 nm (QD3); diameter of 11 nm and height of 1.4 nm (QD1); diameter of 8.4 nm and height of 1.4 nm (QD4).	54
Figure 4.14: The simulation for QDs with various diameters, the diamagnetic coefficients (a), and the root mean square radius of electron and hole wave functions in their initial and final states (b).	57
Figure 4.15: The distribution of calculated electron wave function in X^- initial state (a), and X^- final state (b); The distribution of calculated hole wave function in X^+ initial state (c), and X^+ final state (d). White line: the QD's boundary with diameter of 11.6nm and height of 1.1nm.....	57
Figure 4.16: The diamagnetic coefficients γ_{X^-} , γ_X , γ_{XX} and γ_{X^+} are plotted as a function of X emission energy. The dashed lines are guide for the eye.	58
Figure 4.17: The theoretical (left) and experimental (right) anomalous diamagnetic shifts in small QDs.....	60
Figure 5.1: The tilt-view and top-view of H1 PhC cavity.	62
Figure 5.2: Schematic modified H1 cavity. The lattice constant is a. The radius of regular air	

hole is r . The nearest six air holes around defect are shifted and their radii are reduced to r' , as illustrated in the enlarged figure on the right. The radii of air holes inside regions I and II are reduced to r''	63
Figure 5.3: Our simulated Q factors compare with that of Ref. 50. The hollow-block points are the results of Ref. 50, and the solid-green points are ours.	64
Figure 5.4: (a) Simulated Q factors against varied r''/r ratios. Each line represents individual value of r' from 0.154a to 0.231a. (b) The corresponding mode volumes.	65
Figure 5.5: The simulated electric field distributions (E_x) of V dipole mode for various r''/r ratios (upper row) and their 2-D spatial Fourier transform profiles in tangential k-vector space $k//$ (lower row). Light cones are plotted in white circles.	67
Figure 5.6: The sketch of the total internal reflection condition. Medium 1 of refractive index n_1 is surrounded with mediums 2 of refractive index n_2	68
Figure 5.7: (a) Top view of SEM image for fabricated H1 cavity. The right figures are the local enlarged images of the six nearest holes and those in regions I and II. (b) Cross-section view of SEM image.	70
Figure 5.8: Measured spectra showing H- and V-dipole modes of an H1 cavity. The blue and red dots were measured data, and the blue and red curves were fitted data. Inset: the polar plot of cavity modes.	70
Figure 5.9: Measured Q factors and (b) enhancement factors for r''/r ratios of 1, 0.923, 0.846, and 0.769. The grouping devices are plotted with the same symbol. The dashed lines are guide for the eye.	71
Figure 5.10: The PL-spectra of the area with different QD density in the sample Lm5217.	74
Figure 5.11: The micro-PL spectra at three different temperatures 5.5 K, 28 K and 35K	75
Figure 5.12: The temperature-dependent micro-PL spectra.....	75
Figure 5.13: The emission energy, FWHM, and intensity as a function of temperature.	76
Figure 6.1: The difference in emission energy, FWHM, and intensity of two signals as a	



Chapter 1 Introduction

1.1 Brief review of the semiconductor QDs

The semiconductor quantum dots (QDs) are the nanometer-scaled materials with size about 10~100 nm, where the carriers are confined in three dimensions, and the discrete quantum levels are formed, resulting in many special characteristics different from bulk materials. Due to its tunable light wave length and high efficiency of photon absorption and emission, QDs have been considered to be suited for many optical electric devices, such as semiconductor laser and quantum dot Infrared photodetector (QDIP). In addition, for quantum information process, including quantum cryptography and quantum computing, is another particularly noteworthy area. By recent researches, the realizations of these quantum information technologies are believed to necessarily rely on the single photon source and entangled photon pair [1-4]. To generate the single photon source and entangled photon pair, single QD is a very suitable selection due to its quantized two-level system. Hence understanding and manipulating the emission mechanism of single QD are quite important and interesting issues.

1.2 Brief review of photonic crystal

Photonic crystal (PhC) cavities are usually used to serve as a resonator with the specific light wavelength, and have been applied on many areas, including low-threshold nanolasers [5-6], optic filters with waveguides [7-8] and cavity quantum electrodynamics because of their excellent photon confinement within tiny volume. In cavity quantum electrodynamics, single quantum dot (SQD) coupled to photonic

crystal cavity has been studied extensively, QD emission rate would be effectively controlled or enhanced by Purcell factor [9-13]. Recently, single QD coupled to pillar micro-cavity has been used to realize single photon source with identical quantum states [14, 15]. With high quality factor (Q factor) cavities and small mode volume, the strong coupling effect [16, 17] has also been demonstrated in such systems, in theory, that is proposed to be a possible way to eliminate the fine structure splitting (FSS) of QDs for generation of entangled photon pairs as predicted in Ref. 18 and 19. Various two-dimensional PhC cavities with high Q factor and small mode volume have been demonstrated, such as the L3 cavity [20] and double heterostructure cavity [21]. However, these cavities have no two degenerately and orthogonally fundamental modes, which are necessary for tuning QD FSS via the strong coupling [18, 19]. Hence, to meet the requirements of Ref. 18 and 19, other type of high Q factor photonic crystal cavity has to be developed.

1.3 Research motivation

Based on the numbers of carriers confined in single QD, different excitonic complexes are formed due to the Coulomb interactions among the constituent carriers. Understanding the individual behaviors of these excitonic complexes would provide helpful information for quantum information technologies, thus the Coulomb interactions are necessary to be studied. By applying an external magnetic field, the distributions of carrier's wave function are more concentrated in QD, resulting in the changes of quantum levels and the raises of the binding energies. Thus the diamagnetic shifts induced by the magnetic field can reflect not only the QD's spatial confinement but also the interparticle Coulomb interaction [22]. The observations of diamagnetic shifts for three excitonic complexes, including neutral exciton (X), biexcitons (XX)

and positive trions X^+ , have been analyzed systematically [23], but that of negative trion (X^-) may be more interesting and still not yet realized completely. For example, C. Schulhauser *et al.* have theoretically predicted that a weakly confined negative trion (X^-) in large-size QDs would exhibit a negative magnetic dispersion [24], however, such an unusual behavior of X^- has not yet been observed in past works focused on charged trions in QD system [25, 26]. We study InAs QDs and hope to observe the spontaneous emission spectra of the all four excitonic complexes and their magnetic response. By comparing the difference among their diamagnetic shifts, we hope to realize the interparticle Coulomb interactions how to affect the overall diamagnetism. If Coulomb energies dominate over the single particle energies, the diamagnetic shifts should be expected to be more complicated because they become a measure of magnetic response of Coulomb energies. On the other hand, in the part of studying the coupling effective between QD and PhC cavity, we select the H1 PhC cavity though it has smaller Q factor than other cavities. However, it intrinsically has two orthogonal-fundamental dipole modes and relatively small mode volume. If its Q factor is enough high for entering the strong coupling regime, the FSS of QDs may be eliminated to generate the polarized entangled photon pair. With FDTD simulation, we hope to design a modified H1 photonic crystal cavity to enhance its Q factor while the mode volume is nearly unchanged so that the strong coupling with a single InAs QD would be realized.

1.4 Organization of this dissertation

In this dissertation, we mainly observe the magneto-photoluminescence of single InAs QD, the Q factor of the modified H1 cavity, and the strong coupling effect between QD and cavity by using the Micro-photoluminescence system. Chapter 1

introduces the applications of QDs and photonic crystal cavity. Chapter 2 presents the fundamental theorems of magneto-optical effect, PhC and the light-matter interaction, the Coulomb energies among carriers in QDs are also introduced for their magnetic responses. Chapter 3 presents experimental techniques, including the preparation of sample and measurement setup. The sample was grown by the MBE system, fabricated by an E-beam lithography and an ICP/RIE system. A micro-PL system can help us study the emission characteristics of the sample. Chapter 4 exhibits the experimental results of magneto-PL for excitonic complexes. We observed an anomalous X^- diamagnetic shift. A numerical simulation by using the finite element method within the Hartree and one band effective mass approximation is proposed to reasonably explain the anomalous behavior. Chapter 5 illustrate the structure of a modified H1 PhC cavity designed to enhancing Q factor, which demonstrates the highest theoretical Q factor of 120,000. The experimental results of Q factor are collected by the same micro-PL system. It also includes the detailed discussion of the distributions of the electric field in the cavity. Finally we report an observation of strong coupling effect between single QD and H1 cavity by the temperature-dependent PL measurement. Chapter 6 gives the conclusions of this work.

Chapter 2 Theoretical studies: the magnetic response of single quantum dot, photonic crystal cavity and light-matter interaction

2.1 Electronic configurations of quantum dot

Because of the confinement in three dimensions, quantum dots have discrete energy states. The electronic configuration of QD is always a rather interesting and complicated topic. A. Schliwa *et al.* [27] have had a detailed discussion about InGaAs QD's electronic configuration, in which the effects of QD shape, strain, Valence band mixing are all considered. Due to the relative position of conduction band and valence band of dot and barrier materials, QD is mainly classified into two groups: Type I and Type II heterostructures as described in Fig. 2.1. Because carriers prefer to concentrate in the material with lower potential, for Type I structure, electrons and holes are both confined in low band gap material 2. However, for Type II structure, electrons and holes are confined in material 2 and material 1, respectively. In this dissertation, the investigated InAs/GaAs QDs belong to Type I structure, thus the overlap of electron and hole wave functions is higher than that of Type II QDs, which leads higher emission intensity useful to our measurement.

Because of the strain effect of QDs, the valence band of heavy hole and light hole are split off so that holes mainly fill in the quantum states of heavy hole. When electrons and holes occupy quantum states, they can form so-called excitonic complexes due to Coulomb interactions. By Pauli exclusion principle, each state of conduction (valence) band can only be filled in two electrons (holes). Depend on the various numbers of constituent electrons and holes, four excitonic complexes are

formed in the ground state: neutral exciton (X), biexciton (XX), negative trion (X^-), and positive trion (X^+) as illustrated in Fig. 2.2. After the recombination of one pair of electron and hole, each excitonic complex radiates a photon and degenerate to its final state. For these excitonic complexes, the strengths of Coulomb interactions are different from each other, which would reflect in the spontaneous emission energy of the photon. Considering the direct Coulomb energies as the perturbation terms, the emission energies can be approximately written as,

$$E_{X^-} = E_e + E_h + E_g + V_{ee} - 2V_{eh} \quad (2.1)$$

$$E_X = E_e + E_h + E_g - V_{eh} \quad (2.2)$$

$$E_{XX} = E_e + E_h + E_g + V_{ee} + V_{hh} - 3V_{eh} \quad (2.3)$$

$$E_{X^+} = E_e + E_h + E_g + V_{hh} - 2V_{eh} \quad (2.4)$$

where $V_{\alpha\beta}$ is the Coulomb energy between α and β carrier, E_e/E_h is the quantum energies of electron/ hole, E_g is the band-gap of QD's material.

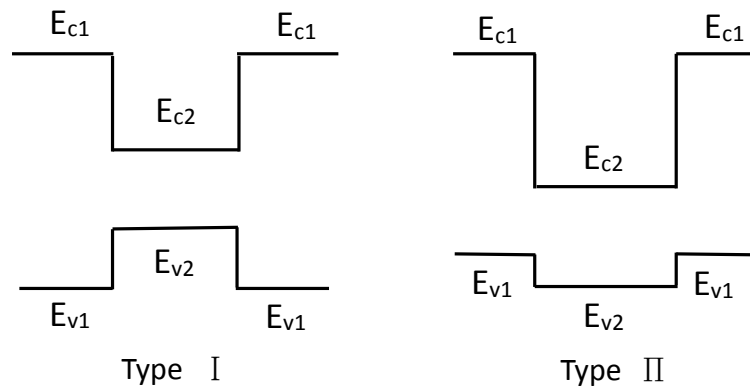


Figure 2.1: Band diagrams of Type I and Type II heterostructure

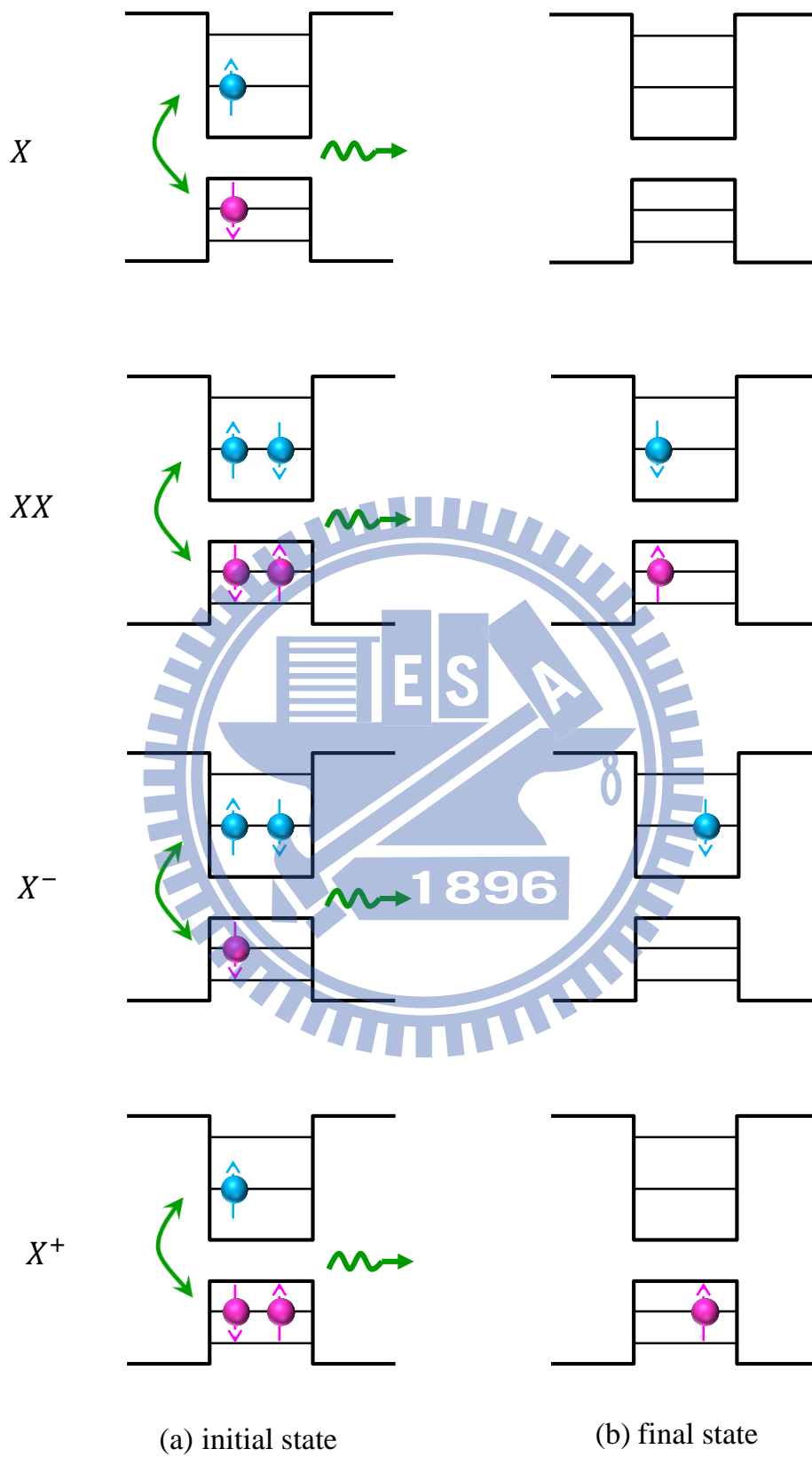


Figure 2.2: The excitonic complexes: neutral exciton (X), biexciton (XX), negative trion (X^-) and positive trion (X^+) in initial state (a) and final state (b)

2.2 Fine structure splitting

In the development of entangled photon pairs by QDs, an unavoidable problem of fine structure splitting (FSS) is always expected to be solved because it breaks the entanglement of the photons associated with X and XX emissions. In general, FSS is believed to arise from the broken symmetry of QD structure, such as the geometry elongation, strain and piezoelectric effect, which cause the long range e-h exchange interaction defined as

$$\delta = \iint d^3r_1 d^3r_2 \psi^h(\vec{r}_1)^* \psi^e(\vec{r}_2)^* \frac{e^2}{4\pi\epsilon_0\epsilon_r |\vec{r}_1 - \vec{r}_2|} \psi^h(\vec{r}_2) \psi^e(\vec{r}_1) \quad (2.5)$$

, where $\psi^e(\psi^h)$ denotes the envelope wave function of electron (hole), ϵ_0 and ϵ_r are vacuum permittivity and relative permittivity, e is electron charge, and \vec{r}_α is the position vector of α particle. The general form of the spin Hamiltonian for electron-hole exchange interaction is given,

$$H_{exhge} = - \sum_{i=x,y,z} (a_i \cdot J_{h,i} \cdot S_{e,i} + b_i \cdot J_{h,i}^3 \cdot S_{e,i}) \quad (2.6)$$

$J_h (S_e)$ is the hole (electron) spin Pauli matrices. The relation between FSS (2.5) and the distributed symmetry of carriers has been proposed by H.Y. Ramirez *et al.* in Ref. [28]. H.Y. Ramirez used the single band effective mass approximation to calculate the e-h exchange interaction based on a three dimensionally parabolic model. Their result is expanded as

$$\delta = K \cdot \beta_x \beta_y \beta_z \cdot \frac{\xi(1-\xi)}{(l_y^{eh})^3} \left(1 - \frac{3 l_z^{eh}}{2 l_y^{eh}} \right) + \dots \quad (2.7)$$

, where the factor K is determined by material parameters including the conduction-valence band interaction energy E_p , the dielectric constant ϵ and the bulk energy gap E_g^b ,

$$K = \frac{3\sqrt{\pi}e^2\hbar^2E_p}{(4\pi\epsilon_0)16\sqrt{2}\epsilon m_0(E_g^b)^2} \quad (2.8)$$

$\beta_x\beta_y\beta_z$ is defined as the e-h wave function overlap,

$$\beta_x\beta_y\beta_z = \left[\frac{2(l_x^h/l_x^e)}{1 + (l_x^h/l_x^e)^2} \right] \left[\frac{2(l_y^h/l_y^e)}{1 + (l_y^h/l_y^e)^2} \right] \left[\frac{2(l_z^h/l_z^e)}{1 + (l_z^h/l_z^e)^2} \right] \quad (2.9)$$

l_α^h denotes the wave function extent of h carrier in α direction. l_α^{eh} represents the effective wave function extent of exciton and is written as

$$l_\alpha^{eh} = \frac{\sqrt{2}l_\alpha^e l_\alpha^h}{\sqrt{(l_\alpha^e)^2 + (l_\alpha^h)^2}} \quad (\alpha = x, y, z) \quad (2.10)$$

The asymmetry of excition wave function in x and y direction is put a factor of ξ . If QD is in-plane symmetric, $\xi = 1$, resulting in the long range exchange $\delta = 0$

$$\xi = l_y^{eh}/l_x^{eh} \quad (2.11)$$

From Eq. 2.7, it is expect that the long range interaction is determined by overlap and asymmetry of e-h wave function.

Fig. 2.3 is a two-level system illustrated for understanding of the X - XX cascade decay with and without the e-h exchange interaction. With the e-h exchange interaction, the two bright X states lose their degeneracy so that the X emissions associated with the transition from X state to ground state become two linear polarized lights form two circular polarized lights, as well as the XX emissions associated with the transition from XX state to X state.

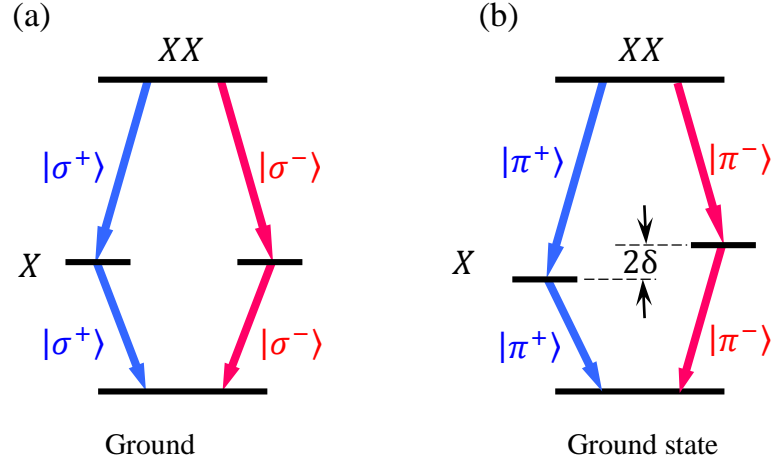


Figure 2.3: The X - XX cascade decay in QD with (a) and without (b) e-h exchange interaction.

In experiment, some literatures have been reported for successfully tuning FSS by applying in-plane magnetic field [29], in-plane electric field [30], and thermal annealing [31, 32]. Besides, R. Johne [18] and P. K. Pathak [19] *et al.* proposed another method for overcoming FSS in theory. They suggested that when two orthogonally-linearly polarized cavity modes split by the energy δ_c couple to the two X cascades split by the energy δ_x , where the two cavity modes are polarized along horizontal (H) and vertical (V) directions, as well as the two X cascades, via the strongly coupling effect, the X states and cavity modes can hybridize together and form two groups of linear-polarized polariton states by the Eq. 2.12,

$$E_{\pm}^{H,V} = \frac{E_{H,V} + E_c^{H,V}}{2} \pm \frac{1}{2} \sqrt{(E_{H,V} - E_c^{H,V})^2 + 4\hbar^2 \Omega_R^2} \quad (2.12)$$

where $E_{H,V}$ ($E_c^{H,V}$) denotes the exciton energies (cavity modes) for H and V polarization, Ω_R is the half of Rabi splitting. With appropriately relative positions of

their energy levels and coupling strength, it is possible to let the polariton states with different polarized directions to become degenerate, and generate the entangled photonic pair as illustrated in Fig. 2.4 (taken from Ref. 18). R. Johne *et al.* think polariton states can effectively prevent diphas because of its lifetime of ten to hundred times shorter than that of the bare exciton. Further, by their calculation, the degree of entanglement almost can achieve the maximum $1/2$.

In order to satisfy above requirements in polarization, H1 photonic crystal cavity, having two linearly-polarized fundamental modes, is one suitable selection for entanglement device than other types of photonic crystal cavities. Despite this, its relatively low Q factor and uncontrolled intrinsic splitting between two fundamental modes still make actual difficulties in manipulating. These difficulties are expected to be overcome.

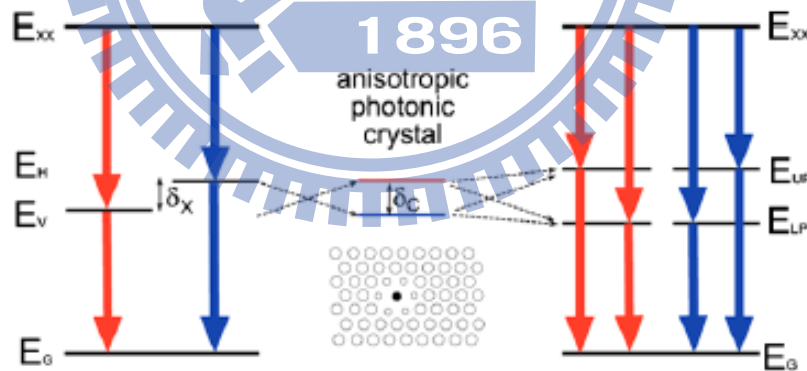


Figure 2.4: Two cavity modes strongly couple to non-degenerated X states. Two groups of degenerate polariton states are formed.

2.3 Magnetic response of quantum structures

The magneto-optical property means that the change in emission characteristics of the radiated light from one material by the presence of an external magnetic field, especially in emission energy. For quantum structures, the magnetic responses are determined by the states of the confined carriers before and after recombination, thus it is associated with the carrier's quantum levels and the Coulomb interaction among them.

2.3.1 Magnetic response of single particle

When a charged particle is confined within a quantum structure under a uniformly external magnetic field \vec{B} along z direction, the Hamiltonian is expressed as

$$H = \frac{1}{2m^*} [\vec{p} - e\vec{A}(\vec{r})]^2 + V_0(\vec{r}) \quad (2.13)$$

, where $V_0(\vec{r})$ is the confined potential, $\vec{A}(\vec{r})$ is vector potential associated with \vec{B} ($\vec{B} = \nabla \times \vec{A}(\vec{r})$), m^* is the effective mass, and e is electron charge. According to the symmetric gauge, i.e., $\vec{A} = \left(-\frac{1}{2}yB_z, \frac{1}{2}xB_z, 0\right)$, the Hamiltonian is expanded as

$$H = H_0 + H_1 + H_2 \quad (2.14)$$

$$H_0 = \frac{1}{2m^*} \vec{p}^2 + V_0(\vec{r}) \quad (2.15)$$

$$H_1 = -\frac{e}{2m^*} \vec{L} \cdot \vec{B} \quad (2.16)$$

$$H_2 = -\frac{e^2 B^2}{8m^*} \hat{\rho}^2 \quad (2.17)$$

, where \vec{L} is the operator of orbital angular momentum. $\hat{\rho}^2$ is the operator of the

vector projection of \vec{r} onto the plane perpendicular to \vec{B} . H_0 is the Hamiltonian as $\vec{B} = 0$, H_1 is the orbital Zeeman term, and H_2 is the diamagnetic term. In quantum mechanics, the total magnetic moment $M = M_1 + M_2$,

$$\vec{M}_1 = \frac{e}{2m^*} \vec{L} \quad ; \quad \vec{M}_2 = -\frac{e^2}{2m^*} \vec{r} \times \vec{A} \quad (2.18)$$

where M_1 is intrinsic magnetic moment, and M_2 is induced magnetic moment. One can see $H_1 = -\vec{M}_1 \cdot \vec{B}$, which represents the coupling energy between orbital angular momentum and magnetic field. In addition, the induced magnetic potential U is written as

$$U = -\int_0^B \vec{M}_2 \cdot \vec{B} dB = -\frac{e^2}{4m^*} (\vec{r} \times \vec{A}) \cdot \vec{B} = -\frac{e^2 B^2}{8m^*} \hat{\rho}^2 = H_2 \quad (2.19)$$

According to Lenz's law, the induced magnetic moment opposes the change of external magnetic flux. Thus the directions of \vec{M}_2 and \vec{B} is opposite, resulting in a positive U . That is why H_2 is called diamagnetic term, the induced magnetic potential is called the diamagnetic shift and associated with the extent of wave function.

For self-assembled InAs/GaAs QDs, they are usually formed the flat geometry analogous to 2-D structure. The Fock-Darwin model, which describes a 2-D disk structure with a parabolic-confined potential $V_0 = \frac{m^* \omega_0^2}{2} (x^2 + y^2)$, can briefly explain the quantum states of single particle in dot. In the presence of a uniform magnetic field $\vec{B} = (0, 0, B_z)$ along z direction, the quantum energy of a carrier confined in this QD can be expressed as follow (see Appendix A)

$$E_{nl} = (2n + |l| + 1) \hbar \left(\omega_0^2 + \frac{1}{4} \omega_c^2 \right)^{1/2} - \frac{1}{2} l \hbar \omega_c \quad (2.20)$$

, where $\omega_c = eB_z/m^*$ is the cyclotron angular frequency, nl are the quantum

numbers in two dimensions. By Taylor series, Eq. 2.20 is expanded by the power of B ,

$$E_{nl}(B_z) = (2n + |l| + 1)\hbar\omega_0 + \left(\frac{e^2\sqrt{\langle\rho_0^2\rangle_{nl}}^2}{8m^*} B_z^2 - \frac{e^4\sqrt{\langle\rho_0^2\rangle_{nl}}^6}{128m^*\hbar^2} B_z^4 + \dots \right) - \frac{e\hbar l}{2m^*} B_z \quad (2.21)$$

$\sqrt{\langle\rho_0^2\rangle_{nl}}$ is the root mean square radius of particle in the state nl at zero magnetic field. In Eq. 2.21, the first term is the eigenenergy at zero magnetic field. The second term is attributed to the diamagnetic shift, if the magnetic length $\ell_M = \sqrt{\hbar/eB_z}$ is much larger than $\sqrt{\langle\rho_0^2\rangle_{nl}}$, the quadratic dependence on magnetic field dominates the diamagnetic shift, and the higher order terms can be ignored, while the diamagnetic shift is inverse to effective mass and proportional to $\langle\rho_0^2\rangle_{nl}$. The third term is the Zeeman effect related with the orbital angular momentum of quantum state, which leads to the splitting of states having opposite angular momentum with increasing magnetic field.

2.3.2 Magnetic response of Coulomb interaction

The external magnetic field alters not only the quantum levels of each carrier confined in quantum structure, but also influences the Coulomb energy among these confined carriers to lead the different magnetic response for excitonic complexes. In Consequence, the transition energy between levels is altered, this well-known magneto-optical effect. Considering the 2-D Fock-Darwin model with an external magnetic field B as mentioned in above section and Appendix A, the wave function of ground state is expressed as

$$\psi_{00}^\alpha = \frac{1}{\sqrt{\pi}l_\alpha} \exp\left[-\frac{r^2}{2l_\alpha^2}\right] \quad (2.22)$$

, where $l_\alpha = \sqrt{\langle \rho_B^2 \rangle_{00}} = \sqrt{\hbar/m} \left(\frac{\omega_c^2}{4} + \omega_0^2 \right)^{-1/4}$ is the root mean square radius of ground state at magnetic field B . Putting Eq. 2.22 into the Coulomb interaction Hamiltonian, the direct Coulomb energy between α and β particle can be given in Eq. 2.23, which has been deduced by Ref. [23,33,34]

$$V_{\alpha\beta}(B) = \frac{e^2}{4\pi\epsilon_0\epsilon_r} \int \int \frac{|\psi_{00}^\alpha|^2 \cdot |\psi_{00}^\beta|^2}{|r_\alpha - r_\beta|} dr_\alpha dr_\beta = \frac{e^2}{4\pi\epsilon_0\epsilon_r} \sqrt{\frac{\pi}{2}} \frac{1}{l} \quad (2.23)$$

, where $l = \sqrt{(l_\alpha^2 + l_\beta^2)/2}$. Via Taylor series, Eq. 2.23 is approximated to

$$V_{\alpha\beta}(B) = V_{\alpha\beta}(0) + \frac{e^2}{4\pi\epsilon_0\epsilon_r} \cdot \frac{e^2}{16\hbar^2} \sqrt{\frac{\pi}{2}} \cdot \frac{l_\alpha^6 + l_\beta^6}{2l^3} \cdot B^2 + \dots \quad (2.24)$$

Comparing Eq. 2.24 with Eq. 2.21, we see that the quadratic coefficients of single particle energy and Coulomb energy are proportional to l^2 and l^3 , respectively. Thus we can speculation that, for weak confinement, the magnetic response of Coulomb energy becomes more important, and total diamagnetic diamagnetism is more complicated. For neutral exciton, the diamagnetic shifts have report to exhibit a conventional quadratic dependence on magnetic field for InGaAs dot or GaAs well, so on [35, 36, 37]. In particular, it has been theoretically predicted that a weakly confined negative trion (X^-) in large-size QDs would exhibit a negative magnetic dispersion [24]. However, such an unusual behavior of X^- has not yet been observed in past works focused on charged trions in QD system [25,26].

2.4 Concept of photonic crystal and cavity

The concept of Photonic Crystal (PhC) was first proposed by Yablonovitch [38] and John [39] in 1987. PhC is a micro-structure consisted of materials with periodic refractive indices, hence it can form its own photonic band-structure similar to that of solid crystal arrayed by periodic atoms. By the different dimensions, photonic crystal can be classified as one, two or three dimensional structure as shown in Fig. 2.5. One of the many advantages of PC is that, one can change its photonic band-structure for controlling the characteristics of propagating light within PC such as wavelength, phase and polarization by adjusting the periodic structure artificially. Furthermore, Photonic Crystal cavities (PhC cavities), the artificial defects are purposely putted into the photonic crystal, have also been applied on many areas, including low-threshold nano-lasers [5,6], optic filters with waveguides [7,8] and cavity quantum electrodynamics because of their excellent photon confinement within tiny volume. For these defects, the original symmetry and periodicity are broken so that the defect modes are form in the resonant cavities. Via specific designing, the defect modes are possibly changed and controlled.

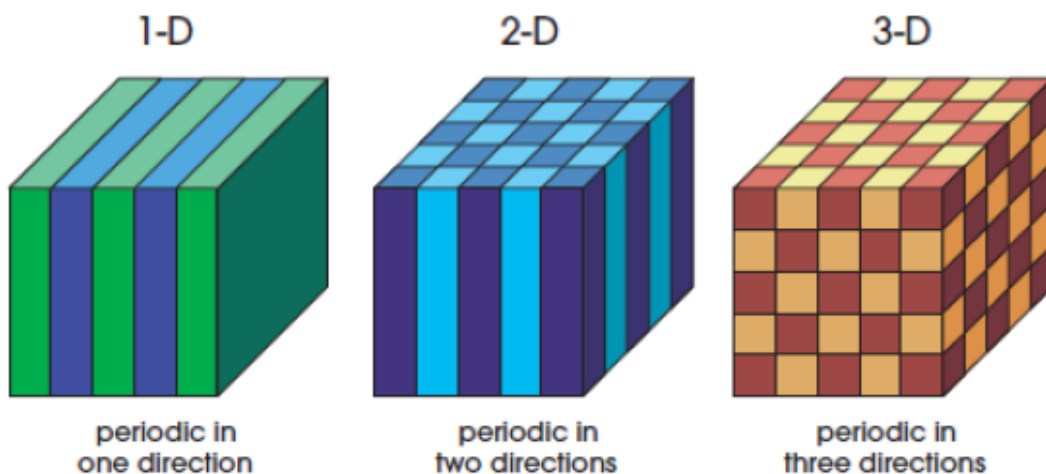


Figure 2.5: The illustrated scheme of one, two and three dimensional PhC.

Because 2-D PhC can provide excellent compatibility for fabricated process, it is often used for integrating with optic-electric devices. Many types of 2-D cavities have been demonstrated such as H1, H2 and L3 cavities in triangular lattice. Fig. 2.6 plots their geometry and fundamental modes (taken from Ref. 40).

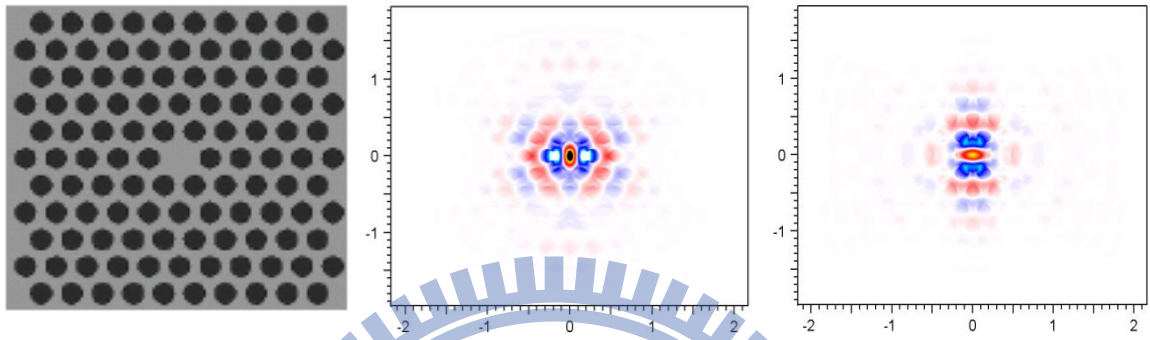


Figure 2.6(a): The H1 cavity and its two fundamental modes: Horizontal and Vertical dipole mode.

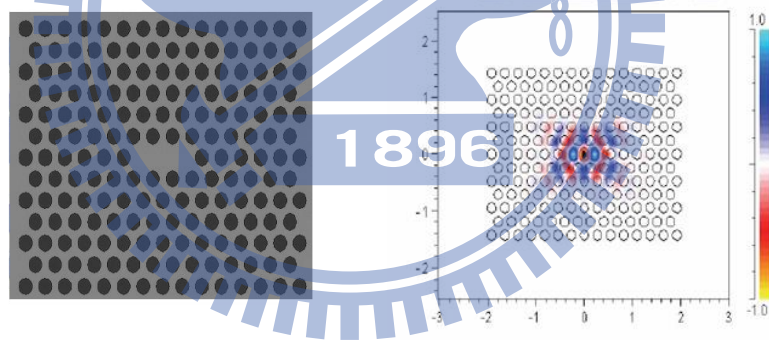


Figure 2.6(b): The H2 cavity and its fundamental modes: monopole mode.

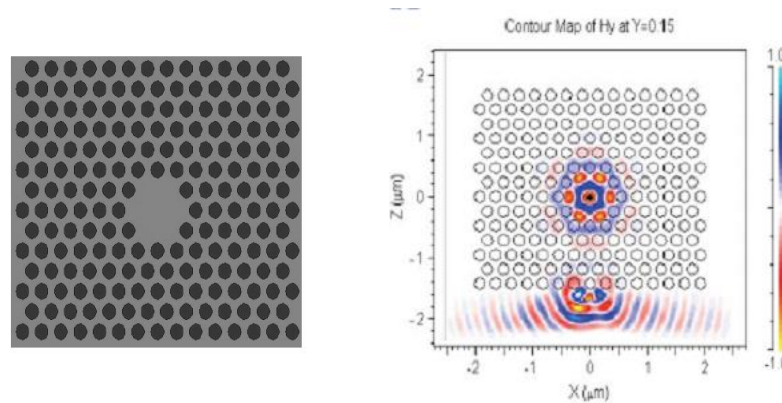


Figure 2.6(c): The L3 cavity and its fundamental modes.

2.5 Photonic Crystal fundamental theorem

The photon behavior in photonic crystal can be described by Maxwell equation. If there is no free charge or current in this system, Maxwell equation can be represented as follows,

$$\nabla \times \vec{E}(r, t) = -\mu_0 \frac{\partial \vec{H}(r, t)}{\partial t} \quad (2.25)$$

$$\nabla \times \vec{H}(r, t) = \varepsilon_0 \varepsilon_r(\vec{r}) \frac{\partial \vec{E}(r, t)}{\partial t} \quad (2.26)$$

$$\nabla \cdot (\varepsilon_0 \varepsilon(\vec{r}) \vec{E}(r, t)) = 0 \quad (2.27)$$

$$\nabla \cdot (\mu_0 \vec{H}(r, t)) = 0 \quad (2.28)$$

where \vec{r} is the position vector, ε_0 and μ_0 are vacuum permittivity and permeability, and $\varepsilon_r(\vec{r})$ is the relative dielectric constant at position \vec{r} . If we consider fields as harmonic modes which vary sinusoidally with time, they can be written as,

$$\vec{E}(r, t) = \vec{E}(r) e^{-i\omega t} \quad (2.29)$$

$$\vec{H}(r, t) = \vec{H}(r) e^{-i\omega t} \quad (2.30)$$

Inserting Eq. 2.29 and 2.30 into Eq. 2.25-2.28 and eliminating time factor of $e^{-i\omega t}$, we can obtain

$$\nabla \times \vec{E}(r) = i\omega \mu_0 \vec{H}(r) \quad (2.31)$$

$$\nabla \times \vec{H}(r) = -i\omega \varepsilon_0 \varepsilon_r(r) \vec{E}(r) \quad (2.32)$$

$$\nabla \cdot (\varepsilon(r) \vec{E}(r)) = 0 \quad (2.33)$$

$$\nabla \cdot (\mu_0 \vec{H}(r)) = 0 \quad (2.34)$$

Combining Eq. 2.31 and Eq. 2.32, they can be rewritten into

$$\nabla \times \left(\frac{1}{\epsilon_r(r)} \nabla \times \vec{H}(r) \right) = \frac{\omega^2}{c^2} \vec{H}(r) \quad (2.35)$$

Eq. 2.35 is a problem of eigenfunction. To solve it, all orthogonal eigenvalues ω and its corresponding eigenfunction $H(\vec{r})$ can be gotten. $H(\vec{r})$ tells us the variation of magnetic field with position, i.e., characterize the light wave how to propagating in this structure. Hence we can extract the wave vector \vec{k} from $H(\vec{r})$, and the band structure can be plotted according to obtained ω and \vec{k} . One of the principal characteristics for PhC is the photonic band gap (PBG). Fig. 2.7 shows the TE mode band structure of an air-hole triangular lattice on a GaAs membrane calculated using FDTD method. The lattice period is 260 nm, and the air-hole radius is 65 nm. Obviously a photonic band gap (PBG) forms between two bands (the shadow region), in which no eigensolution exists. This is, photon with the frequency in PBG cannot propagate with such PhC structure. If one air-hole of above PhC is removed, a point-defect named H1 cavity would be formed. And a defect state of a specific frequency appears within the range of PBG and ranges over total \vec{k} space as shown in Fig. 2.8. It means that photon in the specific frequency is confined in the defect region.

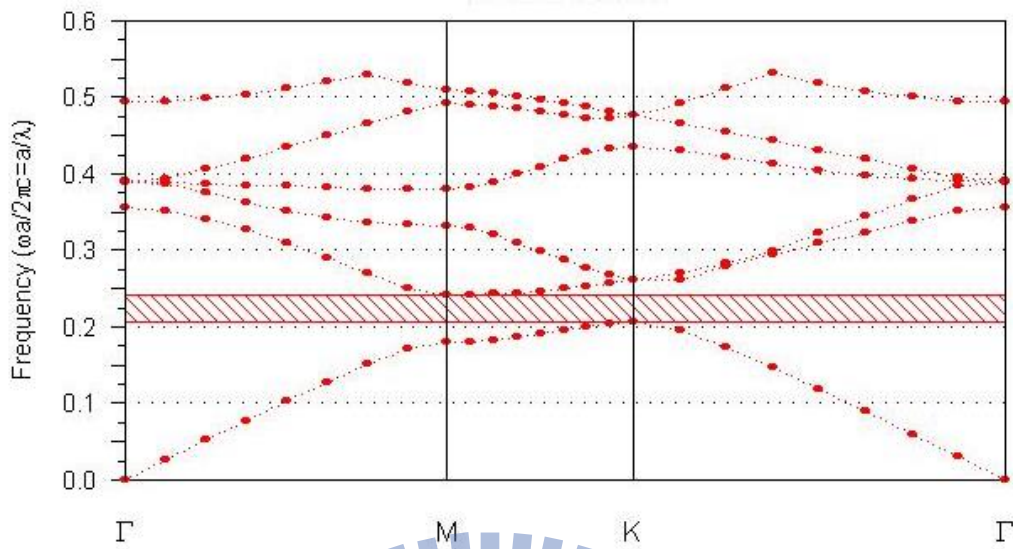


Figure 2.7: A calculated TE mode band structure of an air-hole triangular lattice on a GaAs membrane with period=260 nm and air-hole radius=65 nm, this calculation uses FDTD method. The shadow region is so-called photonic band gap (PBG).

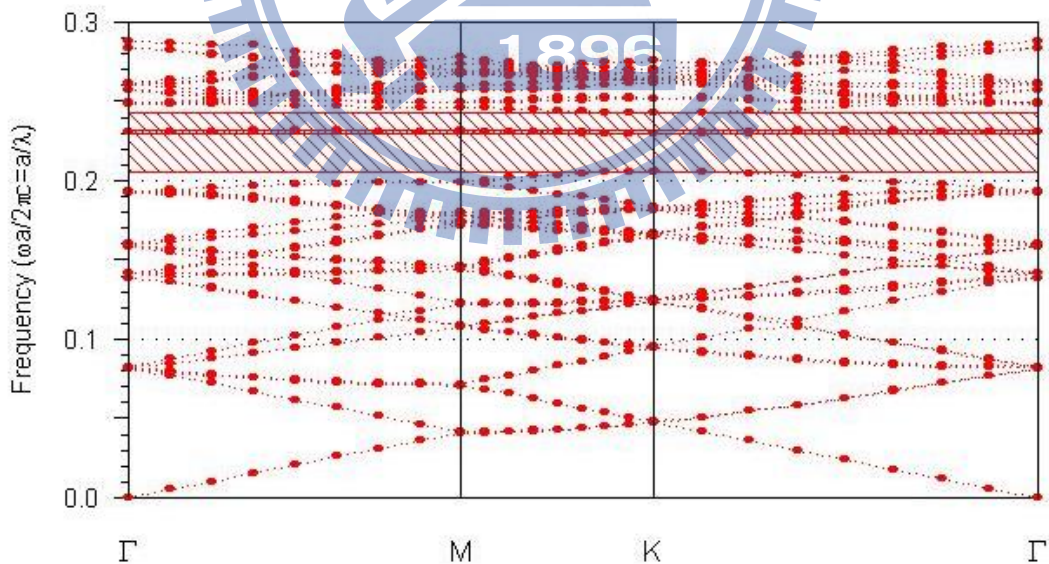


Figure 2.8: The calculated TE mode band structure of a point defect PHC cavity formed by removing one hole in a perfect air-hole triangular lattice. A defect mode appears in the range of P BG.

2.6 Light-matter interaction : Jaynes-Cummings model

Consider a cavity-emitter coupling system as shown in Fig. 2.9. An emitter having two levels, ground state ($|g\rangle$) and excited state ($|e\rangle$), is placed within a resonant cavity. Because resonant mode is a quantum mechanical harmonic oscillator, the energy of electromagnetic field can be quantized. When the emitter couples to resonant mode (their emission energy are very close), the spontaneous emission rate of the emitter becomes rapider through Purcell effect, i.e., the excited state decays to ground state by another way of releasing energy to the resonant mode of high density state so that the rate is accelerated. If the coupling strength is strong enough to achieve the strong coupling regime, the photon energy is exchanged fast between the emitter state and cavity mode. A physical model, Jaynes-Cummings model, can describe that the emitter how to interact with the resonant mode in the cavity. By Jaynes-Cummings model, the Hamiltonian of the full system can be written as Eq. 2.36

$$H_{JC} = \hbar\omega_c \hat{a}^+ \hat{a} + \hbar\omega_a \frac{\hat{\sigma}_z}{2} + g \cdot (\hat{a}^+ \hat{\sigma}_- + \hat{a} \hat{\sigma}_+) \quad (2.36)$$

The three terms represent the free field Hamiltonian, emitter excitation Hamiltonian and interaction Hamiltonian, respectively, where \hat{a}^+ and \hat{a} are the bosonic creation and annihilation operators of the radiation field, and ω_c is the angular frequency of the resonant mode. The operator $\hat{\sigma}_z = |e\rangle\langle e| - |g\rangle\langle g|$ is the inversion operator, $\hat{\sigma}_+ = |e\rangle\langle g|$ and $\hat{\sigma}_- = |g\rangle\langle e|$ are the raising and lowering operators of the emitter, and ω_a is the transition energy between ground and excited states of the emitter. One most important factor of the coupling strength, g , is given by $\vec{d} \cdot \vec{E}(\vec{r})$, here \vec{d} is the transition dipole moment of the emitter, and $\vec{E}(\vec{r})$ is electric field of the resonant mode at the position \vec{r} , of which the maximum satisfies $|\vec{E}_{max}| = \sqrt{\hbar\omega_c/2n^2\varepsilon_0V}$. Here n is the material refractive index, ε_0 is the vacuum permittivity, and V is the

mode volume. The physical meaning of g is the rate of energy exchange between the emitter and resonant mode, which is connected to the strength of the transition dipole moment, the position of the emitter within the cavity, and mode volume. To solve this eigen-problem, the Hamiltonian matrix can be decomposed into a block of 2×2 matrix on the basis of two states $|N$ and $|N + 1, g\rangle$ as Eq. 2.37, here N is photon number in cavity,

$$H_{JC} = \hbar \begin{pmatrix} N\omega_c + \frac{\omega_a}{2} & g\sqrt{N+1} \\ g\sqrt{N+1} & (N+1)\omega_c - \frac{\omega_a}{2} \end{pmatrix} \quad (2.37)$$

Diagonalizing this matrix, its eigenvalues, E_+ and E_- , are gotten,

$$E_{\pm} = \hbar\omega_c \left(N + \frac{1}{2} \right) \pm \frac{1}{2} \sqrt{\delta^2 + \Omega_n^2} \quad (2.38)$$

Where $\delta = \hbar\omega_a - \hbar\omega_c$ and $\Omega_n = 2g\sqrt{N+1}$ are defined as the energy detuning and the Rabi splitting with N photon in cavity, respectively. Further, considering the line widths of resonant mode and the emitter, γ_c and γ_a , which are proportional to the emitter's spontaneous emission rate and the cavity's energy loss rate. Eq. 2.38 becomes,

$$E_{\pm}(\delta) = \hbar\omega_c \left(N + \frac{1}{2} \right) - i \frac{\gamma_c + \gamma_a}{2} \pm \frac{1}{2} \sqrt{\Omega_n^2 - \frac{(\gamma_c - \gamma_a - 2i\delta)^2}{4}} \quad (2.39)$$

When the detuning δ is zero, the difference between the two eigenvalues, ΔE , would be the smallest splitting between two emission line observed in experiment.

$$\Delta E(0) = \sqrt{\Omega_n^2 - \frac{(\gamma_c - \gamma_a)^2}{4}} \quad (2.40)$$

To enter the strong coupling regime, the small mode volume and high Q factor are

necessary so that the energy exchange rate between the emitter and cavity mode is rapid enough to overcome the emitter's spontaneous emission rate and the cavity's energy loss rate. In this case, the emitter and cavity mode are hybridized into the polariton states.

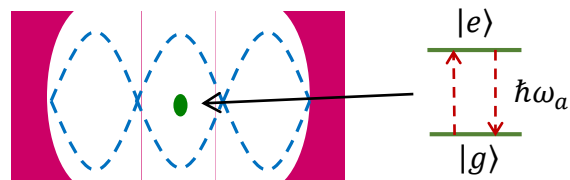
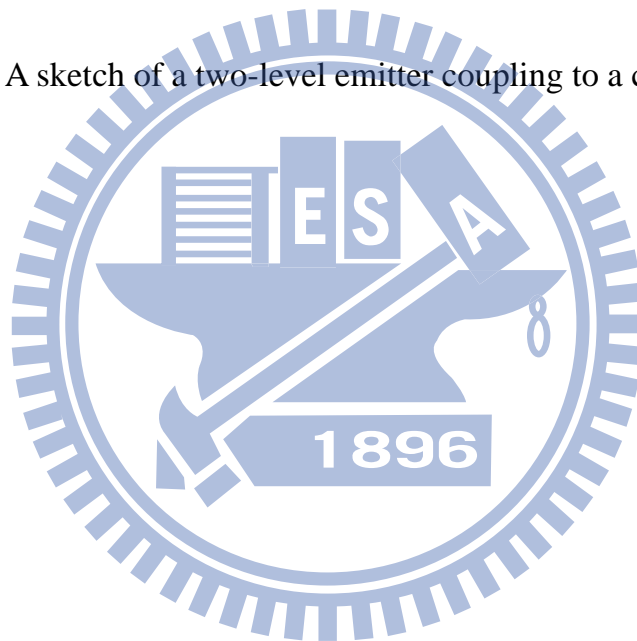


Figure 2.9: A sketch of a two-level emitter coupling to a cavity resonator.



Chapter 3 Fabrication and Experiment/Simulation techniques

3.1 The growth of InAs/GaAs quantum dot

The investigated samples of InAs self-assembled quantum dot (2.0 MLs) were grown on a GaAs (100) substrate by a Varian Gen II molecular beam epitaxy system. First we grew a GaAs buffer layer about 100 nm for smoothing the sample surface and resisting the defects from substrate, sequentially grew a 100 nm undoped GaAs layer, and then used the Stranski-Krastanow mode to form InAs QD at 480 °C, where InAs source was deposited on GaAs layer to form a 2-D heterostructure called wetting layer, because of the lattice mismatch between InAs and GaAs, the strain gradually accumulated with increasing the thick of wetting layer until it could not be sustained and released to form 3-D dotted structure. In the process of growth, the sample was not rotated, yielding a gradient in dot density on the wafer due to different distances from In source (In effusion cell). Finally, the InAs QDs were capped by a 100 nm undoped GaAs layer as the barrier material, the structure of this sample (Lm4596) is illustrated in Fig. 3.1(a). From the AFM images of Lm4596, which has reported in Ref. 41, shown in Fig. 3.2. We can see that the QD density distributes over the range from 10^8 to 10^{11} cm⁻², corresponding to different positions of the sample. Meanwhile, Ref. 41 also reported the PL spectra of the regions with different QD density in Lm4596 as shown in Fig. 3.3, which indicates the signals of QD and wetting layer. On the other hand, for manufacturing PhC cavities, an adding 1.2 μm thick Al_{0.9}Ga_{0.1}As was grown onto the buffer layer of the sample Lm5217 before growing QDs to be a sacrificial layer, its structure is illustrated in Fig. 3.1 (b).

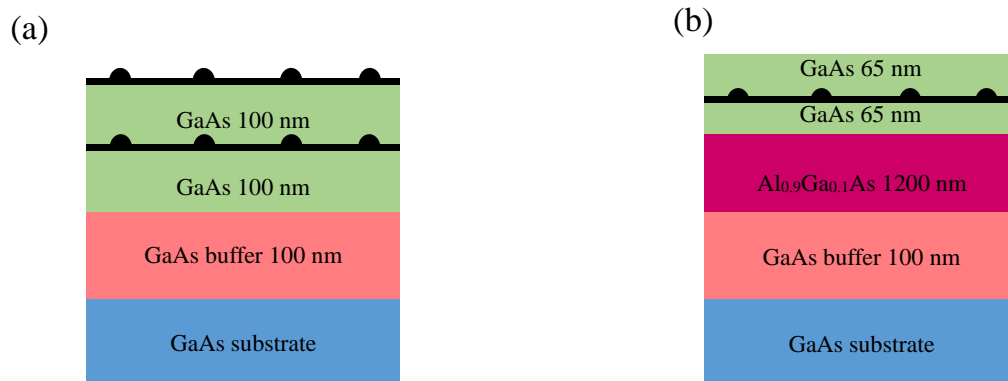


Figure 3.1: The structures of the samples embedded in InAs/GaAs QDs. (a) Lm4596 for single QD study (b) Lm5217 for PhC cavity study.

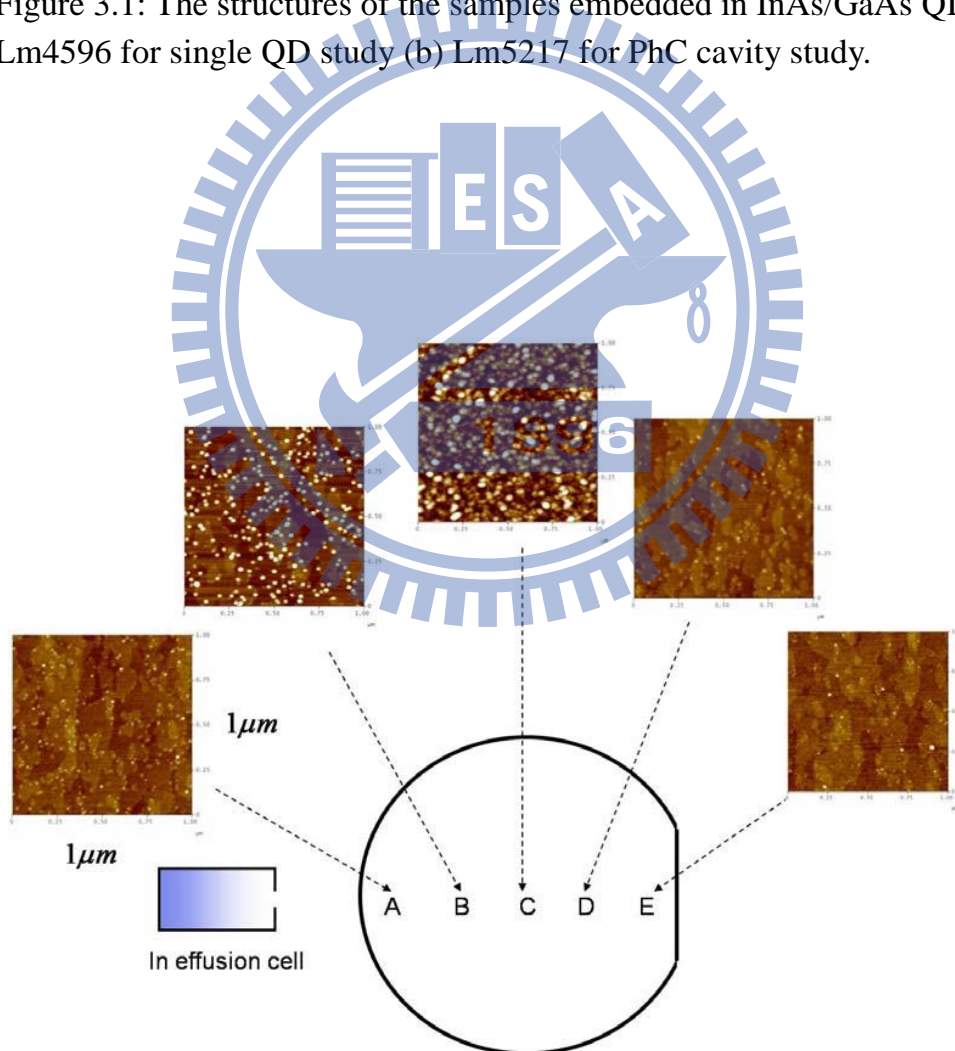


Figure 3.2: The AFM images of the sample Lm4596.

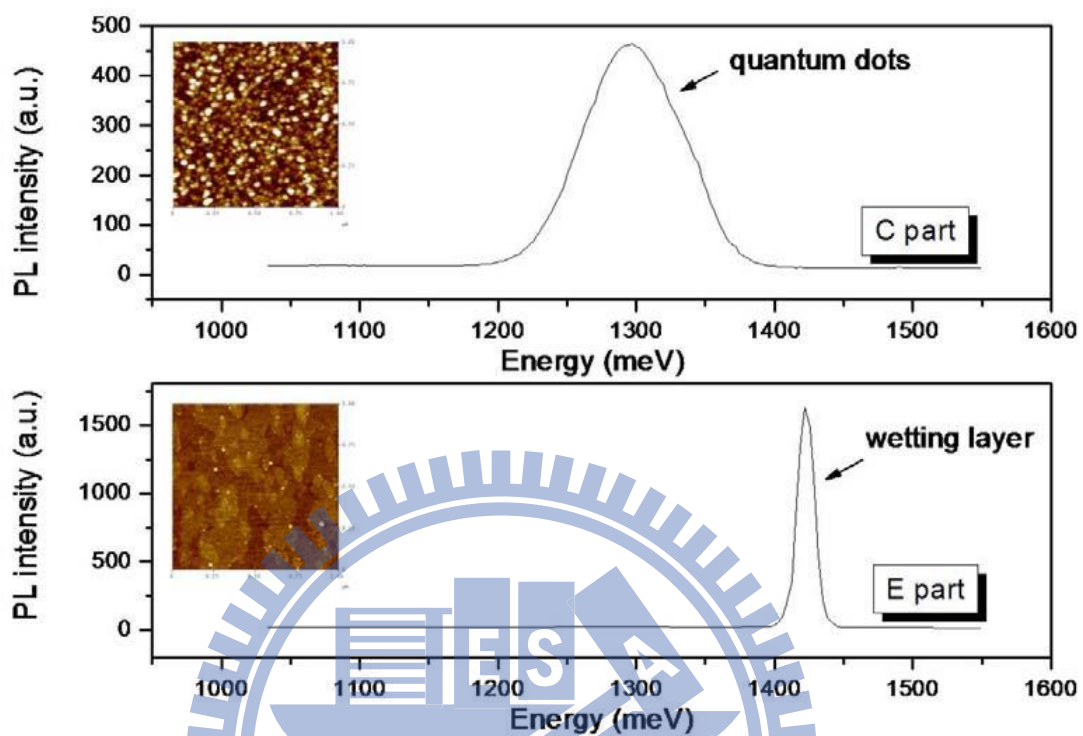


Figure 3.3: The PL spectra of the regions with different QD density in the sample Lm4596.

3.2 Fabrication of Aluminum apertures on QD sample

In order to indeed observe the individual QD, we took a specific process on the InAs QDs sample (LM4596). The hollow apertures immersed in an Al layer were manufactured on the sample surface, we expected only one QD under each aperture. If so, there is only one QD to be excited in μ -PL measurement because laser cannot penetrate these areas covered with Al. Fig. 3.4 shows the diagram of process flow, and the fabricated steps are as follows,

(1) Deposition of the Al layer:

First we used an electron-gun evaporator to deposit an Al film about 100 nm upon the sample after growing.

(2) PMMA resist coating:

A resist layer of poly methyl methacrylate A5 (PMMA A5) was coated about 300 nm upon the Al film. The spin condition are distinguished into two steps, spin time and speed are that 10s / 1000RPM for the first step, and 25s / 6000RPM for the second step.

(3) E-beam writing:

We used an E-beam Lithography System (ELS-7500EX) to define the patterns of apertures on the PMMA resist. The E-beam Lithography System was operated on accelerated voltage of 50 kV and emission current of 50 pA.

(4) Development:

After Lithography, the sample was immersed in a MIBK solution of 25 °C for 70s to develop the resist, and then dried by a hot plate at 180 °C for 90s.

(5) DHF wet etching:

Putting the sample inside DHF solution to etch the part of Al film which was not

covered by PMMA and cleaning the sample by DI water. Then, the aperture patterns were transferred to Al layer so that the hollow apertures were formed.

(6) Removing the PMMA resist:

Finally, we clean the sample in ACE solution for removing the remnant PMMA.

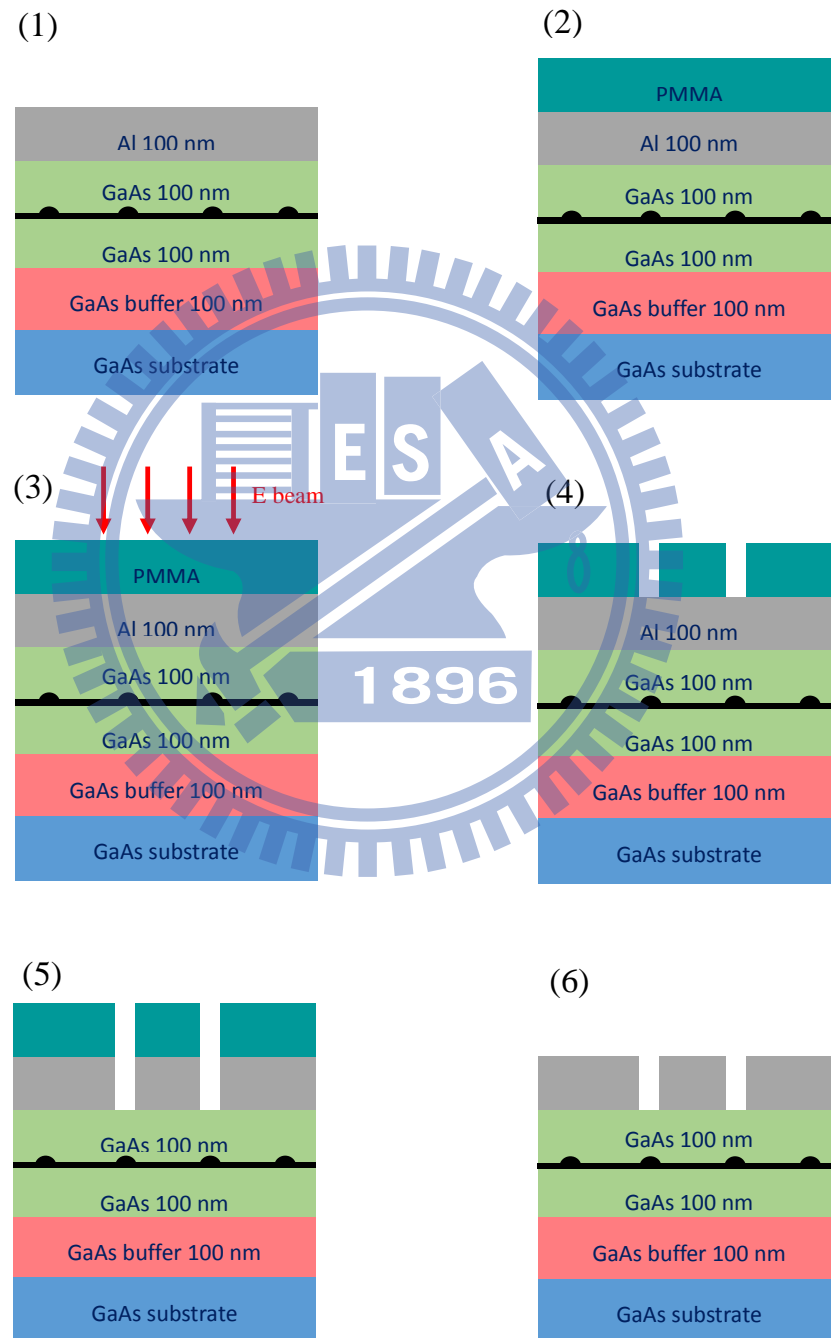


Figure 3.4: The process flow of Al aperture on the sample Lm4596

3.3 Fabrication of photonic crystal cavity

In this section, we interpret the fabrication of 2-D PhC cavities based on the InAs/GaAs self-assembled QDs sample. The sample (LM5217) was also grown by a Varian Gen II molecular beam epitaxy system with solid sources as mentioned in section 3.1, its epitaxy structure mainly consists of a 1.2 μm thick $\text{Al}_{0.9}\text{Ga}_{0.1}\text{As}$ sacrificial layer and an active InAs QDs layer centered at 130 nm GaAs layer (see Fig. 3.1 (b)). To fabricate the PhC cavity, we took the followed process steps as illustrated in Fig. 3.5.

(1) Hard mask deposition :

First we deposited a SiN_x layer about 200 nm as hard mask upon the sample by using a plasma-enhanced chemical vapor deposition (PECVD) system.

(2) PMMA resist coating :

A PMMA (A5) of about 300 nm was coated on the SiN_x layer, and the spin parameters are the same as that mentioned in section 3.2.

(3) Defining the patterns of PhC cavities (Ebeam writing and development) :

The photonic crystal cavities were patterned on PMMA resist using the E-beam Lithography System which were also operated on accelerated voltage of 50 kV and emission current of 50 pA. Sequentially, the sample was also developed in MIBK solution.

(4) Patterns transference from PMMA to SiN_x layer :

An inductively coupled plasma/reactive ion etching (ICP/RIE) system was used to etch the SiN_x , resulting in transferring the PhC patterns from PMMA to SiN_x layer by using gases O_2/CHF_3 .

(5) Patterns transference from SiN_x layer to GaAs layer:

By this ICP/RIE system, the patterns were again transferred from SiN_x layer to GaAs cavity layer by using gases of Ar/SiCl₄ to etch the GaAs.

(6) Removing the sacrificial layer :

Finally, the suspending membrane was released by etching the sacrificial layer with DHF solution. Here we added tiny surfactant antifoaming agent in DHF solution because such addition could assist to take away the remnant product in etch process [42,43]. The used surfactant antifoaming agent in this process was Benzalkonium chloride (BKC). By adding BKC, the etch rate became slow obviously, and the etch uniform was dramatically improved. The DHF solution consisted of HF, BKC and H₂O by the ratio of HF : BKC : H₂O = 1 : 1 : 100.

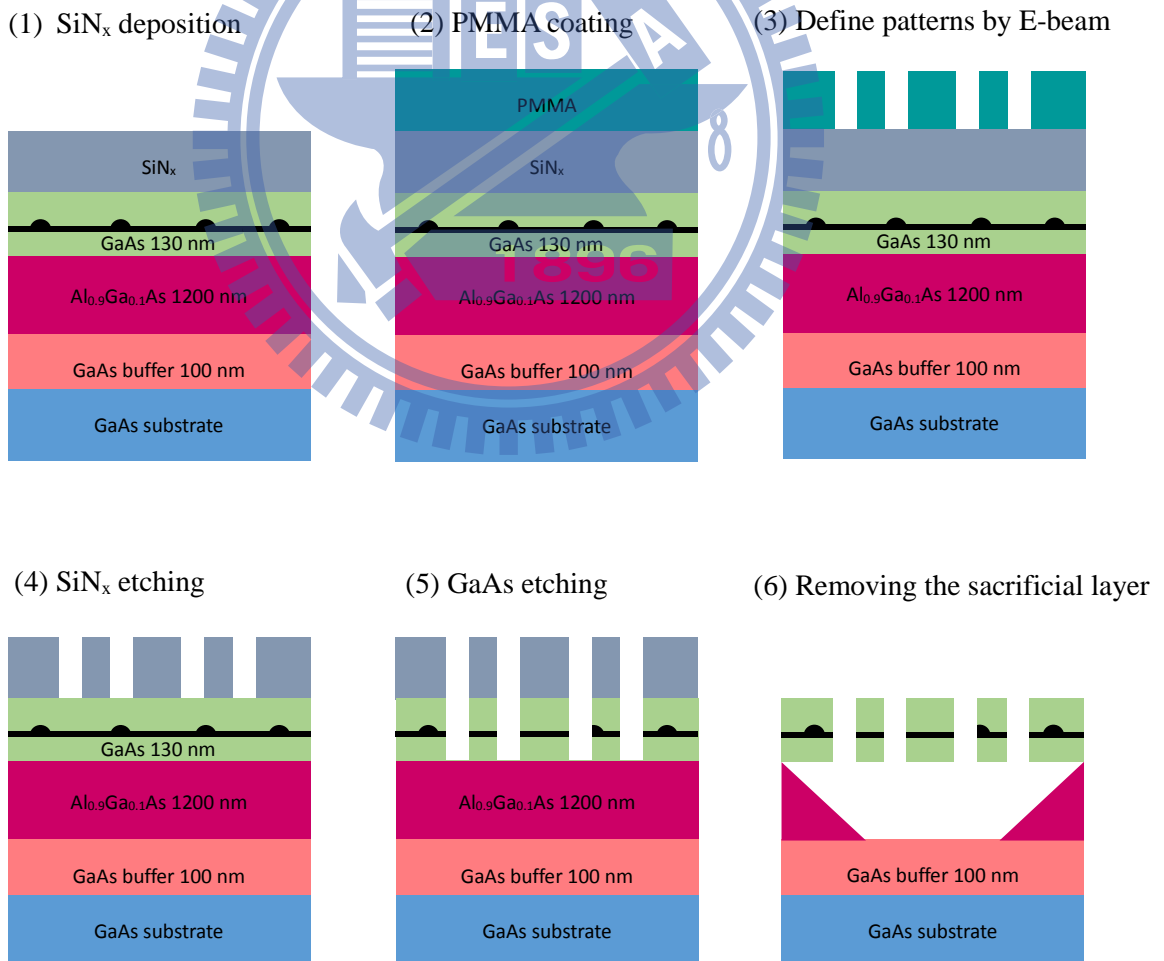


Figure 3.5: The process flow of PhC cavity on the sample Lm5217.

3.4 Conventional photoluminescence setup

The photoluminescence (PL) system is an effective and convenient tool to investigate the intrinsic physical properties of materials. The basic concept is that the laser light is used to optical-excited the sample to its excited state, and then the sample decay from the excited state to the ground state with generating a photon. For quantum structures, such as quantum dot and quantum well, the emission can reveal many fundamental properties, such as band gap and electronic structure.

The sketch of the conventional PL setup is depicted in Fig. 3.6. The sample is mounted on a helium close-cycle cryostat for cooling to low temperature about 15 K. An Argon laser with wave length of 488 nm passes a chopper with specific frequency and excites the investigated sample. The radiative photoluminescence is focused as parallel light by a lens, and then focused into the slit of monochromator by passing through another lens. Sequentially, the photoluminescence is dispersed through a grating of 0.55 m long, and detected by an InGaAs detector, of which the detection wave length can be ranging from 830 nm to 1650 nm. Due to the modulated laser beam by the chopper, the detected PL signals also have been modulated by the same frequency. A Lock-in Amplifier is used to enlarge the PL signals with the chopper's frequency to filter out the environmental noise.

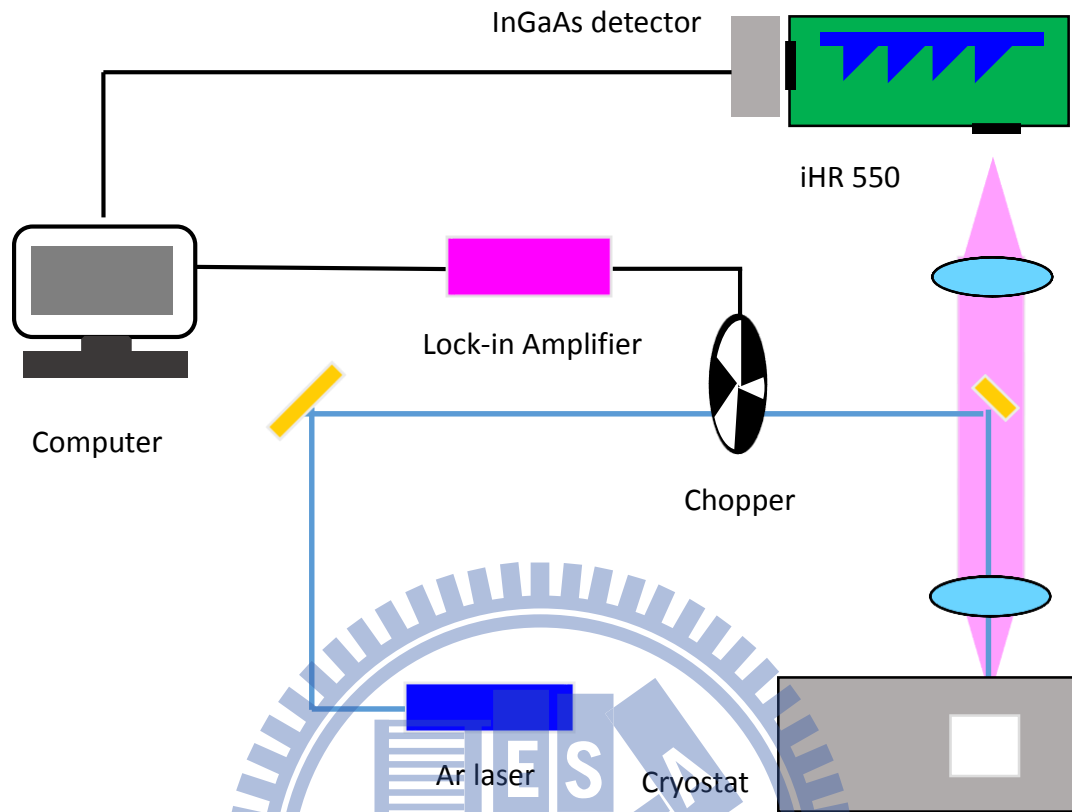


Figure 3.6: The framework of the conventional PL setup.

3.5 Micro-photoluminescence setup

In this dissertation, we mainly used a specially designed micro-photoluminescence setup (μ -PL) to observe the device with micro-scaled area, including the individual QD and PhC cavities because of its small laser spot size about $4\mu\text{m}^2$. The framework of the μ -PL setup is shown in Fig. 3.7 (a). A He-Ne laser, of which the wavelength is 632 nm shorter than that of the wetting layer (about 870 nm in our sample), was used as the optical-pumped source. The laser beam passed through an attenuator to tune the excited power, and then was split into two beams by the beam splitter. Transmitted beam entered the power meter to detect the excited power, and reflected beam was focused onto the sample through a 100 X microscope objective (NA=0.5) which could concentrate the spot size to about $4\mu\text{m}^2$. The photoluminescence (PL) radiated from

the excited sample was collected by the identical objective, and then passed through a series of optic components including $\lambda/2$ or $\lambda/4$ wave plate and linear polarizer, finally arrived at the monochromator. After entering the monochromator, the PL signals were dispersed through a grating of 0.75 m long and 1200 g/mm and then detected by a Si liquid-nitrogen-cooled charged coupled device camera (Si CCD), which connected to the exit of the monochromator. The CCD yield a resolution limited spectral linewidth of about 60 μeV and a detected range of spectral wave length of from 400 to 1100 nm.

When beginning the measurement, the samples were mounted on a cryostat, which could be cooled down to 4 K by liquid helium and maintained in such low temperature environment. Moreover, to avoid the solidification of steam, we pumped the internal pressure of the cryostat chamber to 2×10^{-5} Torr before cooling down. On the other hand, for the magneto- μPL measurement, the cryostat chamber was inserted in the bore of superconducting magnet which can supply an external magnetic field (0T—6T) normal to the cryostat. The magneto- μPL measurement are operated by the magneto- μPL system provided by Prof. Wen-Hao Chang lab in Department of Electrophysics, National Chiao Tung University.

In addition, the cryostat chamber was fixed on a three axes motor stage for accurately controlling the position of the sample. A white light beam arising from a mercury lamp was led into the microscope objective after passing through a beam splitter, and then illuminated on the sample. The light reflected from the sample was collected to a CCD and imaged on the computer. In the image, we could see if the laser beam was focused onto the positions that we wanted to observe. By tuning the three axes motor, we could control the position of the sample so that the laser beam was accurately focused onto the hollow Al apertures or PhC cavities as shown in Fig. 3.7 (b).

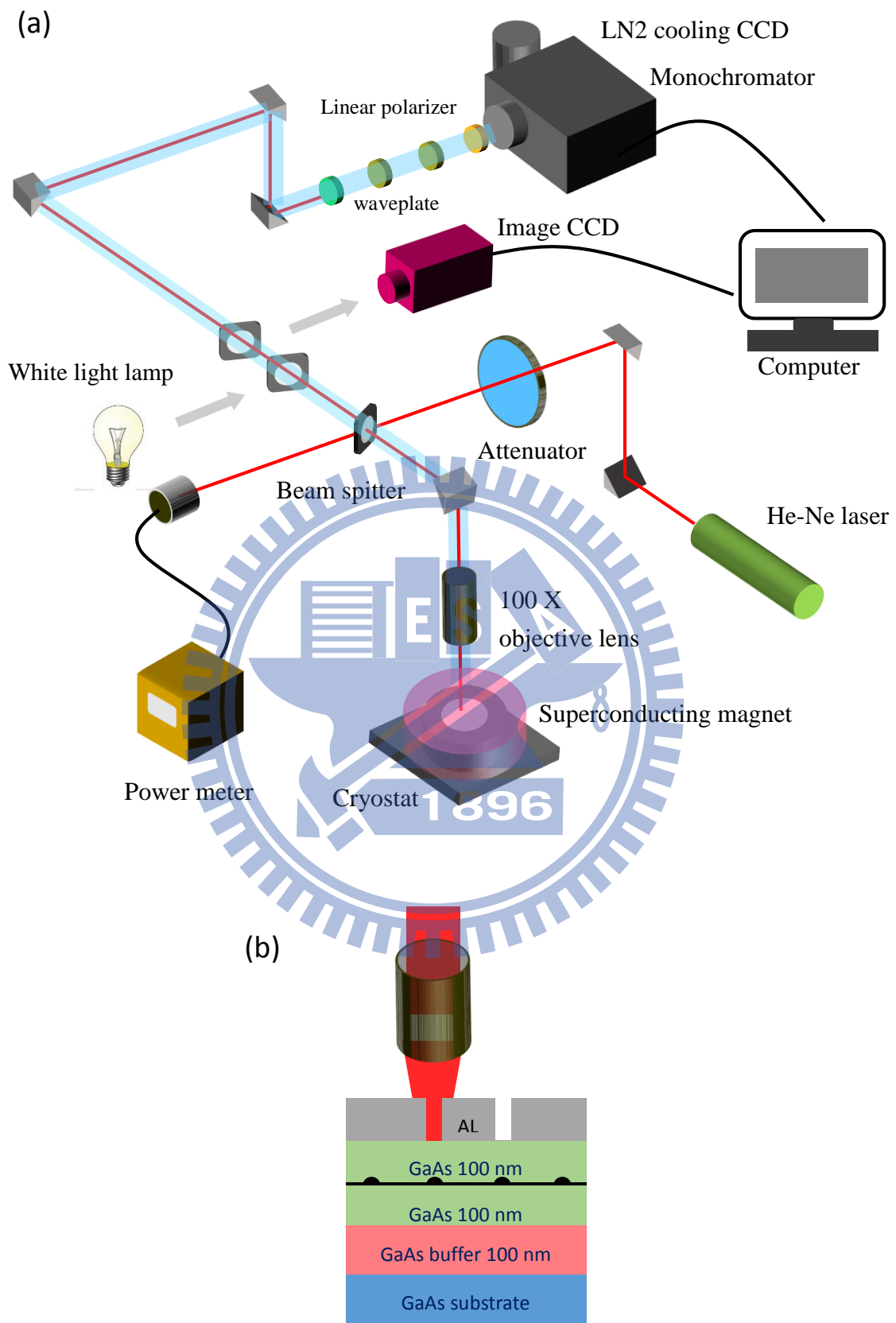


Figure 3.7: (a) The framework of the μ -PL setup. (b) The laser beam is focused onto the Al aperture.

3.6 Finite-element method (fem) : Comsol Multiphysics

Finite element method (FEM) is a numerical method for solving the partial differential equations. Via the discretization of the space, the problem can be simplified to a matrix equation with finite unknown numbers. Comsol Multiphysics is a commercial software based on finite element method, in this dissertation, we use it to calculate the quantum levels of QDs and the electric potentials induced by carriers by solving one-band Schrodinger equation and Poisson equation. The calculations for the emission energies of excitonic complexes will be interpreted in section 4.3.

3.7 Finite-difference time domain (FDTD) method : Rsoft

In addition, we also use another commercial simulation software (Rsoft, Fullwave mode), which is based on finite-difference time domain (FDTD) method, to simulate the PhC structures. FDTD is a time domain method to solve partial differential equations, for which the time-dependent Maxwell's equations (Eq. 2.25 and 2.26) are discretized using central difference approximation in spatial and time domain. When operating Rsoft, we depict the structure of PhC and input the material parameters. Then, a Gaussian pulse is placed in the middle of the cavity as an excited light source as shown in Fig. 3.8. With the PML boundary condition, we get the solutions of electric field profile, Q factor and mode volume by using its built-in tool Q-finder, a fast harmonic analysis.

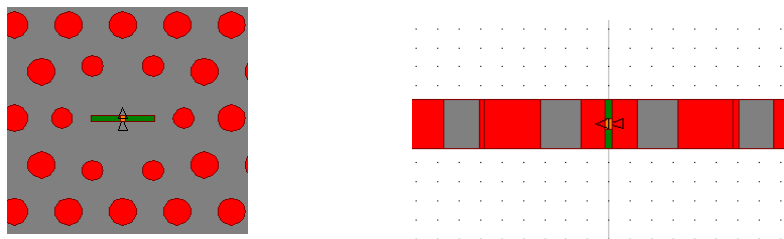


Figure 3.8: The top/side view of the calculated H1 cavity structure (left/right). The orange arrow is the excited Gaussian pulse.

Chapter 4 *Magnetic response of single InAs QD*

In this Chapter, we report the measured magnetic response of single InAs QD, when the external magnetic field was applied along the grown direction of sample (Faraday geometry). The sample is studied via the μ -PL measurements. The typical characteristics of Zeeman and diamagnetic effect are observed and discussed. Moreover, we propose a numerical simulation to explain the diamagnetic behaviors.

4.1 Micro- photoluminescence results

After the fabrication of the sample, we carried out the μ -PL measurements for the apertures on the sample LM4596 maintained at the low temperature 8 K in non-magnetic field environment. Fig. 4.1 shows the spectra excited from seven different apertures at the areas with appropriate QDs density. Clearly, each one of these spectra has only four peaks in measured range. We conjecture that each group of four peaks all belongs to the same QD, and arise from the emissions of four excitonic complexes, negative trion (X^-), neutral exciton (X), biexciton (XX), and positive trion (X^+) from low to high energy, respectively. To confirm such scenario, we execute the power-dependent and polarization-resolved PL measurement, which can tell us the identity of each peak and will be discussed latter. In Fig. 4.1, we shifted all spectra to fix the X emission energies at 0, the actual X emission energies were noted in the right of the figure, which distributes over the range from 1340 to 1382 meV. Take note of the binding energies of X^- , XX , and X^+ , which are defined as

$$E_{X^-}^b = E_X - E_{X^-} = V_{eh} - V_{ee} \quad (4.1)$$

$$E_{XX}^b = E_X - E_{XX} = 2V_{eh} - V_{ee} - V_{hh} \quad (4.2)$$

$$E_{X^+}^b = E_X - E_{X^+} = V_{eh} - V_{hh} \quad (4.3)$$

One can clearly see that $E_{X^-}^b$ are about 6 meV identical for all QDs, however, E_{XX}^b and $E_{X^+}^b$ are both negative and have the same variation trend with different QDs. According to the report of Ref. [23], due to the signs of binding energies, we can know the nonequivalent Coulomb energies, $V_{hh} > V_{eh} > V_{ee}$. It suggests that the wave function of hole is more concentrated inside QDs, thus the change of hole wave function induced by the variation of QD's size is larger than that of electron, which causes more obvious change in V_{hh} for different QDs and then reflects in the variation of E_{XX}^b and $E_{X^+}^b$.

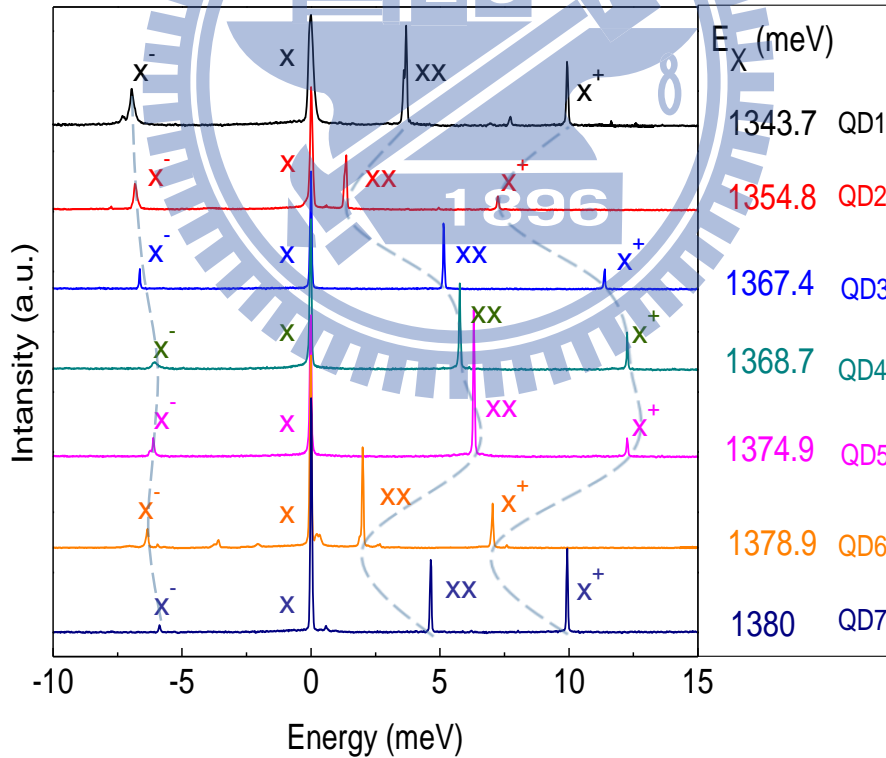


Figure 4.1: The measured micro-PL spectra of seven different apertures in Lm4596.

4.1.1 Power-dependent measurement

In this part, we observed the change of signal intensities when varying the laser excitation power. The amount of excited carriers dominates the occupied states. For low excitation power, the few carriers have no enough possibility to fill the XX state before the recombination of electron-hole pair in X state, hence the X signal is stronger than the XX signal. With increasing the excitation power, the excited carriers become more and can fill the XX state that results in the rapid raise of the XX signal. Fig. 4.2 (a) and 4.3 (a) are the spectra excited by the power from 43 nW to 10 μ W for QD3 and QD5, as expected, the XX signal rapidly raise with increasing the excitation power, finally far more than the X signal. According to reference [23], the relation of intensity I and the excitation power P can be written as,

$$\text{Log}(I) = m\text{Log}(P) + \text{Log}(c) \quad (4.4)$$

m is the number of e-h pair, and c is a constant. We plot the PL signal intensity for each excitonic complex as a function of the excitation power in logarithmic scale, as shown in Fig. 4.2 (b) and 4.3 (b). It exhibits that the slopes for X and XX are respectively about 1 and 2 consistent with their number of e-h pair confined in QDs. Thus we can distinguish X signal from XX signal. Besides, the slopes for X^- and X^+ are close to 1.

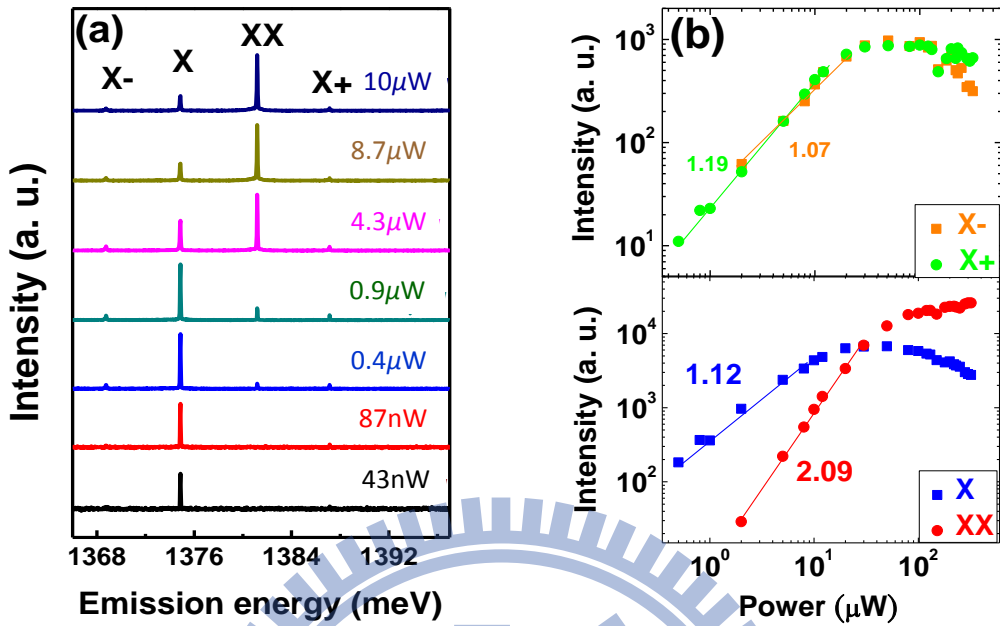


Figure 4.2: (a) The PL spectra of QD3 excited by the power from 43nW to 10μW. (b) The dependence between PL intensity and the excitation power.

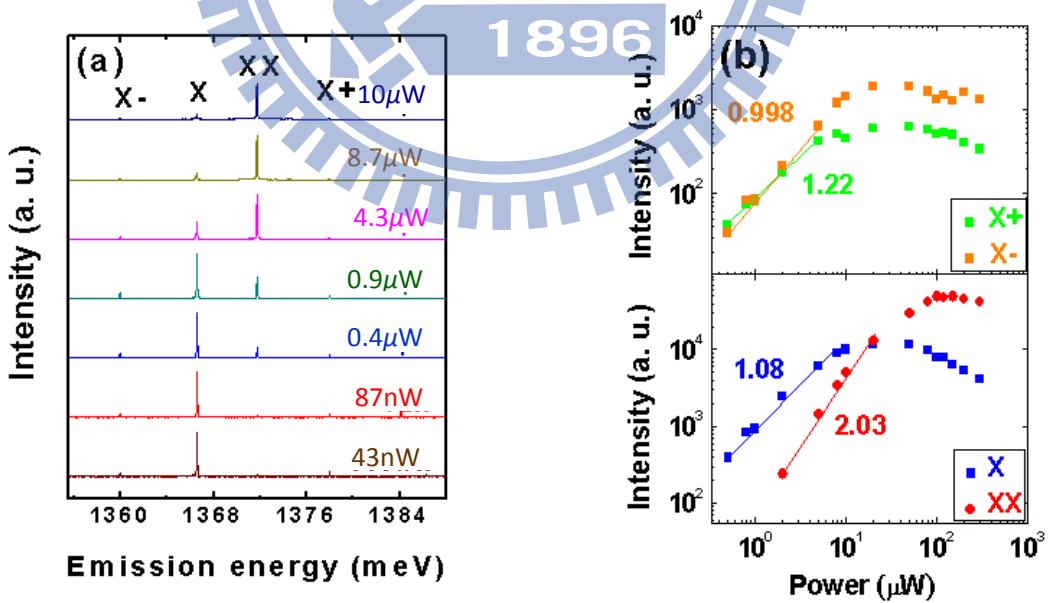
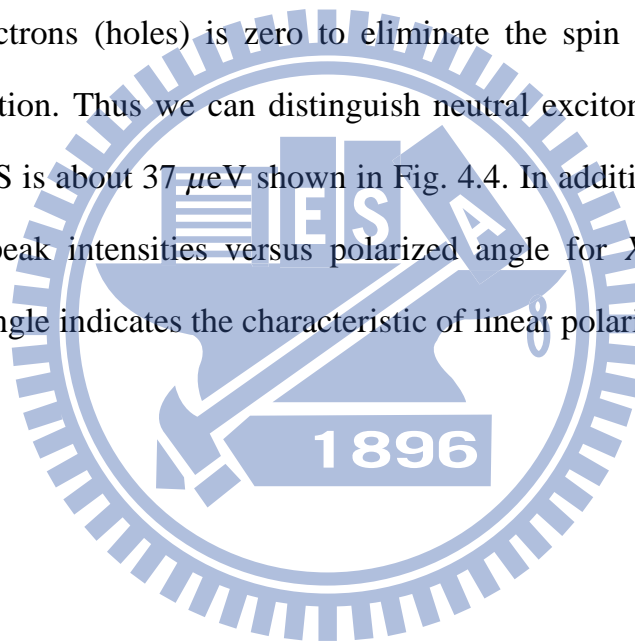


Figure 4.3: (a) The PL spectra of QD5 excited by the power from 43nW to 10μW. (b) The dependence between PL intensity and the excitation power.

4.1.2 Polarization resolution measurement

The polarizations of the four signals of each QD have been resolved by a $\lambda/2$ wave plate and a polarizer before entering the monochromator. By rotating the angle of $\lambda/2$ wave-plate, we could selectively allow the photon with specific linearly-polarized direction to pass through the polarizer. The completely angle measurement exhibits that X and XX are split by a fine structure splitting. However, the signal of X^- (X^+) is not split because the two electrons (holes) in X^- (X^+) form the singlet state, i.e., total spin of electrons (holes) is zero to eliminate the spin Hamiltonian of the e-h exchange interaction. Thus we can distinguish neutral exciton from charged exciton. For QD3, the FSS is about $37 \mu\text{eV}$ shown in Fig. 4.4. In addition, Fig. 4.5 exhibits the relation of the peak intensities versus polarized angle for X and XX , their strong dependence on angle indicates the characteristic of linear polarization.



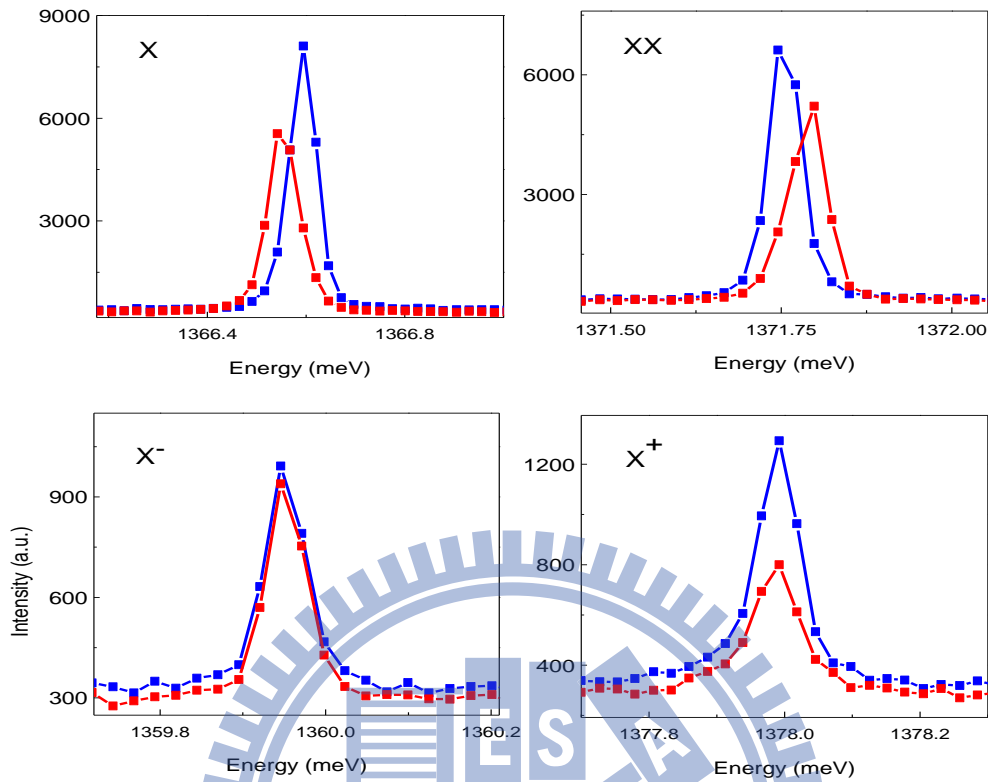


Figure 4.4: The polarized PL spectrum of X , XX , X^- and X^+ in QD3 for polarized angle 80° (blue peaks) and 160° (red peaks), respectively.

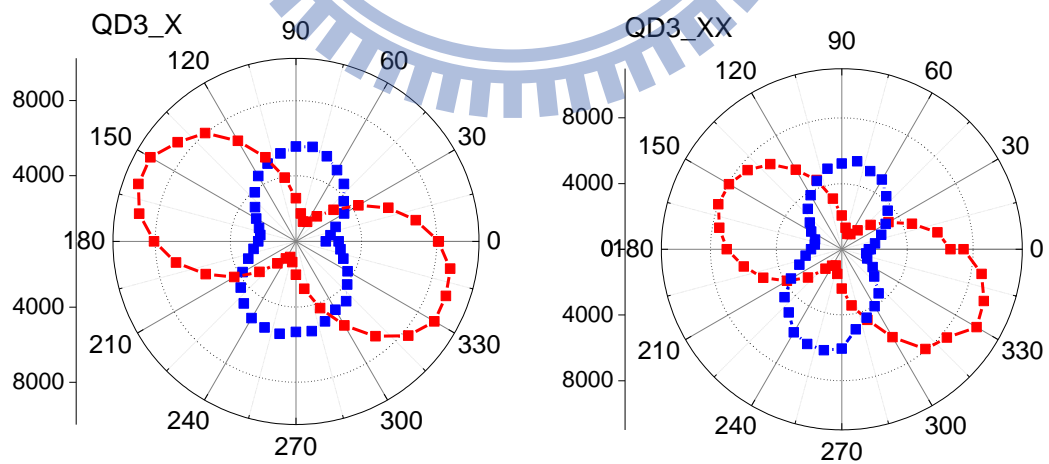


Figure 4.5: The figure of peak intensity versus polarized angle for X (left) and XX (right). The blue and red curves represent the split peaks due to FSS.

4.2 Magneto-photoluminescence results

Sequentially, the cryostat was inserted into the bore of superconducting magnet, which provided the sample for an external magnetic field along the grown direction (Faraday geometry). We executed the magneto- μ -PL measurement on the total of seven QDs mentioned in last section. Representative spectra selected from particular dot (QD1) are shown in Fig. 4.6. With increasing the magnetic field, each peak splits into the Zeeman double corresponding to two spin states, the emission energy shift are related to two mechanisms. The first one is the Zeeman spin splitting that arises from the interaction between magnetic field and spin angular momentums of carriers and increases linearly with magnetic field. Another one is the well-known diamagnetic shift that usually increases quadratically with magnetic field for neutral exciton in QD.

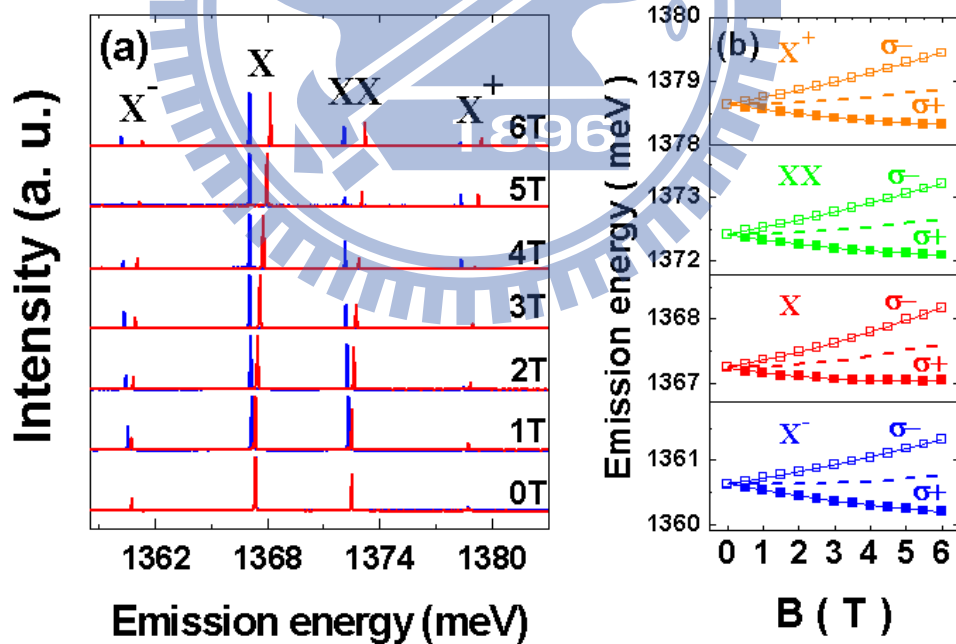


Figure 4.6: (a) The magneto-PL spectra for QD1 under a magnetic field $B=0-6$ T. (b) The corresponding peak energies of different excitonic complexes as a function of B for QD2, where σ^+ and σ^- in each form a Zeeman doublet. The dashed line is the average energy of σ^+ and σ^- .

Fig. 4.6 (b) plots the energies of two split peaks as a function of B for all excitonic complexes of QD1, which are denoted by the symbols σ^+ and σ^- . The Zeeman spin splitting and diamagnetic shift can be extracted by the energy difference $\sigma^- - \sigma^+$ and the average value of σ^+ and σ^- , as the following two relations,

$$\text{Zeeman spin splitting} = \sigma^+ - \sigma^- \quad (4.5)$$

$$\text{Diamagnetic shift} = \frac{\sigma^+ + \sigma^-}{2} \quad (4.6)$$

In Fig. 4.7 (a), the measured Zeeman spin splitting for four excitonic emission lines of four investigated QDs (QD2, QD3, QD4 and QD5) are plotted as a functions of B . Generally, the Zeeman spin splitting is expressed as Eq. 4.7,

$$\text{Zeeman splitting} = g\mu_B B \quad (4.7)$$

where μ_B is the Bohr magneton equal to $5.7883818066 \times 10^{-5}$ eV/T. The factor of g indicates the magnitude of the splitting and is determined by the material parameters of band gap, spin-orbit splitting, and so on. It can be expressed as,

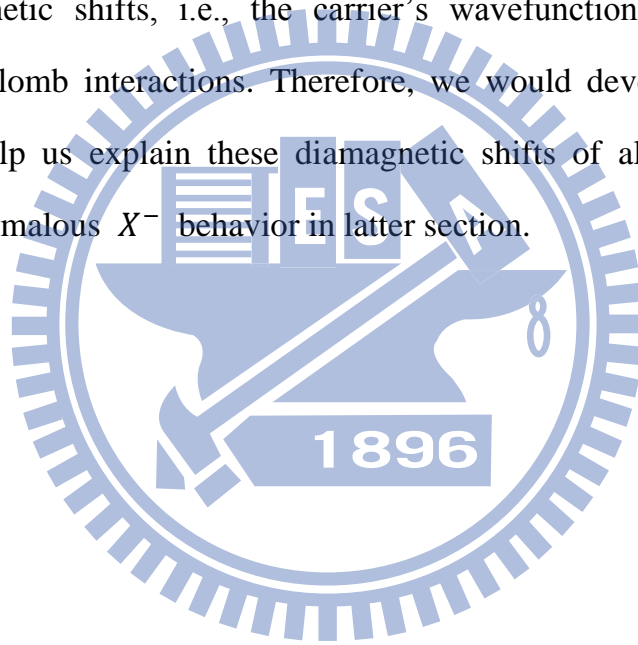
$$g = g_0 - \frac{4 m_0 P^2}{3 \hbar^2} \frac{\Delta_{so}}{E_g (E_g + \Delta_{so})} \quad (4.8)$$

where m_0 and $g_0 \approx 2$ are the free electron mass and the Lande factor, E_g is the band gap, Δ_{so} is the spin-orbit splitting of valence band, and $P = i(\hbar/m_0)\langle S|P_z|Z\rangle$ is the Kane momentum matrix element formed between the s-antibonding conduction (S) and p-bonding valence-band states (Z) [44]. Besides the material parameters, the quantum confinement of the quantum structure also acts another crucial factor for its g factor. For example, the shapes and sizes of QDs are reported to connect to the values of the g factor significantly in Ref. 45, 46, 47

We fitted the data in Fig. 4.7 (a) by the Eq. 4.7 to get their g factors. Clearly, the deduced g factors for all four excitonic emission lines (X^- , X , XX , and X^+) of the same QD are almost identical, which gives a proof that the four excitonic emission lines are indeed belong to the same QD. On the other hand, the deduced g factors for the four investigated QDs distribute over a range from 3.05 to 3.27, the slight difference in g factors maybe attributes to the variation of QD's shape and size.

In addition, we also plot the measured diamagnetic shifts for four excitonic emission lines of the four investigated QDs as a function of B^2 in Fig. 4.7 (b). Obviously, for X , XX , and X^+ in the four QDs, the measured diamagnetic shifts all display a quadratic dependence $\Delta E = \gamma B^2$, from which we can get the diamagnetic coefficient denoted γ . Actually, the quadratic dependence is still hold for other investigated QDs not shown in Fig. 4.7. In very strong contrast, the diamagnetic shift for the X^- does not always obey the quadratic dependence, and has quite large variations among individual QDs. For QD2 and QD5, the X^- diamagnetic shifts still maintain the quadratic dependence, but for QD3, that is more close to a quartic dependence. Interestingly, QD4 exhibits an unexpected-negative diamagnetic shift for X^- , i.e., a special paramagnetic behavior. However we still use a quadratic dependence to fit the anomalous X^- diamagnetic shift to get γ_{X^-} , the deduced diamagnetic coefficients for four excitonic complexes of all investigated QDs are plotted as a function of X emission energy as shown in Fig. 4.8. A clear trend of $\gamma_X > \gamma_{XX} \cong \gamma_{X^+}$ is observed for all QDs, and the diamagnetic coefficients γ_X , γ_{XX} and γ_{X^+} become larger with the raise of X emission energy. On the other hand, the diamagnetic coefficient γ_{X^-} was found to be the smallest one among the four excitonic species, and it seems not to have obvious dependence on X emission energy. The difference of diamagnetic coefficients among the four excitonic complexes can be attributed to interparticle Coulomb interactions. For this trend of $\gamma_X > \gamma_{XX} \cong \gamma_{X^+}$, M. F. Tsai *et al.*

have discuss its cause in Ref. 23. In their theory model, a 2D-disk with a parabolic-confined potential is considered, and the interparticle Coulomb energies are regarded as perturbation terms. They suggested that because of the wider lateral extent of electron than that of hole in small InAs QDs, the increasing rates of V_{ee} and V_{eh} with magnetic field are more rapid than that of V_{hh} , i.e., $\Delta V_{ee}(B) \cong \Delta V_{eh}(B) > \Delta V_{hh}(B)$, thus resulting in the trend $\gamma_X > \gamma_{XX} \cong \gamma_{X^+}$. However, the anomalous X^- diamagnetic shifts are not yet explained in Ref. 23. We think that the supposition of regarding the interparticle Coulomb energies as perturbation terms is no more suitable for X^- diamagnetic shifts, i.e., the carrier's wavefunctions would be obviously changed by Coulomb interactions. Therefore, we would develop another numerical simulation to help us explain these diamagnetic shifts of all excitonic complexes, including the anomalous X^- behavior in latter section.



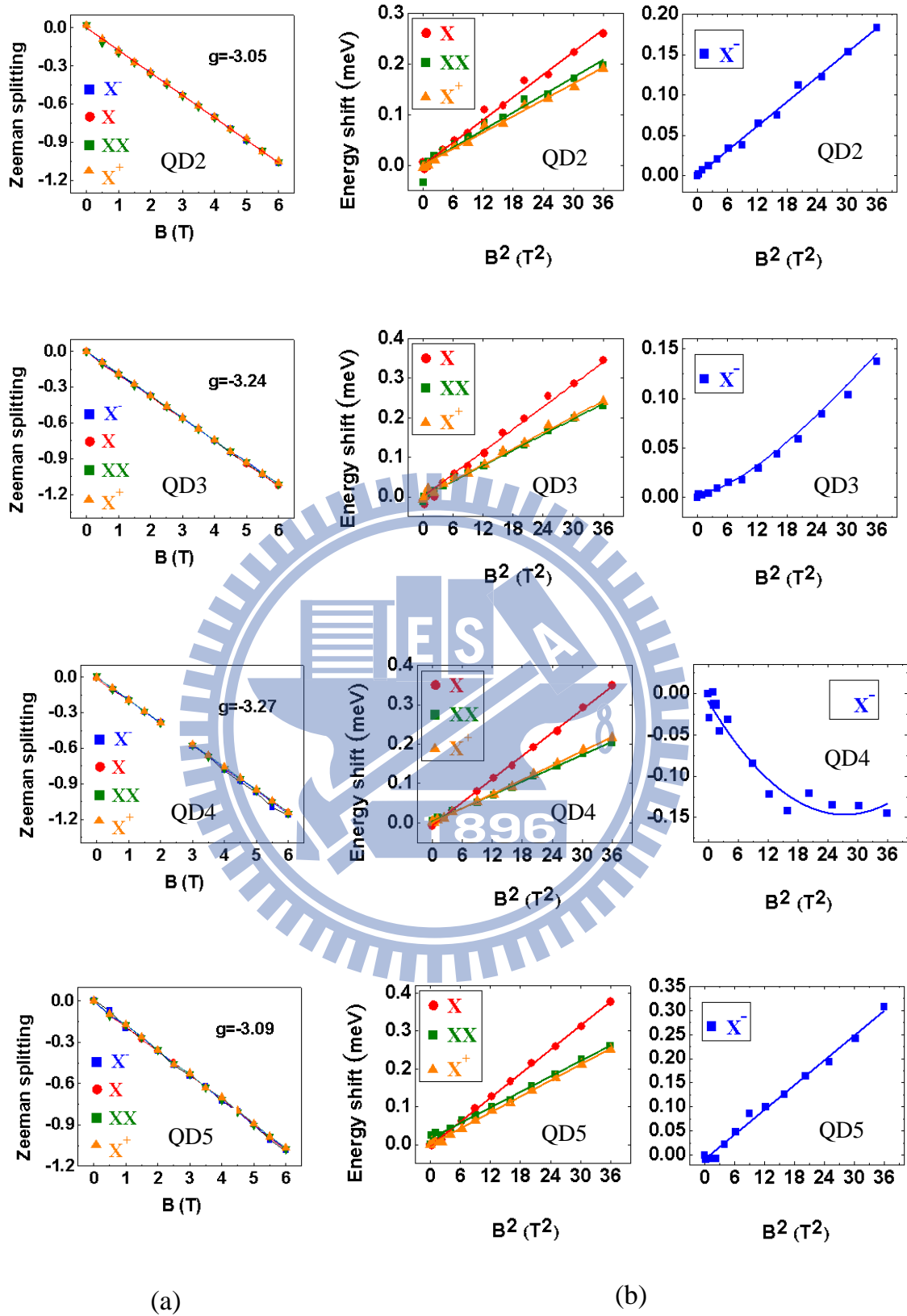


Figure 4.7: The Zeeman splitting versus B (a) and the diamagnetic shifts versus B^2 (b) for X^- , X , XX , and X^+ of four QDs (QD2, QD3, QD4, QD5). Points are the measured data, and the lines are guide for the eye.

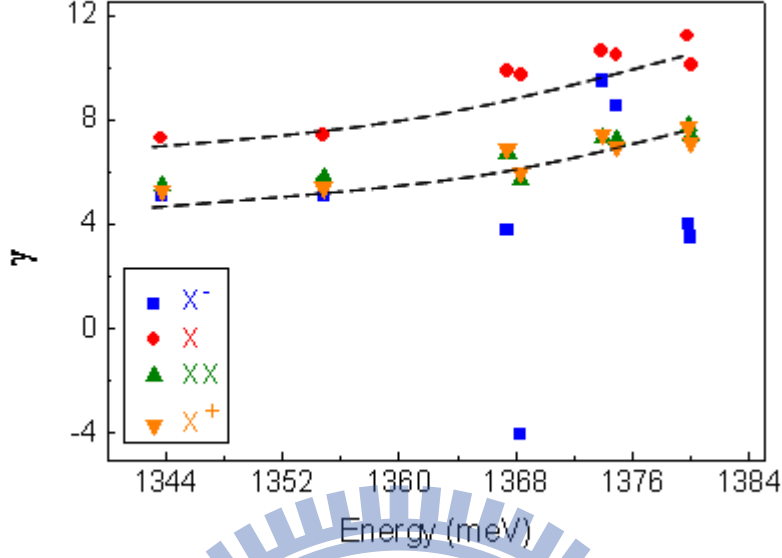


Figure 4.8: The diamagnetic coefficients γ_{X^-} , γ_X , γ_{XX} and γ_{X^+} are plotted as a function of X emission energy.

4.3 The simulation method for emission energies of excitonic complexes

To discuss the interparticle Coulomb interaction how to affect the diamagnetic behavior, we perform the numerical simulation for the quantum states of constituent carriers of excitonic complexes implemented by using the finite element method within the Hartree and one band effective mass approximation. In the Hartree and one band effective mass approximation (see Appendix B), the Schrodinger equation of a carrier in an interacting excitonic complex is written as,

$$\left[-\nabla \cdot \left(\frac{\hbar^2}{8\pi m_i^*} \nabla \phi_n^i(\vec{r}_l) \right) + V(\vec{r}_l) + V_H(\vec{r}_l) \right] \phi_n^i(\vec{r}_l) = \varepsilon_n^i \phi_n^i(\vec{r}_l) \quad (4.9)$$

where \vec{r}_i and m_i^* denote the position coordinate and the effective mass of the i th particle, V the confined potential, ε_n^i the eigenenergy, $\phi_n^i(\vec{r}_i)$ the particle wave function of the eigenstate $|n\rangle$, and $V_H(\vec{r}_i)$ is the Hartree potential (a sum of the electrostatic potentials induced by other charged particles besides the considered particle itself). In the calculation, cone-shaped QDs setting on a 0.4 nm-thick wetting layer are considered. Due to the symmetry of geometry, the eigenfunction $\phi^i(\vec{r}_i)$ can be separated into Eq. 4.10 in cylindrical coordinate,

$$\phi^i(\vec{r}_i) = \chi^i(z_i, r_i)\Theta^i(\varphi_i) \quad (4.10)$$

putting Eq. 4.10 to Eq. 4.9, Eq. (4.9) is rewritten as,

$$-\frac{\hbar^2}{8\pi} \left(\frac{\partial}{\partial z_i} \left(\frac{1}{m_i^*} \frac{\partial \chi^i}{\partial z_i} \right) + \frac{1}{r_i} \frac{\partial}{\partial r_i} \left(\frac{r_i}{m_i^*} \frac{\partial \chi^i}{\partial r_i} \right) \right) \Theta^i - \frac{\hbar^2}{8\pi m_i^* r_i^2} \frac{d^2 \Theta^i}{d\varphi_i^2} + (V + V_H) \chi^i \Theta^i = \varepsilon^i \chi^i \Theta^i \quad (4.11)$$

Dividing the Eq. 4.11 by $\frac{\chi^i(z_i, r_i)}{m_i^* r_i^2} \Theta^i(\varphi_i)$, and rearranging the terms. We can get two independent equations,

$$\frac{1}{\Theta^i} \frac{d^2 \Theta^i}{d\varphi_i^2} = -l^2 \quad (4.12)$$

$$-\frac{m_i^* r_i^2 \hbar^2}{8\pi^2} \left[\frac{\partial}{\partial z_i} \left(\frac{1}{m_i^*} \frac{\partial \chi_i^i}{\partial z_i} \right) \frac{1}{\chi_i^i} + \frac{1}{r_i} \frac{\partial}{\partial r_i} \left(\frac{r_i}{m_i^*} \frac{\partial \chi_i^i}{\partial r_i} \right) \frac{1}{\chi_i^i} \right] + m_i^* r_i^2 [V + V_H - \varepsilon^i] = \frac{-\hbar^2}{8\pi} l^2 \quad (4.13)$$

l is the quantum number of the angular momentum, and

$$\Theta^i = \exp[-il\phi] \quad (4.14)$$

Eq. 4.13 can be rewritten as,

$$-\frac{\hbar^2}{8\pi^2} \left[\frac{\partial}{\partial z_i} \left(\frac{1}{m_i^*} \frac{\partial \chi_i^i}{\partial z_i} \right) + \frac{1}{r_i} \frac{\partial}{\partial r_i} \left(\frac{r_i}{m_i^*} \frac{\partial \chi_i^i}{\partial r_i} \right) \right] + \left[\frac{\hbar^2}{8\pi^2 m_i^* r_i^2} l^2 + V + V_H \right] \chi_i^i = \varepsilon_i^i \chi_i^i \quad (4.15)$$

It is simplified to a two-dimension partial differential problem. Here we only considered the ground state with $l = 0$ because of the electronic configurations for all considered excitonic complexes. This partial differential equation was solved by using the finite element method that is packaged in a commercial software (Cosmol Multiphysics).

First we selected the 2D-PDE function (coefficients form) of Comsol to calculate the quantum levels ε_0 and the wave functions χ_0 of all (noninteraction) particles, and then the volume carrier density $\rho(z_i, r_i)$ gotten from the wave functions of all particles, excluding the objective *ith*-particle, was brought into Poisson equation to calculate the Hartree potential $V_H(z_i, r_i)$ for the considered *ith*-particle by using the 2D-Electrostatics function of Comsol as Eq. 4.16.

$$-\left[\frac{\partial}{\partial z_i} \left(\varepsilon_0 \varepsilon_r \frac{\partial}{\partial z_i} V_H(z_i, r_i) \right) + \frac{1}{r_i} \frac{\partial}{\partial r_i} \left(\varepsilon_0 \varepsilon_r r_i \frac{\partial}{\partial r_i} V_H(z_i, r_i) \right) \right] = \rho(z_i, r_i) \quad (4.16)$$

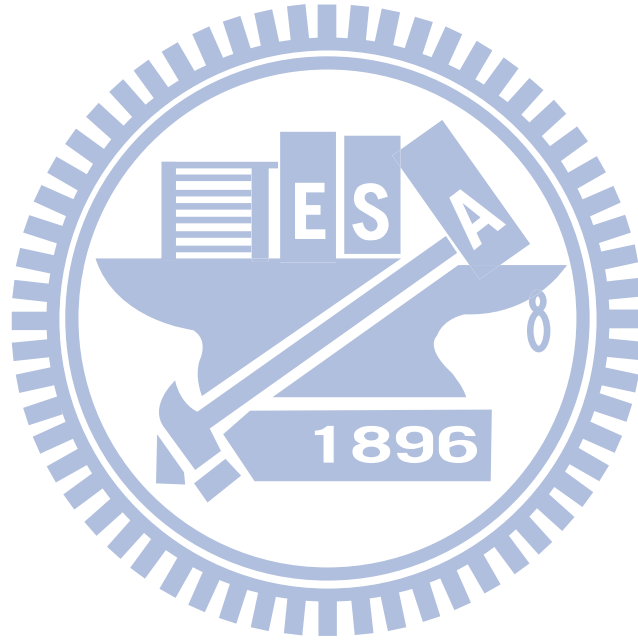
Again, we solved the PDE of the considered *ith*-particle by introducing its Hartree potential into Eq. 4.15. A new energy level and wave function of the *ith*-particle was obtained, moreover, its produced carrier density again affected the wave functions of other particles. By a series of iterative process, we can get a self-consistent and convergent solution for $\{\varepsilon_0^i\}$. For an N-particle excitonic complex, the N-coupled equations of Eq. 4.15 are necessarily to be self-consistently solved by above iterative method. The steps of self-consistent calculation is shown in Fig. 4.9. The total emission energy of the N-particle excitonic complex is then determined by the sum of single-particle energy $\{\varepsilon_0^i\}$, added by InAs energy gap (E_p), but subtracted by the doubly counted interparticle interaction energies (V_{ee}, V_{eh}, V_{hh}) in this iterative process. Thus the emission energies for all excitonic complexes are given,

$$E_{X^-} = (2\varepsilon^e + \varepsilon^h + 2V_{eh} - V_{ee})_{interaction} - (\varepsilon^e)_{noninteraction} + E_g \quad (4.17)$$

$$E_X = (\varepsilon^e + \varepsilon^h + V_{eh})_{interaction} + E_g \quad (4.18)$$

$$E_{XX} = (2\varepsilon^e + 2\varepsilon^h - V_{ee} - V_{hh} + 4V_{eh})_{interaction} - X + 2E_g \quad (4.19)$$

$$E_{X^+} = (\varepsilon^e + 2\varepsilon^h + 2V_{eh} - V_{hh})_{interaction} - (\varepsilon^h)_{noninteraction} + E_g \quad (4.20)$$



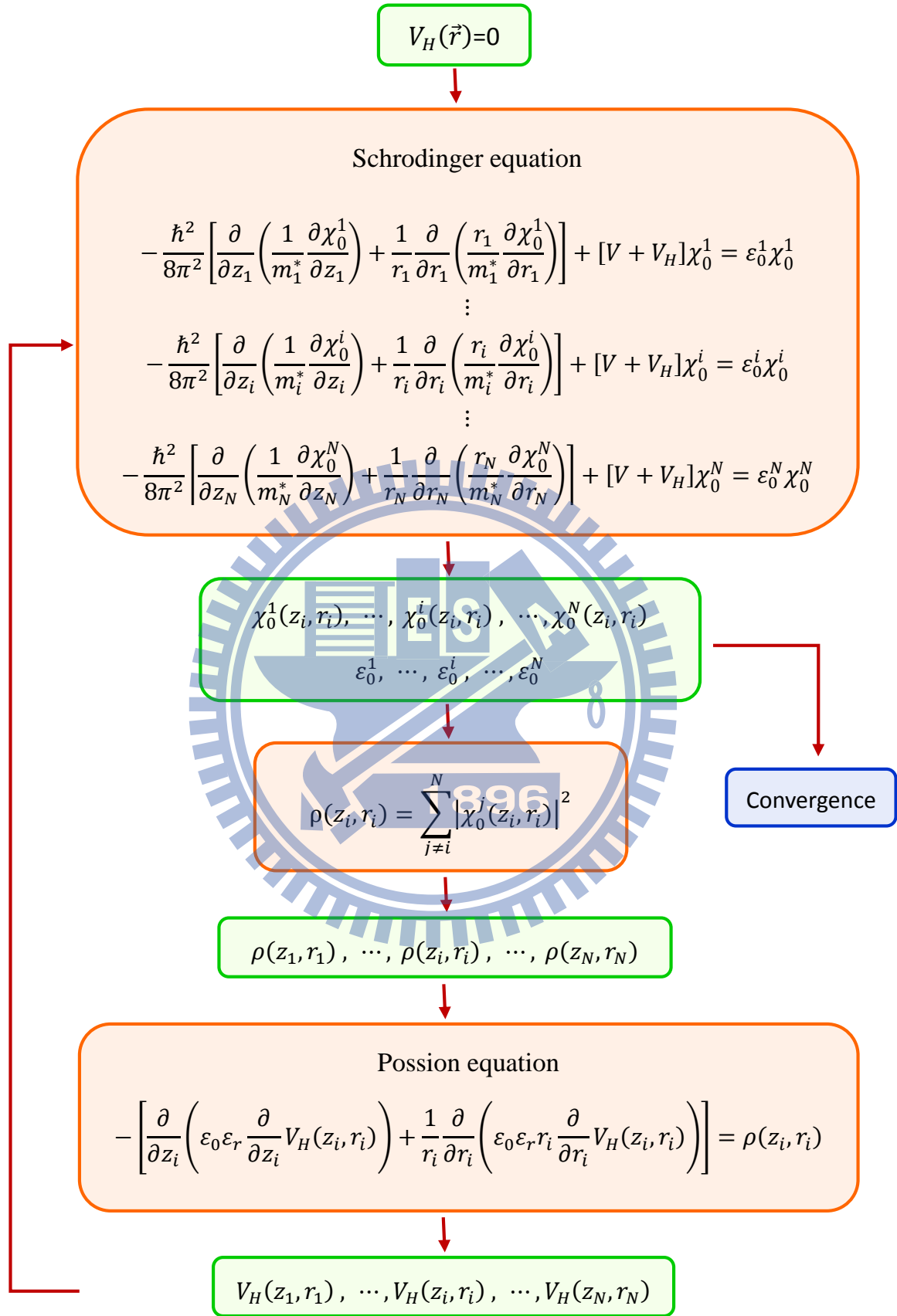


Figure 4.9: The steps of self-consistent calculation.

4.4 The simulation results of diamagnetic shifts and their size-dependence

We used the above method to calculate the emission energies of excitonic complexes for cone-shape InAs QDs sitting on a 0.4 nm-thick wetting layer when an external magnetic field B along vertical direction is considered in this calculation. Fig. 4.10 depicts the cross-sectional view, of which the height and diameter are denoted h and w , respectively. The used material parameters (the effective mass, dielectric constant, band offset and band gap) with the consideration of strain effect are taken from Ref. [48] and listed in Table 4.1. The InAs/GaAs QD is a typical Type II heterstructure, its band diagram of heterinterface is shown in Fig. 4.11. We reasonably select three investigated QDs (QD3, QD1, and QD4) to fit their experimental results by this calculation because their X^- diamagnetic shifts both include the cases of quadratic dependence and anomalous behavior. For comparing, the experimental and simulated results of emission energies of the four different excitonic complexes are both plotted as a function of B^2 in Fig. 4.12, of which the external magnetic field is given from 0T to 6T. The simulated size parameters are diameter of 11.6 nm and height of 1.1 nm for QD3; diameter of 11 nm and height of 1.4 nm for QD1; diameter of 8.4 nm and height of 1.4 nm for QD4. Besides, the simulated diamagnetic coefficients are obtained by taking the second derivative of simulated magnetoenergy spectra with respect to B using three-point numerical differentiation and shown in Fig. 4.13. Compare with the experimental and simulated results, the diamagnetic shifts and diamagnetic coefficients of them are both consistent with each other very well for all excitonic complexes. For X^- diamagnetic shifts, we can see whether the quadratic-dependence or the anomalous behavior all can be gotten in our calculation by tuning the QD's size, which indicates that the anomalous X^- diamagnetic shifts

have very strong dependence on the size factor of QDs.

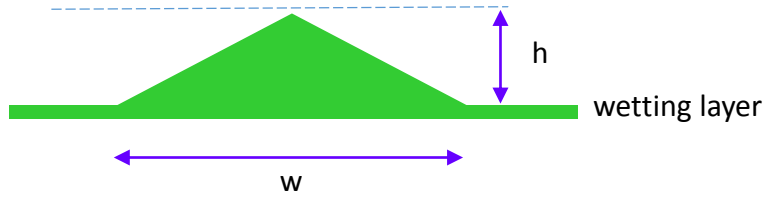


Figure 4.10: The cross-section of simulated cone-shaped InAs QD, of which the height and diameter are denote h and w.

	m_e^*	m_h^*	ΔE_c	ΔE_v	E_g
InAs	$0.044m_0$	$0.5m_0$	0.419eV	0.258eV	0.842eV
GaAs	$0.067m_0$	$0.5m_0$			1.519eV

Table 4.1: The used material parameters in the simulation.

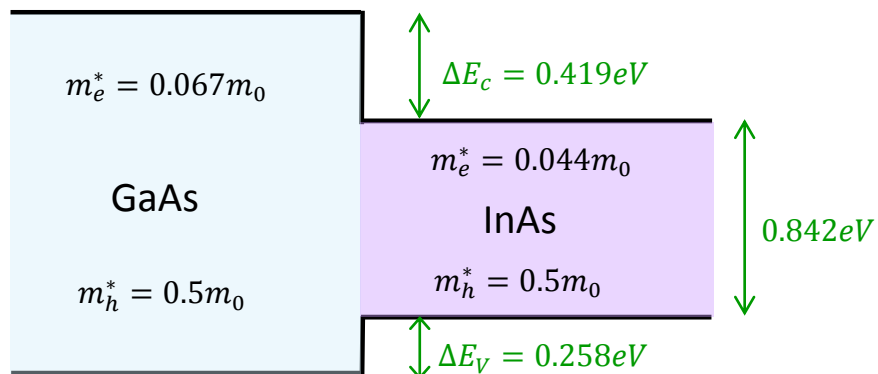


Figure 4.11: The band diagram of InAs/GaAs interface in QDs.

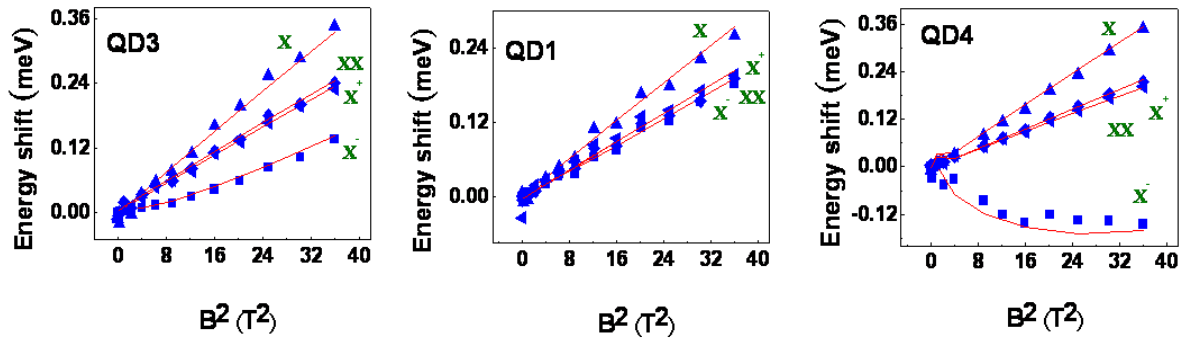


Figure 4.12: The diamagnetic shifts of the excitonic complexes for the three typical QDs (QD3, QD1 and QD4). Blue points and red lines are the experimental and simulated results, respectively. The simulated parameters are diameter of 11.6 nm and height of 1.1 nm for QD3; diameter of 11 nm and height of 1.4 nm for QD1; diameter of 8.4 nm and height of 1.4 nm for QD4.

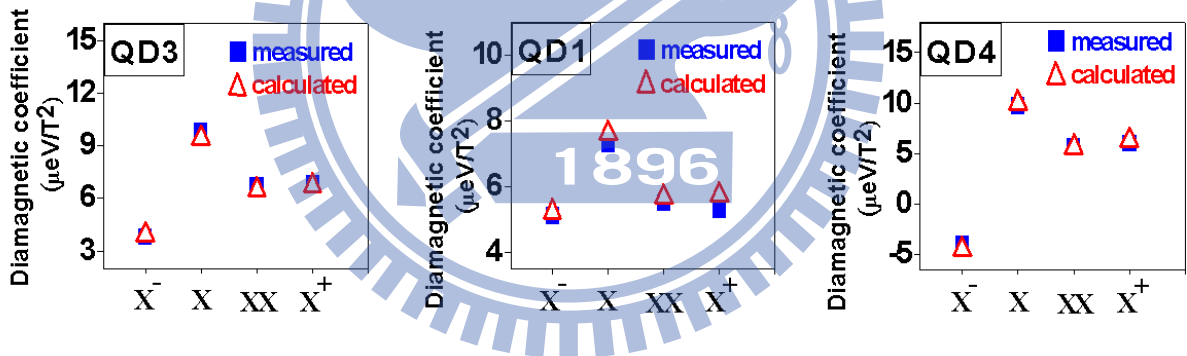


Figure 4.13: The experimental and simulated diamagnetic coefficients of the excitonic complexes for the three typical QDs (QD3, QD1 and QD4). The simulated parameters are diameter of 11.6 nm and height of 1.1 nm (QD3); diameter of 11 nm and height of 1.4 nm (QD1); diameter of 8.4 nm and height of 1.4 nm (QD4).

Continuatively, we discuss the QD's size effect on the diamagnetic shifts. The calculated diamagnetic coefficients for the four exciton complexes in QDs with a diameter ranging from 12 to 26 nm are shown in Fig. 4.14 (a). For large-sized QDs ($D > 16$ nm), the diamagnetic coefficients of the four exciton complexes show similar

increasing trends with the QD size. Because the diamagnetic coefficient is proportional to the area of the carrier's wave function, which associates with the dot diameter for large-size QDs [35, 49]. However, for smaller QD sizes ($D < 16$ nm), the calculated values of γ_X increase with the decreasing dot size, while that of γ_{XX} and γ_{X^+} remain nearly unchanged. The most striking feature is that the calculated γ_{X^-} drops rapidly with the decreasing dot size. Here one can note that our self-consistent calculations also reproduce the experimental finding of $\gamma_X > \gamma_{XX} \cong \gamma_{X^+}$ very well.

For the emission of negative trion X^- , the initial state consists of two electrons and one hole leaving one electron in its final state after recombination. Thus the X^- diamagnetic shift is dominated by the diamagnetic responses of both the initial and final states. To understand the anomalous behavior for X^- , it is necessary to take a closer look at the lateral extent $\ell_e = \sqrt{\langle \rho_e^2 \rangle}$ of the electron wave functions before and after photon emission. Fig. 4.14 (b) shows the calculated wave function extents $\ell_{e,i}$ and $\ell_{e,f}$ for the initial-state and the final-state electrons of X^- , respectively. One can see that the $\ell_{e,f}$ is always more or less larger than $\ell_{e,i}$. This can be realized from the presence of the hole in its initial state, which contracts the electron wave function by the Coulomb attraction. When the sizes of QDs are larger than about 16 nm, the differences between $\ell_{e,i}$ and $\ell_{e,f}$ are small; i.e., the presence of the hole does not change the electron wave function significantly. However, as the QD sizes reduces, $\ell_{e,f}$ increases rapidly, with a rate even faster than $\ell_{e,i}$. Such an increasing trend for $\ell_{e,f}$ indicates that the electron gradually loses confinement as the dot size reduces, which pushes the electron level toward the wetting-layer continuum, resulting in a very extended electron wave function penetrating into the barrier material, as be clearly seen in Fig. 4.15, which plots the distribution of calculated carrier wave function. In such a case of weak confinement regimes, the very extended initial-state

electron becomes sensitive to the long-range Coulomb attractive potential produced by the hole, by which $\ell_{e,i}$ will be contracted and become apparently smaller than $\ell_{e,f}$. As a result, the final-state diamagnetic shift increases, so that the overall diamagnetic shift in X^- is reduced. This explains why the X^- diamagnetic shift decreases rapidly for small-sized QDs shown in Fig. 4.14 (a). Likewise, for the emission of positive trion X^+ , the initial state consists of one electron and two holes leaving one hole in its final state after recombination. As shown in Fig. 4.14 (b), unlike X^- , the lateral extents of hole wave functions $\ell_h = \sqrt{\langle \rho_h^2 \rangle}$ in the initial and final states are almost identical for all QD sizes. Due to the larger effective mass of holes, their wave functions are well confined even in such small QDs. In this case, the Coulomb attractive potential produced by the weakly confined electron becomes less important, so that the size dependence of γ_{X^+} behaves as usual. Comparing the experimental results in Fig. 4.8 with calculated results in Fig. 4.14, The increased trend of the calculated γ_X , γ_{XX} , and γ_{X^+} with reducing the dot diameter (when $D < 16$ nm) is consistent with the experimental results because the small QDs have higher X emission energy than that of large QDs. Besides, we also review the relation between the X^- diamagnetic coefficients and X emission energy, and found the measured γ_{X^-} has a decreased trend with increasing the X emission energy for most dots, except for the three points in the circles, as shown in Fig. 4.16. We think the deviation of three dots inside the circles is attributed to the height variation among dots, which can influence the quantum levels seriously.

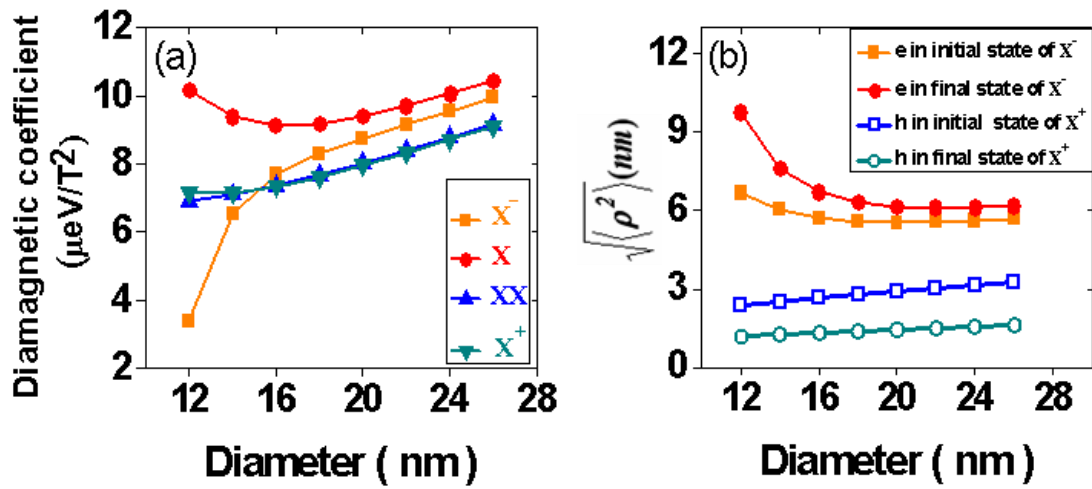


Figure 4.14: The simulation for QDs with various diameters, the diamagnetic coefficients (a), and the root mean square radius of electron and hole wave functions in their initial and final states (b).

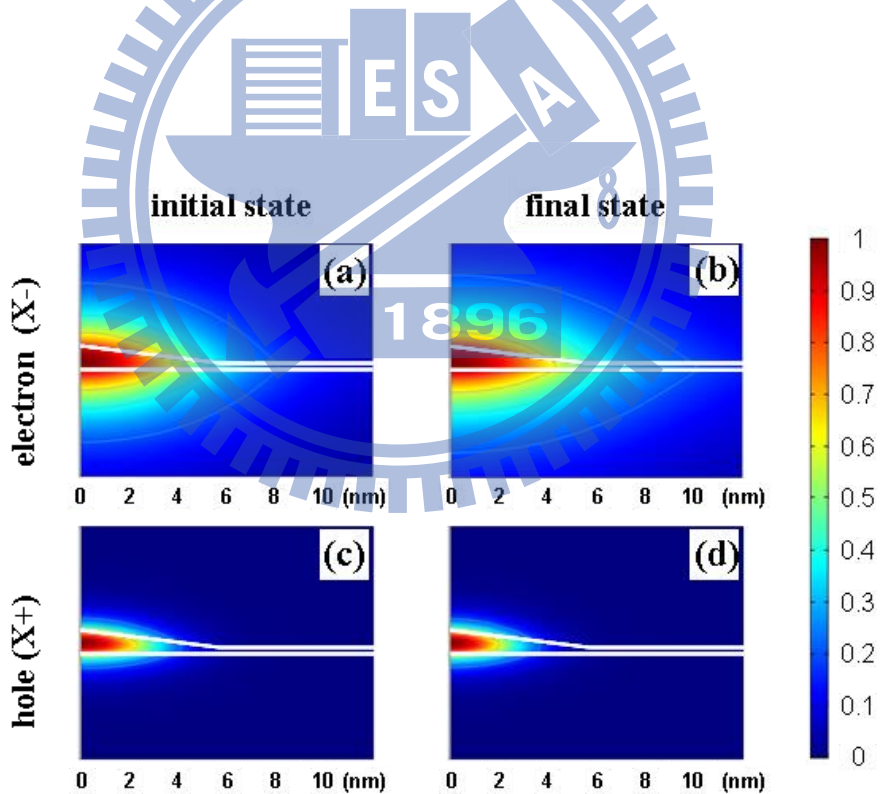


Figure 4.15: The distribution of calculated electron wave function in X^- initial state (a), and X^- final state (b); The distribution of calculated hole wave function in X^+ initial state (c), and X^+ final state (d). White line: the QD's boundary with diameter of 11.6nm and height of 1.1nm.

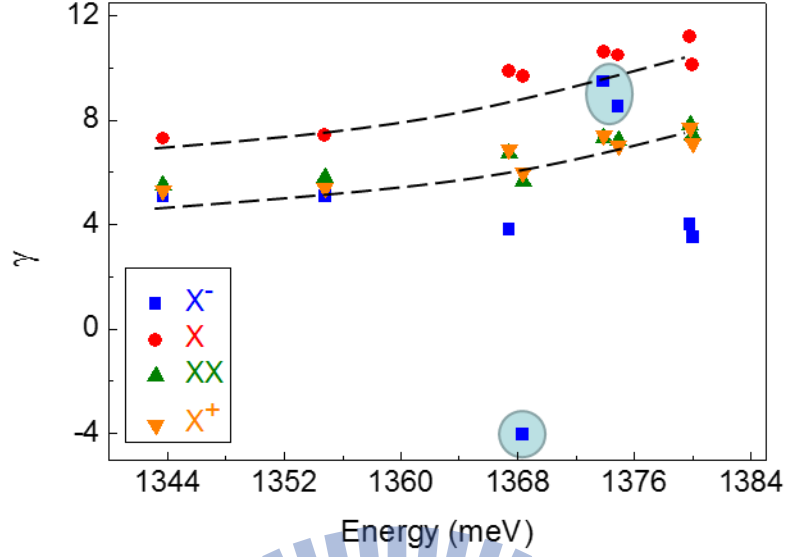


Figure 4.16: The diamagnetic coefficients γ_{X^-} , γ_X , γ_{XX} and γ_{X^+} are plotted as a function of X emission energy. The dashed lines are guide for the eye.

4.5 Brief discussion of anomalous diamagnetic shift

Now one may ask the question why the X^- diamagnetic shift exhibits a nonquadratic B dependence. In general, a quadratic diamagnetic shift holds only in the weak-field limit, i.e., when the magnetic length $\ell_M = \sqrt{\hbar/eB}$ is large compared to the lateral extents of the carrier's wave functions $\ell = \sqrt{\langle \rho^2 \rangle}$. We noted that $\ell_M = 15$ nm at $B=3$ T, which becomes comparable with $\ell_{e,f} = 10$ nm for the final-state electron in a QD with a base diameter of 12 nm. In this regime, the diamagnetic shift would deviate from the typical B^2 dependence. To illustrate this behavior, we consider the diamagnetic shift in the carrier's single-particle energy and expand it in powers of B as $\Delta\varepsilon_\alpha^{SP}(B) = \gamma_\alpha B^2 + \kappa_\alpha B^4 + \dots$, which has been mentioned in Eq. 2.21, where the quadratic and quartic coefficients are $\gamma_\alpha = e^2 \ell_\alpha^2 / 8m_\alpha$ and $\kappa_\alpha =$

$-e^4 \ell_\alpha^6 / 128 m_\alpha \hbar^2$, in which $\alpha = e$ or h denotes the electron or hole, and m_α represents the effective mass of the electron or hole. Because $|\kappa/\gamma|$ varies as $\sim \ell^4$, the contribution from the B^4 term becomes increasingly important as $\ell \sim \ell_M$. By taking into account the difference between $\ell_{e,i}$ and $\ell_{e,f}$, a simple algebraic analysis for the X^- diamagnetic shift $\Delta E_{X^-}(B)$ gives the following expression:

$$\Delta E_{X^-}(B) \approx \gamma_{X^-} B^2 + \kappa_{X^-} B^4 + \dots, \quad (4.21)$$

where $\gamma_{X^-} = (2\gamma_{e,i} + \gamma_{h,i}) - \gamma_{e,f}$ and $\kappa_{X^-} = (2\kappa_{e,i} + \kappa_{h,i}) - \kappa_{e,f}$. Because of $\ell_h < \ell_e$ and $m_h \gg m_e$, the $\gamma_{h,i}$ and $\kappa_{h,i}$ for the hole only have minor influences on the overall diamagnetism. Accordingly, we obtain $\gamma_{X^-} \approx e^2(2\ell_{e,i}^2 - \ell_{e,f}^2)/8m_e$ and $\kappa_{X^-} \approx e^4(2\ell_{e,i}^6 - \ell_{e,f}^6)/128m_e\hbar^2$. Equation 4.21 makes clear how the difference in $\ell_{e,i}$ and $\ell_{e,f}$ can lead to anomalous diamagnetic behaviors for the emission energy of X^- . We first consider a normal case of $\ell_{e,i} = \ell_{e,f} = \ell_e$; we have $\gamma_{X^-} \approx \gamma_e \approx \gamma_X$ and $\gamma_{X^-} \gg \kappa_{X^-}$, as long as $\ell_e < \ell_M$. That is, the X^- diamagnetic shift behaves as the usual quadratic dependence with a coefficient similar to that of X , which is just the case for large-size QDs shown in Fig. 4.14 (a). A very interesting case occurs when $\sqrt{2}\ell_{e,i} = \ell_{e,f}$; i.e., $\ell_{e,i}$ of the initial-state electrons were contracted to 70.7% of its final-state extension $\ell_{e,f}$ by the hole. In this special case, the condition $2\gamma_{e,i} = \gamma_{e,f}$ cancels out the B^2 term leading to a dominant quartic dependence on B . As the difference between $\ell_{e,i}$ and $\ell_{e,f}$ becomes even larger ($\sqrt{2}\ell_{e,i} < \ell_{e,f}$), the magnetic response of X^- goes into a new regime where the quadratic coefficient γ_{X^-} is negative; i.e., the energy shift is *paramagnetic*. This anomalous behavior can be best seen from the calculated results shown in Fig. 4.17 (a), where we keep $\ell_{e,f} = 10$ nm but varying $\ell_{e,i}$ from 7.6 to 6.6 nm. The magnetic response of X^- emissions

transited gradually from the usual quadratic diamagnetic shift to quartic dependences, and finally into an overall negative energy shift, resembling paramagnetic behaviors. In Fig. 4.17 (b), we can see four typical QDs, that could represent the X^- diamagnetic behaviors in different regimes, in qualitative agreement with our calculations.

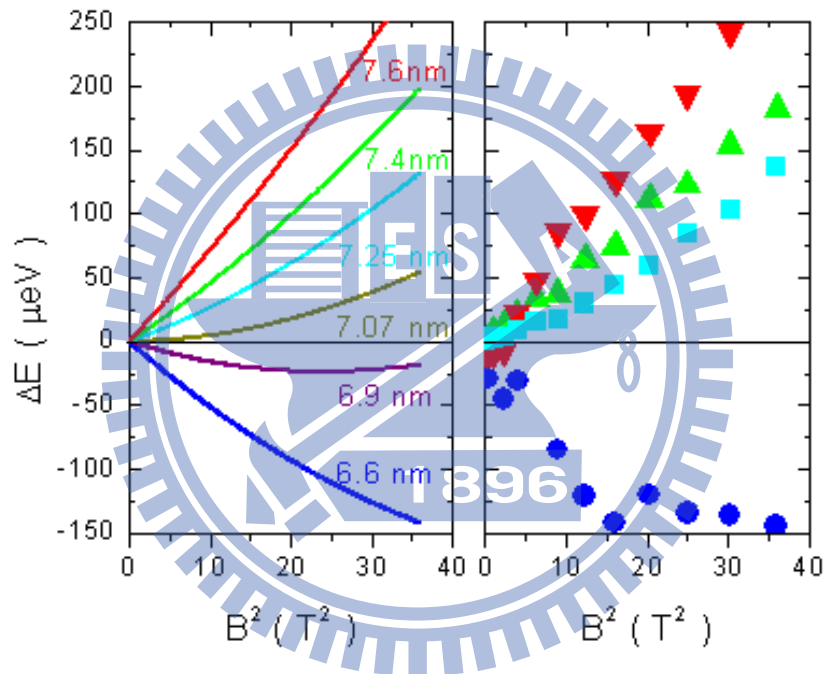


Figure 4.17: The theoretical (left) and experimental (right) anomalous diamagnetic shifts in small QDs.

Chapter 5 Design of high quality-factor H1-cavities in 2-D photonic crystal and demonstration of their strong coupling to single InAs quantum dot

In this Chapter, we propose a method for designing H1 photonic crystal cavity to enhance its Q factor while the mode volume is nearly unchanged. The simulations of Q factor and mode volume are executed by using the 3D finite-difference time-domain (FDTD) packed in a commercial soft (Rsoft, fullwave), and the experimental results are collected by the same micro-PL system. The Q-factor enhancement is explained with the analysis of the Fourier transformation of electric field distribution in cavity. Finally, we successfully observe the strong coupling effect between cavity and single QD.

5.1 The designed structure of modified H1 cavity

The H1 PhC cavity is a 2D membrane suspended in air, with the triangular lattice of air holes lacking one of them to form a cavity. The tilt-view and top-view of this structures can be clearly seen in Fig. 5.1. In this dissertation, we used a GaAs layer with InAs QDs as the membrane material in order to study the coupling effect between QDs and cavity. Because the refractive index of GaAs is larger than that of air, the light of resonant mode would be confined within the membrane and the cavity. However, H1 cavity usually has smaller Q factor and mode volume. In order to enhance the coupling strength to QDs, improving its Q factor as maintaining small volume is necessary to be achieved.

To enhance the Q factor of an H1 cavity, a common method is modifying the positions and radii of holes near the defect cavity [17, 50–52]. So far, the highest Q

factor obtained in experiment is about 25,000 by modifying more holes around the cavity, but the design principle and underlying physics have not been detailed [50].

Here we propose an alternative method for enhancing the Q factor of an H1 cavity while the mode volume is nearly unchanged. Figure 5.2 shows our design of the H1 cavity based on triangular lattice of air holes, the centered hole is absent leaving a defect as an optical cavity, and the period and radii of air holes are a and r , respectively. Starting with the common design, the six nearest neighbor holes around the cavity are shifted in radial direction and away from the defect a distance denoted as s here. The radii of the six holes are reduced from r to r' [51]. In addition, in our design, one more modification on other air holes is introduced to enhance its Q factor further. We reduce the radii of the fourth, fifth, eighth, and ninth rounds of air holes, as indicated with gray regions I and II in Fig. 5.2, from r to r'' .

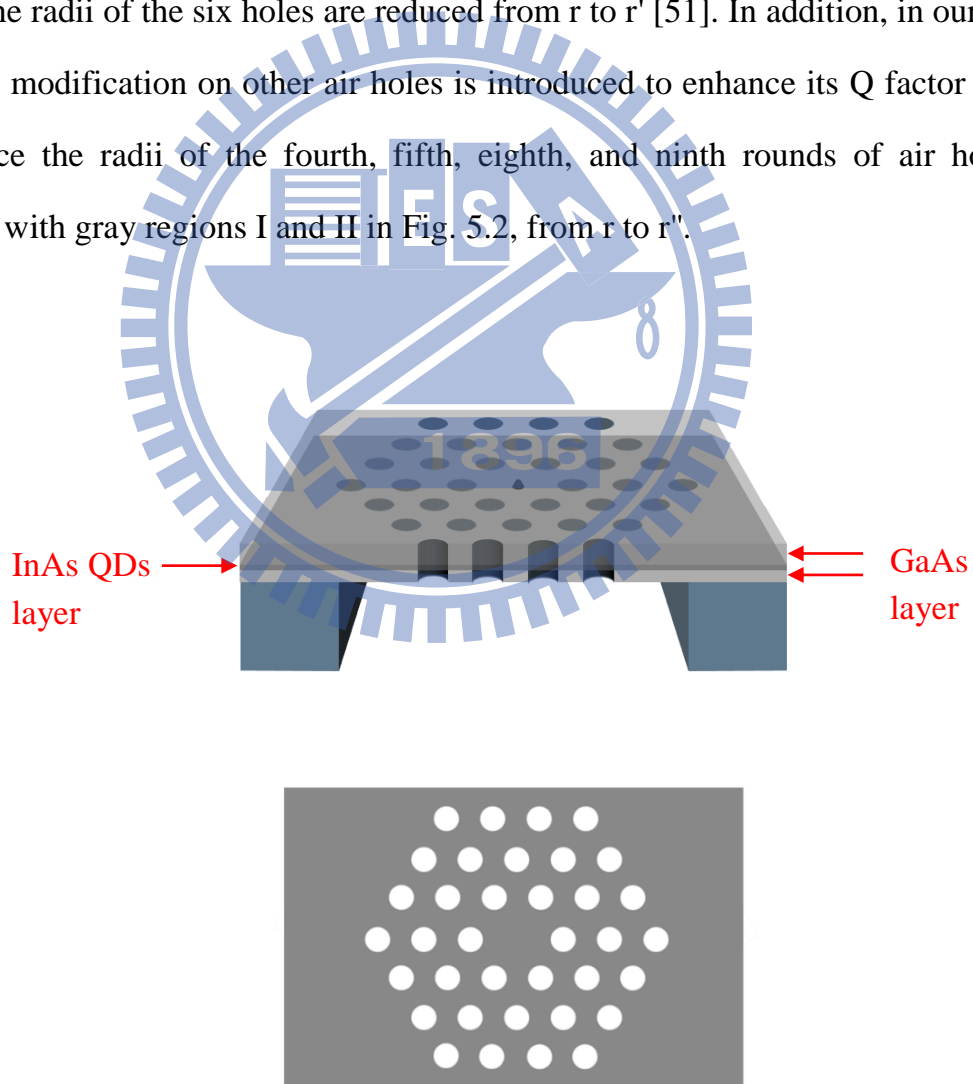


Figure 5.1: The tilt-view and top-view of H1 PhC cavity.

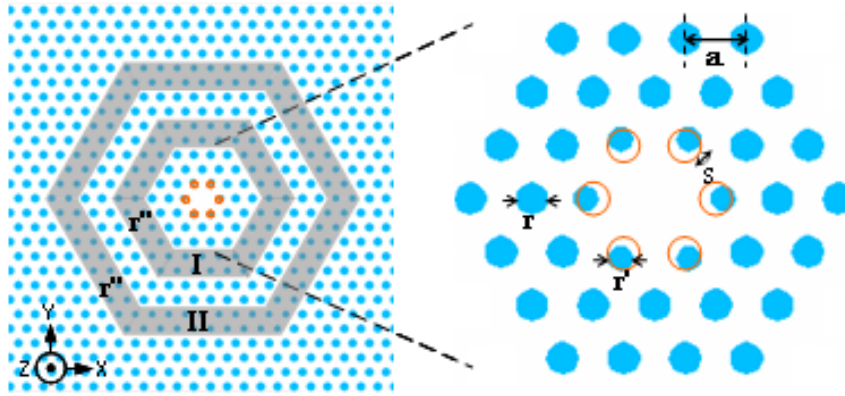


Figure 5.2: Schematic modified H1 cavity. The lattice constant is a . The radius of regular air hole is r . The nearest six air holes around defect are shifted and their radii are reduced to r' , as illustrated in the enlarged figure on the right. The radii of air holes inside regions I and II are reduced to r'' .

5.2 The simulation results of Q factor and mode volume

To simulate the modified H1 cavity, we use 3-D finite-difference time-domain (FDTD) method that is packaged in a commercial software (Rsoft, FullWave). The simulated parameters are detailed as follows. The thickness of GaAs photonic crystal membrane, denoted as d , is 130 nm. The lattice constant a is 260 nm and the radius of air hole r is $0.25a$. The shifted distance s of the nearest six holes is $0.12a$. We use constant refractive index of 3.36 for GaAs. The values of r' and r'' are varied in our simulation to see their effects on the Q factor. The Q value and mode volume are obtained with the method of fast harmonic analysis. We would like to note that the validity of simulation has been verified by calculating the H1 cavity case reported in [50] as they obtained the highest Q factor of about 60,000 previously. By using our simulation tool and their parameters, our theoretical Q factor is considerably consistent with theirs as shown Fig. 5.3.

The calculated Q factors for the modified H1 cavity and the corresponding mode

volumes are shown in Fig. 5.4. In Fig. 5.4 (a), the Q factors of V-dipole cavity mode for r''/r ratios from 0.6 to 1 are plotted. Each curve represents different r' from 0.154a to 0.231a. We can see an evident trend that, with reducing r''/r ratio, the Q factor raises and reaches its maximum around $r''/r = 0.65-0.75$. However, it falls rapidly when the r''/r ratio comes to about 0.6. The strongest dependence is obtained with $r' = 0.192a$. The Q factor for an unmodified H1 cavity ($r''/r = 1$) is about 33,000 and reaches the highest value about 120,000 for the modified one of $r''/r = 0.7$. A four-fold Q-factor enhancement has been achieved. However, for other r' , this enhancement becomes less significant. On the other hand, the corresponding mode volumes V are plotted in Fig. 5.4(b). With decreasing r''/r ratios, the mode volumes V increases monotonically for all r' . Nevertheless, the increased amount is all less than 14% so the parameter Q/V , which governs the coupling strength between cavity and emitter, could be increased. In addition, we would like to note that based on the simulated results, the parameters r' , s , and r'' are rather critical to obtain a high Q factor of modified H1 cavity. With appropriate r' and s , a well-tuned r'' could give us an extremely high Q factor. This, of course, would be a challenging task for fabricating the real devices.

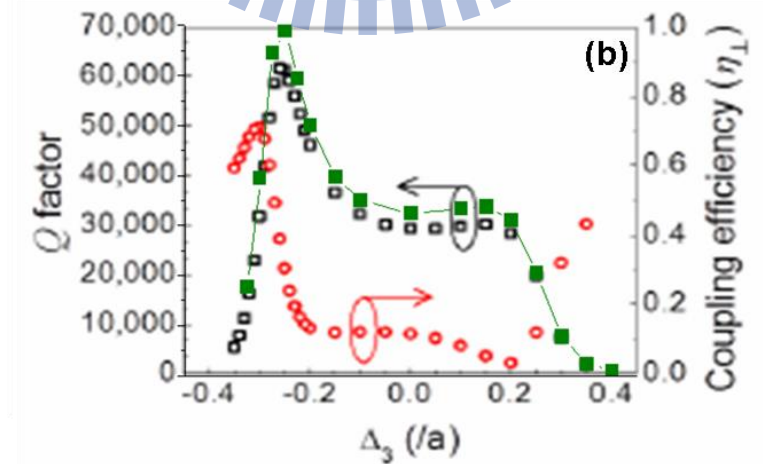


Figure 5.3: Our simulated Q factors compare with that of Ref. 50. The hollow-block points are the results of Ref. 50, and the solid-green points are ours.

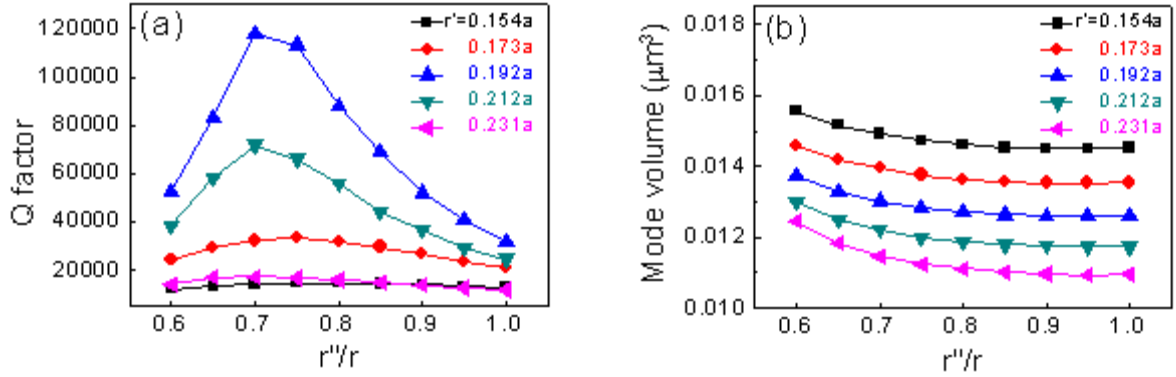


Figure 5.4: (a) Simulated Q factors against varied r''/r ratios. Each line represents individual value of r' from 0.154a to 0.231a. (b) The corresponding mode volumes.

5.3 The spatial Fourier transform of electric field distribution in cavity

To understand how the H1 cavity with modified r''/r ratio reaches a high Q factor, in Fig. 5.5, we plot the simulated electric field (E_x) distribution and the corresponding spatial Fourier transformation in tangential k -vector space ($k_{//}$) for the V-dipole mode in the cavity. The simulated parameters are the same as those used in Fig. 5.4 except that r' is fixed at 0.192a. The Fourier transformation equation is represented as Eq. 5.1.

$$F(k_{//}) = \int_{-\infty}^{\infty} E_x(\vec{r}) e^{-i2\pi k_{//} \vec{r}} d\vec{r} \quad (5.1)$$

Note that the color scales of the Fourier transform profiles are plotted in natural logarithm scale for clarity. In the upper row of Fig. 5.5, the electric field distributions at a plane of $z = 0$ (the center of the membrane) of the cavities with $r''/r = 0.6, 0.7, 0.9,$ and 1.0 have no clear difference between each other. However, in the lower row of Fig. 5.5, the Fourier transformed profiles show interesting features inside the centered light cone indicated by the white circles. Inside the light-cone circle, the tangential

k-component decreases gradually when the r'/r ratios reduces from 1.0 to 0.7 and then increases slightly for that of 0.6. This is consistent with the trend of Q factors in Fig. 5.4(a). The correlation between the Q factors and the Fourier transform components inside a light cone is expected because the Fourier transform components inside the light cone represent the components of leakage modes for which light would escape out of the membrane cavity [20]. More specifically, the light cone is defined as the region for which tangential k-vector component ($|k_{//}|$) is smaller than $2\pi\lambda_0$ (where λ_0 is the wavelength of light in vacuum). When $|k_{//}|$ of light lies outside light cone ($|k_{//}| > 2\pi\lambda_0$), total internal reflection condition is satisfied at the interface between cavity membrane and vacuum, thus light can be confined inside the membrane. Therefore, by reducing the tangential component $|k_{//}|$ inside the light cone ($|k_{//}| < 2\pi\lambda_0$), the Q factor of the cavity can be increased. This explanation has also been stated clearly in [20] for the case of L3 cavity. Fig 5.6 is a 2-D sketch for a medium 1 of refractive index n_1 surrounded with mediums 2 of refractive index n_2 . The light propagate in these mediums by Snell's law Eq. 5.2,

$$n_1 \times \sin \theta_1 = n_2 \times \sin \theta_2 \quad (5.2)$$

while $\theta_2 = 90^\circ$, the critical angle θ_c is express as,

$$\sin \theta_c = \frac{n_2}{n_1} \quad (5.3)$$

If $\theta_1 > \theta_c$, the light cannot propagate into the medium 2, i.e., the total internal reflection condition is satisfied

$$\sin \theta_1 > \sin \theta_c = \frac{n_2}{n_1} \quad (5.4)$$

$$\sin \theta_1 = \frac{k_{//}}{k_{total}} \quad (5.5)$$

k_{total} and $k_{//}$ are total and tangential k-component in medium 1. Inserting Eq. 5.5

into Eq. 5.4

$$\frac{k_{||}}{k_{total}} > \frac{n_2}{n_1} \rightarrow k_{||} > k_{total} \times \frac{n_2}{n_1} = \frac{2\pi}{\lambda_2} \quad (5.6)$$

, where λ_2 is light wavelength in medium 2. Thus the light cone is defined as the region, $k_{||} < 2\pi/\lambda_2$.

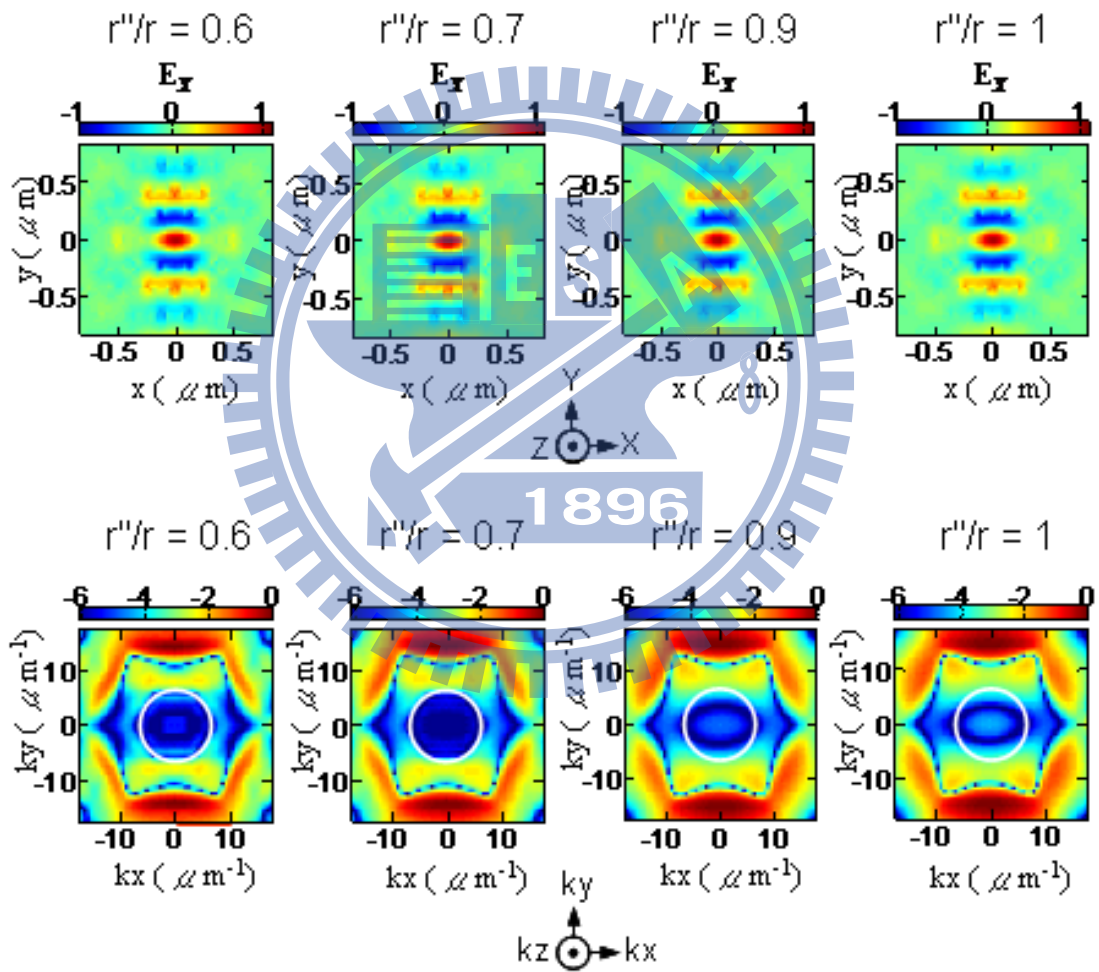


Figure 5.5: The simulated electric field distributions (E_x) of V dipole mode for various r''/r ratios (upper row) and their 2-D spatial Fourier transform profiles in tangential k -vector space $k_{||}$ (lower row). Light cones are plotted in white circles.

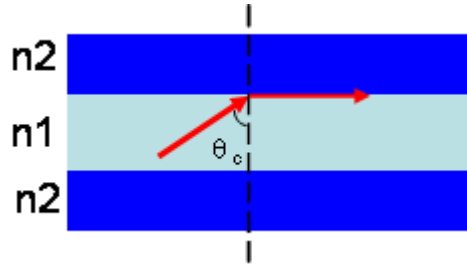


Figure 5.6: The sketch of the total internal reflection condition. Medium 1 of refractive index n_1 is surrounded with mediums 2 of refractive index n_2 .

5.4 Experimental results

The growth and fabrication of the investigated sample (Lm5217) have been introduced in Chapter 3. The photonic crystal membrane is constituted of a GaAs layer with InAs QDs in the middle. Fig. 5.7 shows the top-viewed and cross-section-viewed scanning electron microscopy (SEM) images of one fabricated H1 cavity. Together with the enlarged images on the right, we can see that the sizes of the six nearest holes and those in the region I and II has been reduced. The sample is measured by using the micro-PL system, of which the He-Ne lasers beam was focus onto the center of cavity to excite the cavity signals, and the measured temperature is maintained at 50K. In Fig. 5.8, the measured spectra taken from one of fabricated H1 cavities are shown. Two emission peaks arising from the two fundamental dipole modes (Horizontal and Vertical dipoles) are clearly observed, while we see that there is no on-resonance single QD transition in the emission energies of the two peaks to excite the cavity modes. Many studies have indicated that such off-resonance cavity modes are fed by acoustic phonon-assisted processes [53] or multiexciton transition process [54]. The nondegeneracy of energy between two cavity modes arises from unavoidable imperfection during device processing. The separation is about 0.1–2.0 meV among our studied devices. The measured polar plot of the two modes is taken from the emission intensities as a function of the angle of $\lambda/2$ wave-plate and shown as the inset

in Fig. 5.8. It is obvious that two dipole modes are linearly polarized and orthogonal to each other as expected.

The spectra of more than 40 devices were measured and the intentional size parameters of these devices are $a = 260$ nm, $r = 0.25a$, $s = 0.12a$, and $r' = 0.192a$. To see the effect of r''/r ratio on Q factor and to minimize the influence of fabrication non-uniformity, we arrange the devices in group so the every four devices with four different r'' are within an area of 1 mm^2 . We extract the Q factor of each device from its micro-PL spectrum according to the ratio between the resonant frequency (f) and the full width half maximum (FWHM, Δf), $Q = f/\Delta f$. Here f and Δf are gotten from the Lorentz function-fitting curves of resonant peaks. The measured Q factors are shown in Fig. 5.9(a). Note that the Q factors in Fig. 5.9(a) are the average values of two dipole modes. The Q factors of the devices in the same group are plotted with the same symbol. In Fig. 5.9(a), the devices with r''/r ratio of 1 (reference devices) have the Q factors in the range of 5,000–8,000 due to the fabrication non-uniformity. Comparing with calculated Q factors shown in Fig. 5.4(a), the experimental ones are much lower, which we attribute to the imperfection during the sample growth and/or the device fabrication. Nevertheless, among the measured devices, we still can see a common trend that Q factors gradually increase with decreasing r''/r ratios. When the r''/r ratio comes down to 0.769, the trend becomes unclear. This trend was considerably consistent with the simulated results in Fig. 5.4(a). We also calculate the enhancement factors defined with Q-factor ratio between devices with modified r'' and unmodified ones. In Fig. 5.9(b), it is apparent that the enhancement factors of almost all devices with modified r'' are larger than 1. This tells us that our method is quite effective for Q-factor improvement. That is, even with the fabrication non-uniformity from one device to the other, the Q-factor enhancement still exists. The highest enhancement factor is about 1.55 and the highest Q factor is about 11,700.

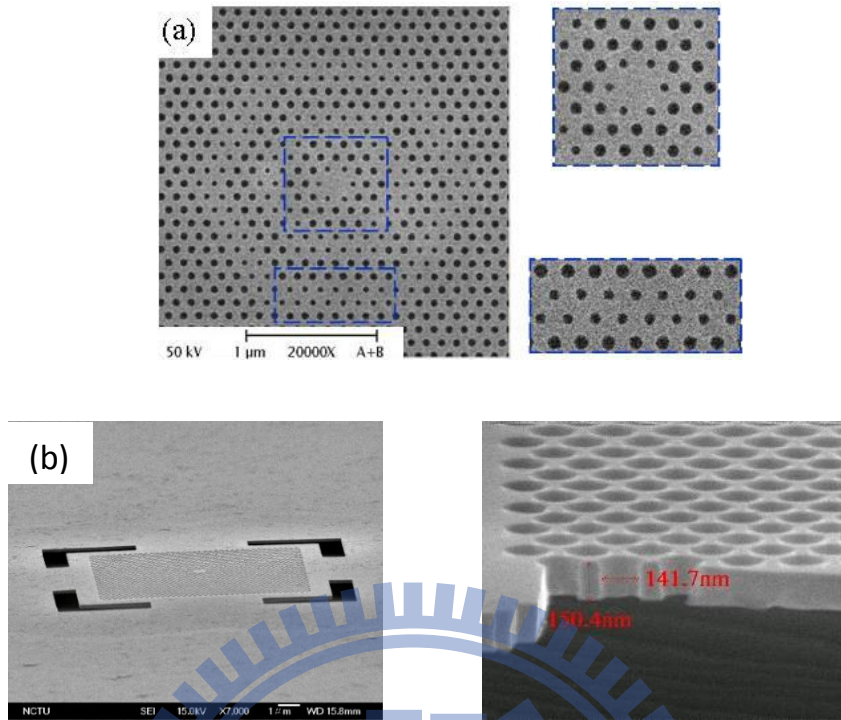


Figure 5.7: (a) Top view of SEM image for fabricated H1 cavity. The right figures are the local enlarged images of the six nearest holes and those in regions I and II. (b) Cross-section view of SEM image.

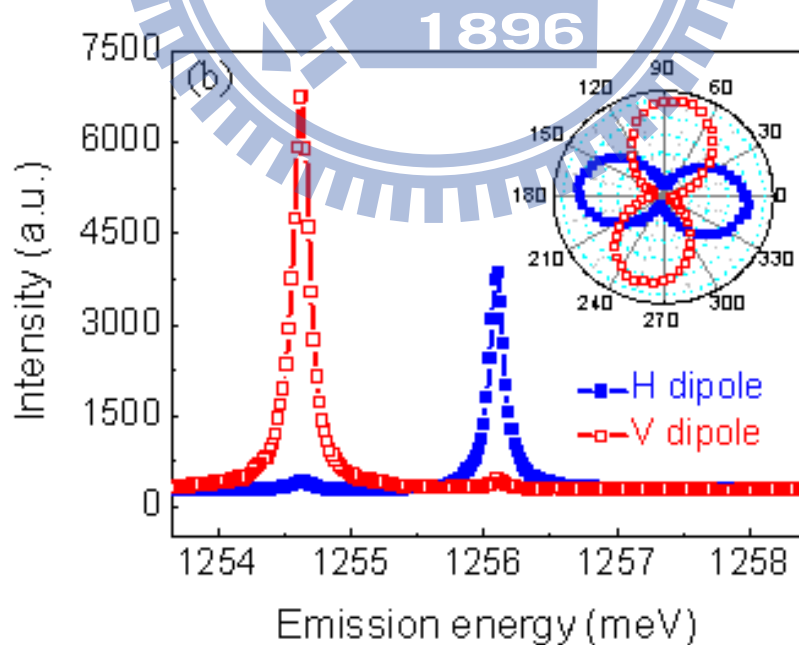


Figure 5.8: Measured spectra showing H- and V-dipole modes of an H1 cavity. The blue and red dots were measured data, and the blue and red curves were fitted data. Inset: the polar plot of cavity modes.

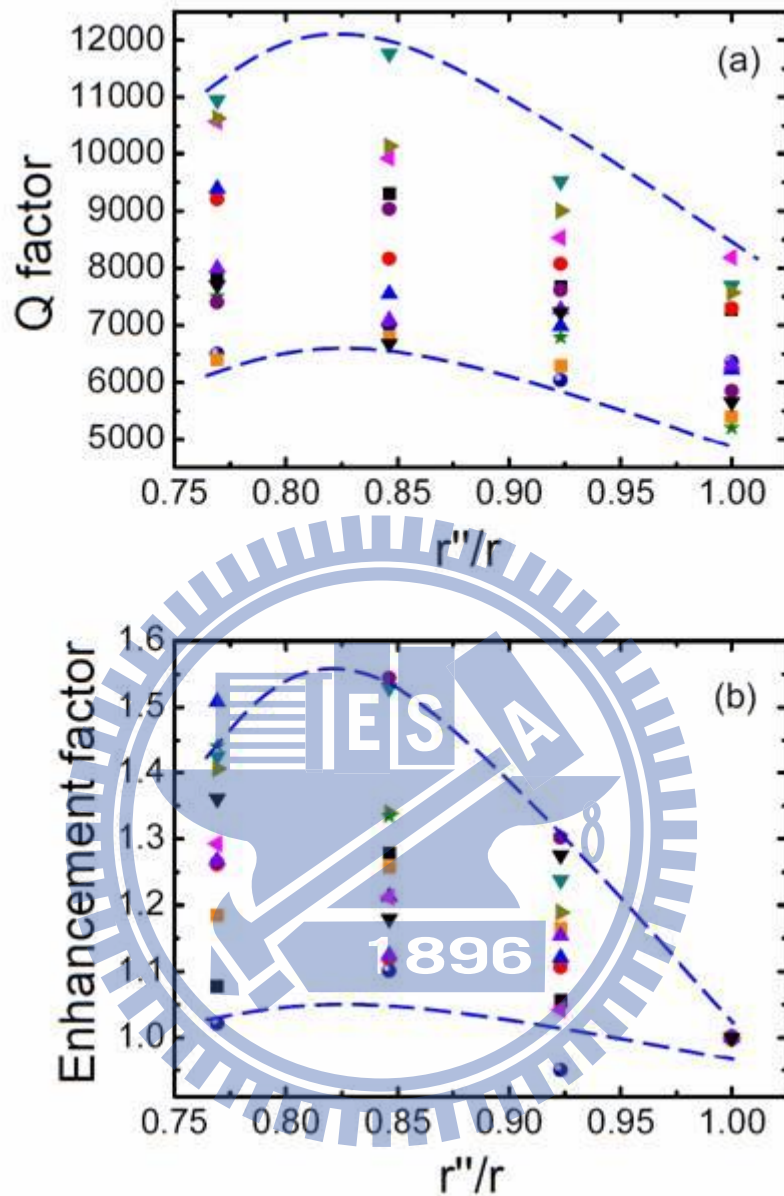


Figure 5.9: Measured Q factors and (b) enhancement factors for r''/r ratios of 1, 0.923, 0.846, and 0.769. The grouping devices are plotted with the same symbol. The dashed lines are guide for the eye.

5.5 The strong coupling effect between InAs QD and cavity

In this part, we report an observation of coupling effect between our designed H1 cavity and single InAs QD. We study this phenomenon via the temperature-dependent micro-PL measurement. The measured results reflect the characteristics of strong coupling.

Temperature-dependent micro-PL measurement

To yield the coupling effect between QD and the cavity, there are two requirements have to be satisfied. One is that only one QD is expected to locate at the high electric field region of the cavity for raising coupling strength, and avoiding too complicated signals from other QDs, thus we must select the area with relatively low QDs density in our sample. Another one is that the emission energy of QD must be consistent with that of the cavity mode. The investigated devices of the H1 cavities are fabricated on the sample Lm5217, which has been introduced in previous content. Fig. 5.10 shows the PL spectra of the area with broad-distributed QD density, we select the region C to fabricate the devices of H1 cavities, which has more suitable QD density. The PL signals in low energy and high energy region (the red and blue shadow) arise from the emissions of QDs and the wetting layer, respectively. The central energy of the wetting layer is about 1415.5 meV, and the emission energies of QDs distribute over a wide range from 1260 meV to 1375 meV. We reasonably design the H1 cavity with these parameters: $a = 260$ nm, $r = 0.25a$ and $d = 130$ nm so that the measured emission energy of cavity mode would be located at the QDs (blue) region.

Sequentially, we measure the micro-PL spectra of these devices and tune the detuning, i.e., the energy difference between cavity mode and single QD signal, by changing the measured temperature. Figure 5.11 shows the spectra taken from one

device at three different temperatures 5.5K, 28K and 35K, one can see that there are three main peaks observed in the region of 1348 nm–1354 nm. With raising temperature, all peaks are red shift, and the shifted rate of the middle peak is obviously faster than that of other peaks on both sides. Thus we can identify the middle peak is the signal of QD due to the obvious energy gap-shrinkage effect induced by raised temperature, and the side peaks are two fundamental dipole modes, respectively. Because the QD signal gradually approaches the dipole mode with lower energy when raising temperature, we would focus on discussing the interaction between QD and this dipole mode. More detailed temperature-dependent micro-PL spectra are taken per 0.25 K or 0.5 K at the measured temperature range from 25 K to 50 K. Fig. 5.12 plots the all spectra at different measured temperature range from 35 K to 41 K. One can clearly see an anti-crossing phenomenon, that is, the QD signal is gradually close to the low energy cavity mode, but they never cross together, finally, far from each other. This is a typical characteristic of strong coupling effect. Using the Lorentz function to fit these peaks in the spectra. The central energies, full width half maximum (FWHM) and intensities of the two fitted peaks are gotten and plotted as a function of temperature in Fig. 5.13. In Fig. 5.13(a), we found that the smallest energy difference between two central energies (ΔE) is about 146 μeV , which occurs at 37.75 K. That means the detuning of QD and cavity mode is zero, and the coupling strength is strongest at this temperature. On the other hand, Fig. 5.13(b) and 5.13(c) show the variations of the fitted FWHM and intensities with temperature, they all exhibit a crossing behavior at about 37.5 K and 37.875 K, which indicates that the QD and cavity mode have mixed into two polariton states at this moment. With far from this temperature, the coupling becomes weaker, resulting in the polariton states gradually transfer into non-coupled QD and cavity mode, which reflects in the removed FWHM and intensity. According to the experimental results, we know that the smallest energy

difference between two central energies (ΔE) is equal to $146 \mu\text{eV}$ when the detuning is zero. The FWHM of the QD signal (γ_{QD}) and the cavity mode (γ_c) can be obtained from the results at the low or high temperature. From Fig. 5.13, γ_{QD} and γ_c are about $110.3 \mu\text{eV}$ and $224.2 \mu\text{eV}$, which indicates that Q factor is equal to 6022. Putting these parameters into Eq. 5.7 or Eq. 2.40

$$\Delta E(\delta) = \sqrt{\Omega_n^2 - \frac{(\gamma_c - \gamma_a)^2}{4}} \quad (5.7)$$

, we can get the Rabi splitting in this system, Ω_n , is equal to $156.7 \mu\text{eV}$.

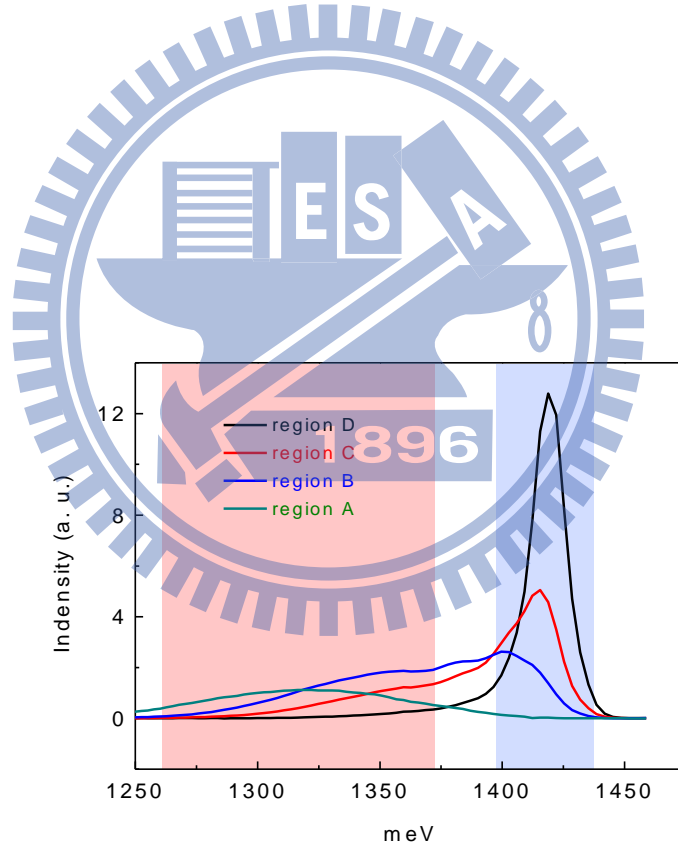


Figure 5.10: The PL-spectra of the area with different QD density in the sample Lm5217.

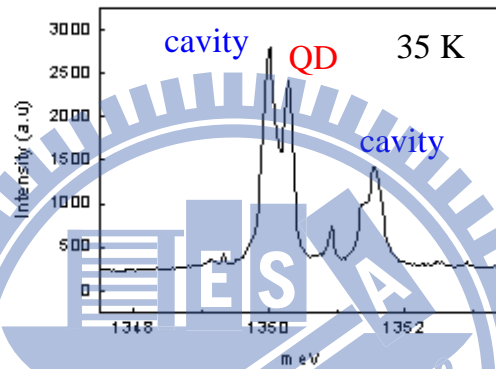
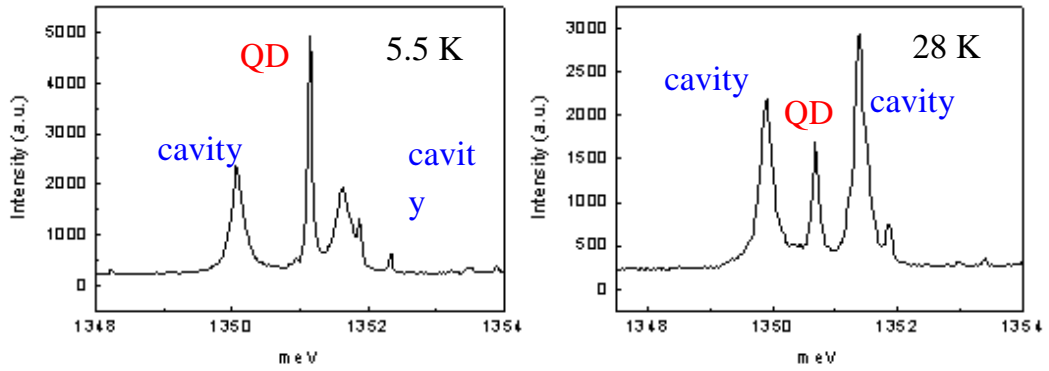


Figure 5.11: The micro-PL spectra at three different temperatures 5.5 K, 28 K and 35K

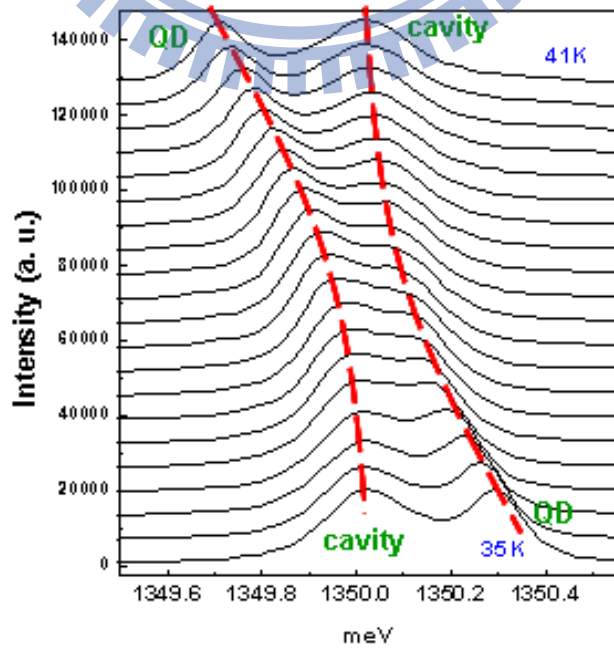


Figure 5.12: The temperature-dependent micro-PL spectra

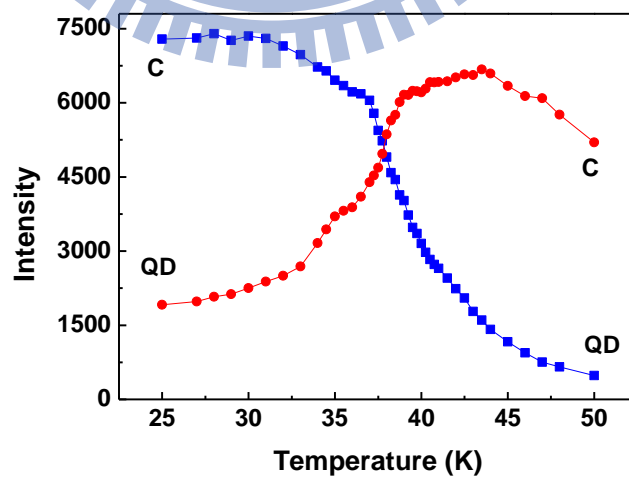
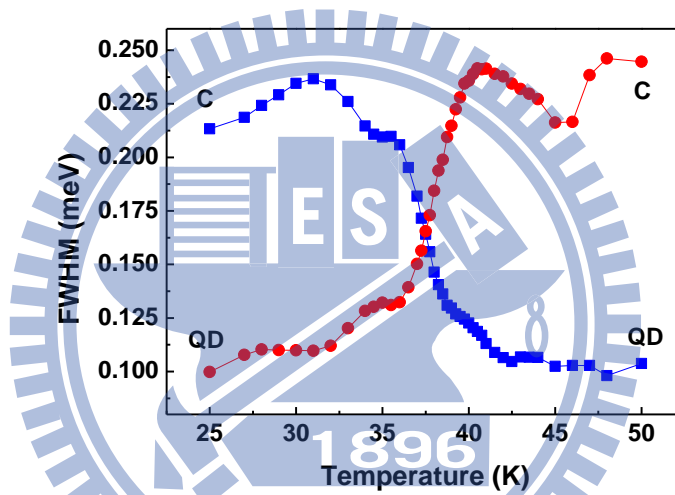
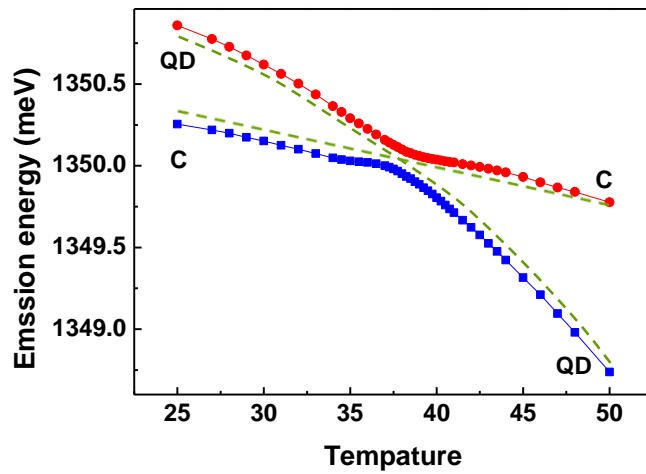


Figure 5.13: The emission energy, FWHM, and intensity as a function of temperature.

Chapter 6 Conclusion and Future work

6.1 Conclusion

In this dissertation, we have study the magneto-optic properties of single InAs/GaAs quantum dot. Besides, we also design a high Q factor H1 cavity in 2-D photonic crystal membrane and have observed the strong interaction between quantum dot and cavity.

First, we have identified four investigated excitonic complexed via the power-dependent and polarization resolution micro-PL measurements. The magnetic responses of excitonic complexes in single self-assembled InAs/GaAs quantum dots have been investigated, including neutral exciton X , biexciton XX , and positive/negative trion X^+ / X^- . For XX and X^+ , their diamagnetic shifts demonstrated the conventional quadratic dependence on magnetic field as neutral exaction. However, the X^- diamagnetic shifts in most of the investigated dots were found to be considerably small and non-quadratic. In particular, we also observed a reversal in sign of the conventional diamagnetic shift. A theoretical analysis indicates that such anomalous behaviors for X^- arise from an apparent change in the electron wave function extent after photon emission due to the strong Coulomb attraction induced by the hole in its initial state. This effect has strong correlation with the sizes of quantum dot and can be very pronounced in small ones, where the electron wave function becomes weakly confined and extended much into the barrier region. When the electrons gradually lose confinement, the magnetic response of X^- will transit gradually from the usual quadratic diamagnetic shift to a quartic dependence, and finally into a special paramagnetic regime with an overall negative energy shift. On the

other hand, because the forming-dots time for low density QDs is shorter than that of high density dots in the growth process, the low density QD's sizes are relatively small. This explains why the investigated dots in our low density QDs sample are relatively small, resulting in the anomalous X^- diamagnetic shifts.

Second, we have presented a design for enhancing the Q factor of H1 PhC cavity. The recorded Q factor of 120,000 in theory has been achieved with a slight increase of mode volume. The 2-D spatial Fourier transform profile in k-space indicates that the components of leakage modes obviously decrease for the designed cavities, where total internal condition is satisfied so that light cannot escape out of the membrane cavity. In experiment, the Q factors also have been improved from 5,000–8,000 to about 11,700. With our design, one has a chance to embed QDs in the cavity for generating entangled photon pair by the strong coupling effect.

Finally, we have successfully demonstrated the strong coupling effect in the H1 cavity embedded one InAs/GaAs quantum dot. By changing measured temperature, we can tune the detuning between QD signal and cavity mode. The strongest coupling occurs at 37.5 - 37.875 K, while the Rabi splitting in this system, Ω_n , is equal to $156.7 \mu eV$.

6.2 Future work

In fact, when observing the strong coupling effect cautiously, one can see that the intensities of two peaks are the same at about 37.875 K, the emission energies are closest at 37.75 K, and the FWHM are cross at 37.5 K as shown in Fig. 6.1. This result seems to be strange because the three points occur at different temperature, so that one cannot know that the strongest coupling occurs at which temperature. We suspect that this temperature-variation may be attributed to the difference in polarized directions of QD and cavity mode. In this system, there are two orthogonal-linear polarized QD

emissions and a linear polarized cavity mode. If the polarized direction of cavity mode is not completely parallel or perpendicular to that of QD emission, the two QD emission would both interact with the cavity mode, that maybe lead to the temperature-difference shown in Fig. 6.1. However, to verify whether this supposition is correct, a micro-PL measurement of all polarized directions is necessary to be analyzed further.

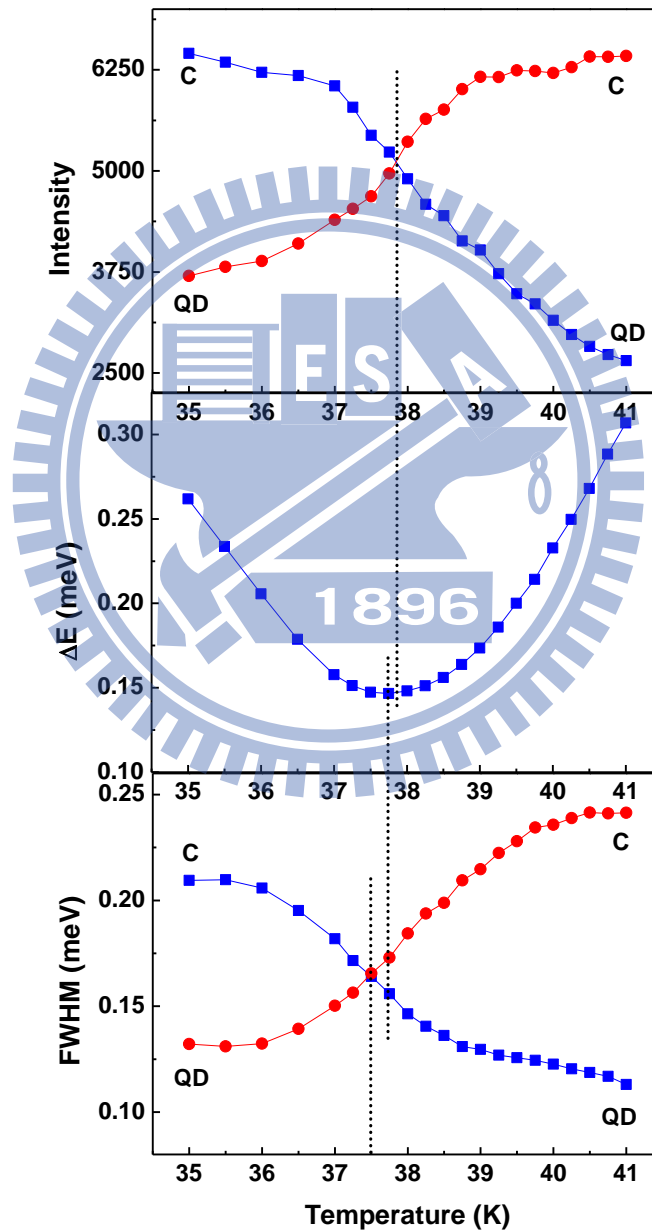


Figure 6.1: The difference in emission energy, FWHM, and intensity of two signals as a function of temperature.

Appendix

A Fock-Darwin model

Consider a particle of effective mass m^* and charge e is placed within a parabolic-confined potential $V_0 = \frac{m^*\omega_0^2}{2}(x^2 + y^2)$ and a uniform magnetic field $\vec{B} = (0, 0, B_z) = \nabla \times \vec{A}$ along z direction, where ω_0 is the angular frequency, and \vec{A} is the vector potential represented as $\vec{A} = \left(-\frac{1}{2}yB_z, \frac{1}{2}xB_z, 0\right)$ by using the symmetric gauge. According to quantum mechanism, the total Hamiltonian can be written as,

$$H = \frac{1}{2m^*} (-i\hbar\nabla + e\vec{A})^2 + V_0 \quad (A.1)$$

Bringing $V_0 = \frac{m^*\omega_0^2}{2}(x^2 + y^2)$ and $\vec{A} = \left(-\frac{1}{2}yB_z, \frac{1}{2}xB_z, 0\right)$ into Eq. A.1. The Hamiltonian is rewritten as,

$$H = \frac{1}{2m^*} \left[-\hbar^2\nabla^2 + i\hbar eB_z \left(y \frac{\partial}{\partial x} - x \frac{\partial}{\partial y} \right) + \frac{e^2 B_z^2}{4} (x^2 + y^2) \right] + \frac{m^*\omega_0^2}{2} (x^2 + y^2) \quad (A.2)$$

In cylindrical coordinates, Eq. A.2 is transformed into

$$H = -\frac{\hbar^2}{2m^*} \left(\frac{\partial^2}{\partial \rho^2} + \frac{1}{\rho} \frac{\partial}{\partial \rho} + \frac{1}{\rho^2} \frac{\partial^2}{\partial \phi^2} \right) - i\hbar \frac{\omega_c}{2} \frac{\partial}{\partial \phi} + \frac{m^*}{2} \left(\frac{\omega_c^2}{4} + \omega_0^2 \right) \rho^2 \quad (A.3)$$

, where $\omega_c = eB_z/m^*$ is the cyclotron angular frequency. If $B_z = 0$, the eigenstates of the Hamiltonian are well known Fock-Darwin states. According to Eq. A.3, one can see that the Schrodinger equation $H\psi(\rho, \phi) = E\psi(\rho, \phi)$ is a separable partial differential equation, thus the eigenfunction $\psi(\rho, \phi)$ can be separated into radial part and angular part,

$$\psi(\rho, \phi) = v(\rho)e^{-i\ell\phi} \quad (A.4)$$

l is the quantum number of angular momentum, $l = 0, \pm 1, \pm 2, \dots$. Bring Eq. A.4 into the Schrodinger equation, we get a radial ordinary differential equation as follows,

$$\left[\frac{\partial^2 v(\rho)}{\partial \rho^2} + \frac{1}{\rho} \frac{\partial v(\rho)}{\partial \rho} - \frac{l^2}{\rho^2} v(\rho) \right] + \left[\frac{lm^* \omega_c}{\hbar} + k^2 - \lambda^2 \rho^2 \right] v(\rho) = 0 \quad (A.5)$$

where $k^2 = \frac{2m^*E}{\hbar^2}$ and $\lambda^2 = \frac{m^*}{\hbar^2} \left(\frac{\omega_c^2}{4} + \omega_0^2 \right)$. To correspond with the boundary condition, $v(\rho)$ approaches zero as ρ close to ∞ , and $v(\rho)$ maintains a finite value as ρ close to zero, we suppose $v(\rho)$ can be written as this form,

$$v(\rho) = \rho^{|l|} e^{-\lambda \rho^2/2} F(\rho) \quad (A.6)$$

Bringing Eq. A.6 into Eq. A.5, we obtained Eq. A.7,

$$\frac{d^2 F(\rho)}{d\rho^2} + \left[\frac{2|l| + 1}{\rho} - 2\lambda\rho \right] \frac{dF(\rho)}{d\rho} - \left[2\lambda(|l| + 1) - k^2 - \frac{lm^* \omega_c}{\hbar} \right] F(\rho) = 0 \quad (A.7)$$

Using the variable χ instead of $\lambda\rho^2$, Eq. A.7 become into a Kummer equation as Eq. A.8, whose solution at $\chi = 0$ is the Confluent Hypergeometric Series

$$\chi \frac{d^2 F(\chi)}{d\chi^2} + [(|l| + 1) - \chi] \frac{dF(\chi)}{d\chi} - \frac{1}{2} \left[(|l| + 1) - \frac{k^2}{2\lambda} - \frac{lm^* \omega_c}{2\hbar\lambda} \right] F(\chi) = 0 \quad (A.8)$$

The solution is

$$F(\chi) = M(a, |l| + 1; \chi) = \sum_{j=0}^{\infty} \frac{a^{(j)} \chi^j}{(|l| + 1)^j j!} \quad (A.9)$$

where

$$a = \frac{1}{2} (|l| + 1) - \frac{k^2}{4\lambda} - \frac{lm^* \omega_c}{4\hbar\lambda} \quad (A.10)$$

For large values of χ , the eigenfunction of $F(\chi)$ would diverge as e^x . In order to

satisfy this, the eigenfunction exists only if

$$a = -n \quad (\text{A. 11})$$

, where $n = 0, 1, 2, \dots$ is a non-negative integer, Thus we can get the eigenfunction and eigenvalue

$$\psi_{nl}(\rho, \phi) = C_{nl} \rho^{|l|} e^{-\lambda \rho^2/2} M(-n, |l| + 1; \lambda \rho^2) e^{-il\phi} \quad (\text{A. 12})$$

$$E_{nl} = (2n + |l| + 1) \hbar \left(\omega_0^2 + \frac{1}{4} \omega_c^2 \right)^{1/2} - \frac{1}{2} l \hbar \omega_c \quad (\text{A. 13})$$

with the normalized constant C_{nl}

$$C_{nl} = \lambda^{(|l|+1)/2} \sqrt{\frac{n!}{\pi(n+|l|)!}} \quad (\text{A. 14})$$

the mean square radius $\langle \rho_B^2 \rangle_{nl}$ is defined as,

$$\langle \rho_B^2 \rangle_{nl} = \langle \psi_{nl} | \rho^2 | \psi_{nl} \rangle = \frac{1}{\lambda} (2n + |l| + 1) \quad (\text{A. 15})$$

We expand Eq. A.13 by Taylor series

$$E_{nl} = (2n + |l| + 1) \hbar \omega_0 \left(1 + \frac{1}{8} \frac{\omega_c^2}{\omega_0^2} - \frac{1}{128} \frac{\omega_c^4}{\omega_0^4} + \dots \right) - \frac{1}{2} l \hbar \omega_c \quad (\text{A. 16})$$

Further, Eq. A.16 can be expanded as

$$E_{nl}(B_z) = (2n + |l| + 1) \hbar \omega_0 + \left(\frac{e^2 \sqrt{\langle \rho_0^2 \rangle_{nl}}^2}{8m^*} B_z^2 - \frac{e^4 \sqrt{\langle \rho_0^2 \rangle_{nl}}^6}{128m^* \hbar^2} B_z^4 + \dots \right) - \frac{e \hbar l}{2m^*} B_z \quad (\text{A. 17})$$

$\sqrt{\langle \rho_0^2 \rangle_{nl}} = \sqrt{\frac{\hbar(2n+|l|+1)}{m^* \omega_0}}$ is the root mean square radius of particle in the state nl at zero magnetic field.

B Hartree approximation

To consider the influence of Coulomb interaction on the magnetic responses of excitonic complexes, the Hartree approximation is a suitable method for solving such many-body problem. Beyond this approximation, the wave functions and energy of all particles in this system are approximated to stable status when considering Coulomb interaction. The Hamiltonian of total N particles system can be written as follows,

$$H = \sum_i^N h_{sp}(\vec{r}_i) + \frac{1}{2} \sum_i^N \sum_{j \neq i}^N V_c(\vec{r} - \vec{r}') \quad (B.1)$$

where h_{sp} is the Hamiltonian of the i th particle without Coulomb interactions and V_c is the Coulomb interaction term. We take the Slater function Ψ^{HF} to retain the fermionic nature of electron and hole.

$$\Psi^{HF} = \frac{1}{\sqrt{N!}} \begin{vmatrix} \phi_1(\vec{r}_1) & \phi_1(\vec{r}_2) & \cdots & \phi_1(\vec{r}_N) \\ \phi_2(\vec{r}_1) & \phi_2(\vec{r}_2) & \cdots & \phi_2(\vec{r}_N) \\ \vdots & \vdots & \ddots & \vdots \\ \phi_N(\vec{r}_1) & \phi_N(\vec{r}_2) & \cdots & \phi_N(\vec{r}_N) \end{vmatrix} \quad (B.2)$$

$\phi_i(\vec{r}_n)$ is the wavefunction of the i th state while the n th particle fills into the i th state. The fermionic nature satisfies the anti-symmetrized condition of the Hartree wave function as follows,

$$\Psi^{HF}(\dots \vec{r}_n \dots \vec{r}_m \dots) = -\Psi^{HF}(\dots \vec{r}_m \dots \vec{r}_n \dots) \quad (B.3)$$

Thus, the total energy of the N particle system is given by

$$\begin{aligned} E^{HF} &= \langle \Psi^{HF} | H | \Psi^{HF} \rangle \\ &= \sum_i^N \langle \phi_i | h_{sp} | \phi_i \rangle + \frac{1}{2} \sum_i^N \sum_{j \neq i}^N \langle \phi_i(\vec{r}) \phi_j(\vec{r}') | V_c(\vec{r} - \vec{r}') | \phi_j(\vec{r}') \phi_i(\vec{r}) \rangle \end{aligned}$$

$$-\frac{1}{2} \sum_i^N \sum_{j \neq i}^N \langle \phi_i(\vec{r}) \phi_j(\vec{r}') | V_c(\vec{r} - \vec{r}') | \phi_i(\vec{r}') \phi_j(\vec{r}) \rangle \quad (B.4)$$

The second and third terms in Eq. B.4 are defined as direct and exchange interaction.

Taking the variation method, we can get Eq. B.5

$$\delta[E^{HF} - \varepsilon_i(\langle \phi_i | \phi_i \rangle - 1)] = 0$$

$$\langle \delta \phi_i | \left\{ \left[h_{sp}(\vec{r}) + \sum_{j \neq i}^N \langle \phi_j | V_c(\vec{r} - \vec{r}') | \phi_j \rangle \right] \phi_i - \sum_{j \neq i}^N \langle \phi_j | V_c(\vec{r} - \vec{r}') | \phi_i \phi_j \rangle \right\} = \varepsilon_i \langle \delta \phi_i | \phi_i \rangle \quad (B.5)$$

, where ε_i is the eigen-energy of the i th state. In order to simplify the problem, we ignore the exchange term and then get the Schrodinger equation of one particle from Eq. B.5,

$$[h_{sp}(\vec{r}) + V_H(\vec{r})] \phi_i(\vec{r}) = \varepsilon_i \phi_i(\vec{r}) \quad (B.6)$$

$$V_H(\vec{r}) = \sum_{j \neq i}^N \langle \phi_j | V_c(\vec{r} - \vec{r}') | \phi_j \rangle = \int d^3 \vec{r}' \frac{e^2 \sum_{j \neq i}^N |\phi_j(\vec{r}')|^2}{4\pi \epsilon_0 \epsilon_b |\vec{r} - \vec{r}'|} = \int d^3 r \frac{e^2 \rho(\vec{r}')}{4\pi \epsilon_0 \epsilon_b |\vec{r} - \vec{r}'|} \quad (B.7)$$

where $V_H(\vec{r})$ is called the Hartree potential arising from the direct Coulomb interactions among particles, which represents the electrostatic potential induced by other N-1 particles. $\rho(\vec{r}')$ is the volume particle density equal to $\sum_{j \neq i}^N |\phi_j(\vec{r}')|^2$. It is clear that the wave function of i th particle $\phi_i(\vec{r})$ is determined by the Hartree potential associated with other particles and the confined potential. Such problem is suitable to be solved by using the self-consistent method, i.e., an iteratively calculated process until convergence.

Reference

- [1] P. Michler, A. Kiraz, C. Becher, W. V. Schoenfeld, P. M. Petroff, Lidong Zhang, E. Hu, A. Imamoglu, "A Quantum Dot Single-Photon Turnstile Device," *Science*, vol. 290, pp. 2282-2285, 2000.
- [2] M. Pelton, C. Santori, J. Vuckovic, B. Zhang, G. S. Solomon, J. Plant, and Y. Yamamoto, "Efficient Source of Single Photons: A Single Quantum Dot in a Micropost Microcavity," *Physical Review Letter*, vol. 89, p. 233602, 2002.
- [3] Z. Yuan, B. E. Kardynal, R. M. Stevenson, A. J. Shields, C. J. Lobo, K. Cooper, N. S. Beattie, D. A. Ritchie, M. Pepper, "Electrically Driven Single-Photon Source," *Science*, vol. 295, pp. 102-105, 2002.
- [4] W.-H. Chang, W. -Y. Chen, H. -S. Chang, T. -P. Hsieh, J. -I. Chyi, and T. -M. Hsu, "Efficient Single-Photon Sources Based on Low-Density Quantum Dots in Photonic-Crystal Nanocavities," *Physical Review Letter*, vol. 96, p. 117401, 2006.
- [5] O. Painter, R. K. Lee, A. Scherer, A. Yariv, J. D. O'Brien, P. D. Dapkus, and I. Kim, "Two-Dimensional Photonic Band-Gap Defect Mode Laser," *Science*, vol. 284, p. 1819, 1999.
- [6] M. Loncar, T. Yoshie, A. Scherer, P. Gogna and Y. Qiu, "Low-threshold photonic crystal laser," *Applied Physics Letters*, vol. 81, pp. 2680-2682, 2002.
- [7] S. Noda, A. Chutinan and M. Imada, "Trapping and emission of photons by a single defect in a photonic bandgap structure," *Nature*, vol. 407, pp. 608-610, 2000.
- [8] Y. Akahane, M. Mochizuki, T. Asano, Y. Tanaka and S. Noda, "Design of a channel drop filter by using a donor-type cavity with high-quality factor in a

- two-dimensional photonic crystal slab," *Applied Physics Letters*, vol. 82, 1341-1343, 2003.
- [9] E. M. Purcell, H. C. Torrey and R. V. Pound, "Resonance Absorption by Nuclear Magnetic Moments in a Solid," *Physical Review*, vol. 69, p. 37, 1946.
- [10] J. C-. Ferrer, L. J. Martínez, I. Prieto, B. Alén, G. M-. Matutano, D. Fuster, Y. González, M. L. Dotor, L. González, P. A. Postigo and J. P. M-. Pastor, "Purcell effect in photonic crystal microcavities embedding InAs/InP quantum wires," *Optics Express*, vol. 20, pp. 7901-7914, 2012.
- [11] S. Noda, M. Fujita and T. Asano, "Spontaneous-emission control by photonic crystals and nanocavities," *Nature Photonics*, vol. 1, pp. 449-458, 2007.
- [12] D. Englund, D. Fattal, E. Waks, G. Solomon, B. Zhang, T. Nakaoka, Y. Arakawa, Y. Yamamoto and J. Vuckovic, "Controlling the Spontaneous Emission Rate of Single Quantum Dots in a Two-Dimensional Photonic Crystal," *Physical Review Letter*, vol. 95, p. 013904, 2005.
- [13] T. D. Happ, I. I. Tartakovskii, V. D. Kulakovskii, J.-P. Reithmaier, M. Kamp and A. Forchel, "Enhanced light emission of $\text{In}_x\text{Ga}_{1-x}\text{As}$ quantum dots in a two-dimensional photonic-crystal defect microcavity," *Physical Review B*, vol. 66, p. 041303, 2002.
- [14] A. Dousse1, J. Suffczynski, A. Beveratos, O. Krebs, A. Lemaitre, I. Sagnes, J. Bloch, P. Voisin and P. Senellart, "Ultrabright source of entangled photon pairs," *Nature*, vol. 466, pp. 217-220, 2010.
- [15] E. Moreau, I. Robert, J. M. Gerard, I. Abram, L. Manin and V. T-. Mieg, "Single-mode solid-state single photon source based on isolated quantum dots in pillar microcavities," *Applied Physics Letters*, vol. 79, pp. 2865-2867, 2001.
- [16] T. Yoshie, A. Scherer, J. Hendrickson, G. Khitrova, H. M. Gibbs, G. Rupper, C. Ell, O. B. Shchekin and D. G. Deppe, "Vacuum Rabi splitting with a single

- quantum dot in a photonic crystal nanocavity," *Nature*, vol. 432, pp. 200-203, 2004.
- [17] Y. Ota, M. Shirane, M. Nomura, N. Kumagai, S. Ishida, S. Iwamoto, S. Yorozu and Y. Arakawa, "Vacuum Rabi splitting with a single quantum dot embedded in a H1 photonic crystal nanocavity," *Applied Physics Letters*, vol. 94, p. 033102, 2009.
- [18] R. Johne, N. A Gippius, G. Pavlovic, D. D. Solnyshkov, I. A. Shelykh and G. Malpuech, "Entangled Photon Pairs Produced by a Quantum Dot Strongly Coupled to a Microcavity," *Physical Review Letter*, vol. 100, p. 240404, 2008.
- [19] P. K. Pathak and S. Hughes, "Generation of entangled photon pairs from a single quantum dot embedded in a planar photonic-crystal cavity," *Physical Review B*, vol. 79, p. 205416, 2009.
- [20] Y. Akahane, T. Asano, B. S. Song and S. Noda, "High-Q photonic nanocavity in a two-dimensional photonic crystal," *Nature*, vol. 425, pp. 944-947, 2003.
- [21] B. S. Song, S. Noda, T. Asano and Y. Akahane, "Ultra-high-Q photonic double-heterostructure nanocavity," *Nature Materials*, vol. 4, pp. 207-210, 2005.
- [22] S. N. Walck and T. L. Reinecke, "Exciton diamagnetic shift in semiconductor nanostructures," *Physical Review B*, vol. 57, p. 9088, 1998.
- [23] M. F. Tsai, H. Lin, C. H. Lin, S. D. Lin, S. Y. Wang, M. C. Lo, S. J. Cheng, M. C. Lee and W. H. Chang, "Diamagnetic Response of Exciton Complexes in Semiconductor Quantum Dots," *Physical Review Letter*, vol. 101, p. 267402, 2008.
- [24] C. Schulhauser, D. Haft, R. J. Warburton, K. Karrai, A. O. Govorov, A. V. Kalameitsev, A. Chaplik, W. Schoenfeld, J. M. Garcia and P. M. Petroff, "Magneto-optical properties of charged excitons in quantum dots," *Physical*

- Review B*, vol. 66, p. 193303, 2002.
- [25] N. I. Cade, H. Gotoh, H. Nakano and H. Okamoto, "Fine structure and magneto-optics of exciton, trion, and charged biexciton states in single InAs quantum dots emitting at 1.3 μ m," *Physical Review B*, vol. 73, p. 115322, 2006.
- [26] H. Sanada, T. Sogawa, H. Gotoh, Y. Tokura, H. Yamaguchi, H. Nakano and H. Kamada, "Magneto-optical spectroscopy of excitons and trions in charge-tunable quantum dots," *Physical Review B*, vol. 79, p. 121303(R), 2009.
- [27] A. Schliwa, M. Winkelkemper and D. Bimberg, "Impact of size, shape, and composition on piezoelectric effects and electronic properties of In(Ga)As/GaAs quantum dots," *Physical Review B*, vol. 76, p. 205324, 2007.
- [28] H. Y. Ramirez, C. H. Lin, C. C. Chao, Y. Hsu, W. T. You, S. Y. Huang, Y. T. Chen, H. C. Tseng, W. H. Chang, S. D. Lin and S. J. Cheng, "Optical fine structures of highly quantized InGaAs/GaAs self-assembled quantum dots," *Physical Review B*, vol. 81, p. 245324, 2010.
- [29] R. M. Stevenson, R. J. Young, P. See, D. G. Gevaux, K. Cooper, P. Atkinson I. Farrer, D. A. Ritchie and A. J. Shields, "Magnetic-field-induced reduction of the exciton polarization splitting in InAs quantum dots," *Physical Review B*, vol. 73, p. 033306, 2006.
- [30] B. D. Gerardot, S. Seidl, P. A. Dalgarno, R. J. Warburton, D. Granados, J. M. Garcia, K. Kowalik, O. Krebs, K. Karrai, A. Badolato and P. M. Petroff, "Manipulating exciton fine structure in quantum dots with a lateral electric field," *Applied Physical Letters*, vol. 90, p. 041101, 2007.
- [31] W. Langbein, P. Borri, U. Woggon, V. Stavarache, D. Reuter and A. D. Wieck, "Control of fine-structure splitting and biexciton binding in In_xGa_{1-x}As

- quantum dots by annealing," *Physical Review B*, vol. 69, p. 161301, 2004.
- [32] A. I. Tartakovskii, M. N. Makhonin, I. R. Sellers, J. Cahill, A. D. Andreev, D. M. Whittaker, J-P. R. Wells, A. M. Fox, D. J. Mowbray, M. S. Skolnick, K. M. Groom, M. J. Steer, H. Y. Liu and M. Hopkinson, "Effect of thermal annealing and strain engineering on the fine structure of quantum dot excitons," *Physical Review B*, vol. 70, p. 193303, 2004.
- [33] S.-J. Cheng, W. Sheng and P. Hawrylak, "Theory of excitonic artificial atoms: InGaAs/GaAs quantum dots in strong magnetic fields," *Physical Review B*, vol. 68, p. 235330, 2003.
- [34] R. J. Warburton, B. T. Miller, C. S. Dürr, C. Bödefeld, K. Karrai, J. P. Kotthaus, G. Medeiros-Ribeiro, P. M. Petroff and S. Hant, "Coulomb interactions in small charge-tunable quantum dots: A simple model," *Physical Review B*, vol. 58, p. 16221, 1998.
- [35] M. Bayer, S. N. Walck, T. L. Reinecke and A. Forchel, "Exciton binding energies and diamagnetic shifts in semiconductor quantum wires and quantum dots," *Physical Review B*, vol. 57, p. 6584, 1998.
- [36] Y. Nagamune, Y. Arakawa, S. Tsukamoto, M. Nishioka, S. Sasaki and N. Miura, "Photoluminescence spectra and anisotropic energy shift of GaAs quantum wires in high magnetic fields," *Physical Review Letter*, vol. 69, p. 2963, 1992.
- [37] T. Someya, H. Akiyama and H. Sakaki, "Laterally Squeezed Excitonic Wave Function in Quantum Wires," *Physical Review Letter*, vol. 74, p. 3664, 1995.
- [38] E. Yablonoyitch, "Inhibited Spontaneous Emission in Solid-State Physics and Electronics," *Physical Review Letter*, vol. 58, p. 2059, 1987.
- [39] S. John, "Strong localization of photons in certain disordered dielectric superlattices," *Physical Review Letter*, vol. 58, p. 2486, 1987.

- [40] C. Y. Su, "Study on Integration of Photonic Crystal and Semiconductor Laser," M. S. Thesis, Dept. Elect. Eng., National Chiao Tung Univ., Hsinchu, Taiwan, 2008.
- [41] M. F. Tasi, "Studies of Single InAs Quantum Dots Photoluminescence," M. S. Thesis, Dept. Elect. Eng., National Chiao Tung Univ., Hsinchu, Taiwan, 2007.
- [42] J.-. Maeda, Y. Sasaki, N. Dietz, K. Shibahara, S. Yokoyama, S. Mityazaki and M. Hirose, "High-rate GaAs epitaxial lift-off technique for optoelectronic integrated circuits," *Japanese Journal of Applied Physics*, vol. 36, pp. 1554-1557, 1997.
- [43] Kota S. R. Koteswara Rao, T. Katayama, S. Yokoyama and M. Hirose, "Optimum Atomic Spacing for AlAs Etching in GaAs Epitaxial Lift-Off Technology," *Japanese Journal of Applied Physics*, vol. 39, pp. L 457–L 459, 2000.
- [44] A. A. Kiselev, E. L. Ivchenko and U. Rossler, "Electron g factor in one- and zero-dimensional semiconductor nanostructures," *Physical Review B*, vol. 58, p. 16353, 1998.
- [45] M. W. Taylor, P. Spencer, E. Clarke, E. Harbord and R. Murray, "Tuning exciton g -factors in InAs/GaAs quantum dots," *Journal of Physics D: Applied Physics*, vol. 46, p. 505105, 2013.
- [46] T. Nakaoka, T. Saito, J. Tatebayashi and Y. Arakawa, "Size, shape, and strain dependence of the g factor in self-assembled In(Ga)As quantum dots," *Physical Review B*, vol. 70, p. 235337, 2004.
- [47] T. Nakaoka, T. Saito, J. Tatebayashi, S. Hirose, T. Usuki, N. Yokoyama and Y. Arakawa, "Tuning of g -factor in self-assembled In(Ga)As quantum dots through strain engineering," *Physical Review B*, vol. 71, p. 205301, 2005.

- [48] C. E. Pryor and M. -E. Pistol, "Band-edge diagrams for strained III–V semiconductor quantum wells, wires, and dots," *Physical Review B*, vol. 72, p. 205311, 2005; we use the material parameters in this dissertation except the hole effective mass of $0.5m_0$.
- [49] U. Bockelmann, W. Heller, and G. Abstreiter, "Microphotoluminescence studies of single quantum dots. II. Magnetic-field experiments," *Physical Review B*, vol. 55, p. 4469, 1997.
- [50] H. Takagi, Y. Ota, N. Kumagai, S. Ishida, S. Iwamoto and Y. Arakawa, "High Q H1 photonic crystal nanocavities with efficient vertical emission," *Optics Express*, vol. 20, pp. 28292-28300, 2012.
- [51] M. Shirane, S. Kono, J. Ushida, S. Ohkouchi, N. Ikeda, Y. Sugimoto and A. Tomita, "Mode identification of high-quality-factor single-defect nanocavities in quantum dot-embedded photonic crystals," *Journal of Applied Physics*, vol. 101, p. 073107, 2007.
- [52] H. -Y. Ryu., M. Notomi and Y. -H. Lee, "High-quality-factor and small-mode-volume hexapole modes in photonic-crystal-slab nanocavities," *Applied Physics Letters*, vol. 83, pp. 4294-4296, 2003.
- [53] J. Suffczynski, A. Dousse, K. Gauthron, A. Lemaitre, I. Sagnes, L. Lanco, J. Bloch, P. Voisin and P. Senellart, "Origin of the Optical Emission within the Cavity Mode of Coupled Quantum Dot-Cavity Systems," *Physical Review Letter*, vol. 103, p. 027401, 2009.
- [54] M. Winger, T. Volz, G. Tarel, S. Portolan, A. Badolato, K. J. Hennessy, E. L. Hu, A. Beveratos, J. Finley, V. Savona and A. Imamoglu, "Explanation of Photon Correlations in the Far-Off-Resonance Optical Emission from a Quantum-Dot–Cavity System," *Physical Review Letter*, vol. 103, p. 207403, 2009.

Vita

Name : Ying-Jhe Fu (傅英哲)

Date of birth : December 26, 1983

Place of birth : Tainan, Taiwan, ROC

E-mail : dueto.ee95g@nctu.edu.tw

Sex : Male

Education :

National Chiao Tung University Ph. D. September, 2007 – July, 2014
Department of Electronics Engineering & Institute of Electronics

National Chiao Tung University M. S. September, 2006 – June, 2007
Department of Electronics Engineering & Institute of Electronics

National Chiao Tung University B. S. September, 2002 – June, 2006
Department of Materials Science and Engineering

Title of Ph. D. Dissertation :

Magneto-Optical Properties of Single InAs Quantum Dot and Their Coupling to
Photonic Crystal Cavity

Publication List

- [1] **Y. J. Fu**, S. D. Lin, M. F. Tsai, H. Lin, C. H. Lin, H. Y. Chou, S. J. Cheng and W. H. Chang, "Anomalous diamagnetic shift for negative trions in single semiconductor quantum dots," *Physical Review B*, vol. 81, p. 113307, 2010.
- [2] **Y. J. Fu**, Yi-Shan Lee and Sheng-Di Lin, "Design and demonstration of high quality-factor H1-cavity in 2-D photonic crystal," *Optics Letters*, vol. 38, pp. 4915-4918, 2013.
- [3] S. D. Lin, **Y. J. Fu** and C. Cheng, "Imbalanced initial populations between dark and bright states in semiconductor quantum dots," *Optics Express*, vol. 20, pp. 19850-19858, 2012.
- [4] W. H. Chang, C. H. Lin, **Y. J. Fu**, T. C. Lin, H. Lin, S. J. Cheng, S. D. Lin, C. P. Lee, "Impacts of coulomb interactions on the magnetic responses of excitonic complexes in single semiconductor nanostructures," *Nanoscale Research Letters*, vol. 5, pp. 680-685, 2010.
- [5] Yu. B. Ovchinnikov, J. Hayes, D. J. Richardson, **Y. J. Fu**, S. D. Lin, P. See, A.G. Sinclair, "Wide spectral range confocal microscope based on endlessly single-mode fiber," *Optics Express*, vol. 18, pp. 18811-18819, 2010.
- [6] **Y. J. Fu**, S. D. Lin, M. F. Tsai, H. Lin, C. H. Lin, S. Y. Wang, S. J. Cheng and W. H. Chang, "Diamagnetic shift of exciton complexes in InAs quantum dots" 18th international conference on Electronic Properties of Two-Dimensional Systems (EP2DS18), Kobe, Japan (Jul. 19-24, 2009)